

DEVELOPMENT OF FBAR BASED ULTRA LOW PHASE NOISE RADIO FREQUENCY OSCILLATOR

張, 国強

<https://doi.org/10.15017/1398545>

出版情報：九州大学, 2013, 博士（学術）, 課程博士
バージョン：
権利関係：全文ファイル公表済



Kyushu University
Graduate School of Information
Science and Electrical Engineering

DEVELOPMENT OF FBAR BASED ULTRA LOW PHASE NOISE RADIO FREQUENCY OSCILLATOR

By
Guoqiang Zhang

A THESIS
Submitted in partial fulfillment of
The requirements for the degree of
[DOCTOR OF ENGINEERING]

KYUSHU UNIVERSITY
FUKUOKA, JAPAN
2013

Table of Contents

Table of Contents	2
Table of Figures	4
Acknowledgements	6
Abstract	7
Chapter I Introduction	8
1.1. Background	8
1.2. Motivation	9
1.3. Research Objective	11
1.4. Thesis Organization	11
Chapter II FBAR Resonator and Oscillator Fundamentals	13
2.1. Introduction	13
2.2. Review of FBAR Resonators	13
2.2.1. Structure of FBAR Resonators	13
2.2.2. Equivalent Circuit of FBAR Resonators	14
2.3. Oscillator Fundamentals	19
2.3.1. Barkhausen Criteria and Negative Resistance Theory	19
2.3.2. Frequency Tuning Method of FBAR Oscillator	22
2.3.3. Phase Noise Model of FBAR oscillator	24
2.4. Conclusion	25
Chapter III Pierce and Inverter FBAR-DCO	27
3.1. Introduction	27
3.2. Pierce FBAR-DCO	27
3.2.1 Pierce FBAR-DCO Design and Analyses	27
3.2.2 Simulation Result	32
3.2.3 Chip Fabrication	35
3.3. Inverter based FBAR-DCO	37
3.3.1 Inverter based FBAR-DCO Design and Analyses	37

3.3.2 Simulation Result	39
3.3.3 Chip Fabrication	41
3.4 Conclusion	41
Chapter IV Cross-coupled and Multiband FBAR-VCO	44
4.1. Introduction	44
4.2. 1.9 GHz cross-coupled FBAR-VCO	45
4.2.1 Circuit Design	45
4.2.2. Low Frequency Instability Analyses and Elimination	47
4.2.3. Optimization of Phase Noise and Loop Gain.....	54
4.2.4. Simulation Result	56
4.3. Multiband FBAR-VCO	59
4.3.1. Circuit Design	59
4.3.2. Simulation Result	63
4.4. Conclusion	65
Chapter V FBAR-VCO based PLL	66
5.1. Introduction	66
5.2. Design of FBAR-VCO based PLL	67
5.2.1. Stability Analysis and LPF Design.....	67
5.2.2. Circuit Design	73
5.2.3. Phase Noise Analysis.....	79
5.3. Conclusion	83
Chapter VI Conclusion and Future Work.....	84
6.1. Conclusion	84
6.2. Future work.....	85
Reference	86

Table of Figures

Fig. 1. 1 Block of CMOS transceiver	8
Fig. 2. 1 Structure of FBAR.....	14
Fig. 2. 2 BVD model of FBAR	15
Fig. 2. 3 MBVD model of FBAR.....	16
Fig. 2. 4 Simplified model used only at f_s (a) and at f_p (b)	17
Fig. 2. 5 Magnitude and phase of FBAR impedance	18
Fig. 2. 6 Unity-gain negative feedback system.....	19
Fig. 2. 7 (a) Damped oscillation, (b) add a negative resistance provided by active circuit to cancel the loss of R_p	20
Fig. 2. 8 A NMOS cross-coupled pair based negative resistance generation circuit	21
Fig. 2. 9 FBAR with tunable capacitor in parallel	22
Fig. 2. 10 N bits capacitor bank	23
Fig. 2. 11 Capacitance-voltage characteristic of CMOS varactor.....	23
Fig. 2. 12 Phase noise curve of Lesson model.....	25
Fig. 3. 1 Parameters of the adopted FBAR	27
Fig. 3. 2 Circuit of the proposed Pierce FBAR-DCO	28
Fig. 3. 3 Equivalent circuit of the proposed Pierce FBAR-DCO.....	29
Fig. 3. 4 Simplified equivalent circuit	30
Fig. 3. 5 Admittance of the proposed Pierce FBAR-DCO	31
Fig. 3. 6 Small signal loop gain and phase of proposed Pierce FBAR-DCO	32
Fig. 3. 7 Tuning curve of the proposed FBAR-DCO	33
Fig. 3. 8 Output waveform of the proposed Pierce FBAR-DCO.....	34
Fig. 3. 9 Phase noise comparison between the proposed FBAR-DCO and LC-VCO	34
Fig. 3. 10 Photograph of Pierce FBAR-DCO (a) without FBAR,	36
Fig. 3. 11 Circuit of the proposed inverter based FBAR-DCO	37
Fig. 3. 12 Curve of $ V_{th} - VFBB$	38
Fig. 3. 13 Output waveform of the proposed inverter based FBAR-DCO.....	40
Fig. 3. 14 Phase noise of the proposed inverter based FBAR-DCO	40
Fig. 3. 15 Photograph of inverter based FBAR-DCO	41
Fig. 3. 16 Parallel resonance impedance of FBAR when R_0 is kept at 0.5 ohm.....	42
Fig. 4. 1 Parameters and impedance response of the adopted FBAR	45
Fig. 4. 2 Circuit of the proposed FBAR-VCO	46
Fig. 4. 3 Equivalent circuit of the proposed FBAR-VCO	47

Fig. 4. 4 Redrawn equivalent circuit of the proposed FBAR-VCO	48
Fig. 4. 5 Small signal equivalent circuit of the circuit in Fig. 4.4.....	49
Fig. 4. 6 Parasitic oscillation of a cross-coupled FBAR-VCO	50
Fig. 4. 7 Two methods for enhancing Z_s in low frequency.....	51
Fig. 4. 8 Impedance comparison of C_a and series- L_aC_b	52
Fig. 4. 9 Loop gain comparison by using the two methods for enhancing Z_s	52
Fig. 4. 10 Low frequency gain margin with the size changing of the NMOS transistors M_3 and M_4 (W_n).....	53
Fig. 4. 11 Relationship among the size of PMOS transistor M_1 and M_2 (W_p), Q-factor, phase noise (a) and loop gain (b)	56
Fig. 4. 12 Layout of the proposed cross-coupled FBAR-VCO	57
Fig. 4. 13 Output waveform of the proposed FBAR-VCO	58
Fig. 4. 14 Phase noise comparison of FBAR-VCO by using the two methods for enhancing Z_s	58
Fig. 4. 15 Proposed multiband FBAR-VCO.....	60
Fig. 4. 16 Schematic of divide-by-2 or 3 divider	61
Fig. 4. 17 Schematic of multiply-by-2 multiplier	62
Fig. 4. 18 Layout of the proposed multiband FBAR-VCO	63
Fig. 4. 19 Output waveform of the proposed multiband FBAR-VCO	64
Fig. 4. 20 Phase noise of the proposed multiband FBAR-VCO	64
Fig. 5. 1 Structure of FBAR-VCO base PLL.....	66
Fig. 5. 2 Linear phase model of PLL.....	67
Fig. 5. 3 Third-order passive LPF	68
Fig. 5. 4 Bode graph of the proposed PLL	71
Fig. 5. 5 Locking process of PLL.....	72
Fig. 5. 6 Traditional tri-state PFD	73
Fig. 5. 7 Schematic of CP	74
Fig. 5. 8 Current mismatch characteristic of CP (a) and current noise of PFD and CP (b)	75
Fig. 5. 9 Divider based on MMD architecture	76
Fig. 5. 10 Proposed 2/3 divider cell and timing diagram	77
Fig. 5. 11 Output waveform (a) and output noise (b) of MMD based divider	78
Fig. 5. 12 Linear phase model of PLL with noise of each block	79
Fig. 5. 13 Output phase noise of each block (a) and the total phase noise of PLL (b)	82
Fig. 5. 14 Layout of proposed PLL	82

Acknowledgements

I would like to express my deep gratitude and sincere appreciation to my supervisors and advisors, Professor Ramesh Kumar Pokharel, Professor Haruichi Kanaya, Professor Keiji Yoshida, for their kindness, guidance, advice, and valuable suggestions during each stage of completion of my study.

I also would like to express my special thanks to Dr. Ruibing Dong for his guidance on my research and his help on my life when I just went to Japan, to Dr. Kochhar for his hard work on the fabrication of my designed chips and to Dr. Anand for his help on the English check of my paper. Also I need to thanks other lab members to their help, kindness and enjoyable time.

I am grateful to thank my parents and my sister for their encouragement and support when I felt upset.

Finally, I also would like to acknowledge China Scholarship Council (CSC) in providing scholarship for my doctoral study at Kyushu University, Japan.

Abstract

In future generation wireless communication systems, the demand of low cost and high performance integration RF transceivers is rapidly growing. High performance oscillators such as low phase noise frequency reference and voltage controlled oscillators (VCO) are the main issues to satisfy the increasing requirement of RF transceivers.

In this thesis, low phase noise monolithic FBAR oscillators are realized by employing high Q-factor FBAR resonators, which have the potential to replace the quartz crystal oscillators as frequency reference and replace the normal Ring-VCO and LC-VCO as local oscillators of RF transceivers. The contributions of this thesis can be divided into three parts. The first part is that a low phase noise monolithic Pierce FBAR-DCO and an inverter based FBAR-DCO are designed, which demonstrated the possibility of monolithic FBAR oscillator and the over 20 dB improvement of phase noise. The second part is that in the design of cross-coupled FBAR-VCO, the novel methods based on capacitor or series inductor-capacitor are proposed to solve low frequency instability; the novel phase noise optimization method based on considering the effect of transistors' size on the Q-factor of FBAR is proposed, which makes the proposed FBAR-VCO has a phase noise below -150 dBc/Hz at 1 MHz offset frequency; the possibility of a multiband VCO using FBAR-VCO as a core circuit has been demonstrated. The third part is that instead of LC-VCOs in the traditional PLL, we employ the presented cross-coupled FBAR-VCO to design an FBAR-VCO based PLL. A new charge pump design based on complementary logic switches is adopted to reduce the mismatch current and the current noise. The proposed PLL proves the possibility of FBAR-VCO based PLL and the simulation result shows the phase noise of FBAR-VCO is further improved.

Chapter I

Introduction

1.1. Background

Wireless communication applications such as mobile, wireless sensor network and wireless local area network, have an explosive growth in recent years. With the rapid growth, the requirement of low cost, high performance and high integration radio frequency (RF) integrated circuits (RFIC) is also increasingly higher. In the past decades, complementary metal-oxide-semiconductor (CMOS), a low cost technology for constructing integrated circuits (IC), has been employed by RFIC researchers and a number of high integration RFICs such as RF transceivers [1-3] which integrate phase lock loop (PLL) or voltage controlled oscillators (VCO), filter, mixer, power amplifier (PA), low noise amplifier (LNA), variable gain amplifier (VGA), analog to digital converter (ADC), digital to analog converter (DAC), and have both transmission and receiving functions, as shown in Fig. 1.1, have been designed successfully.

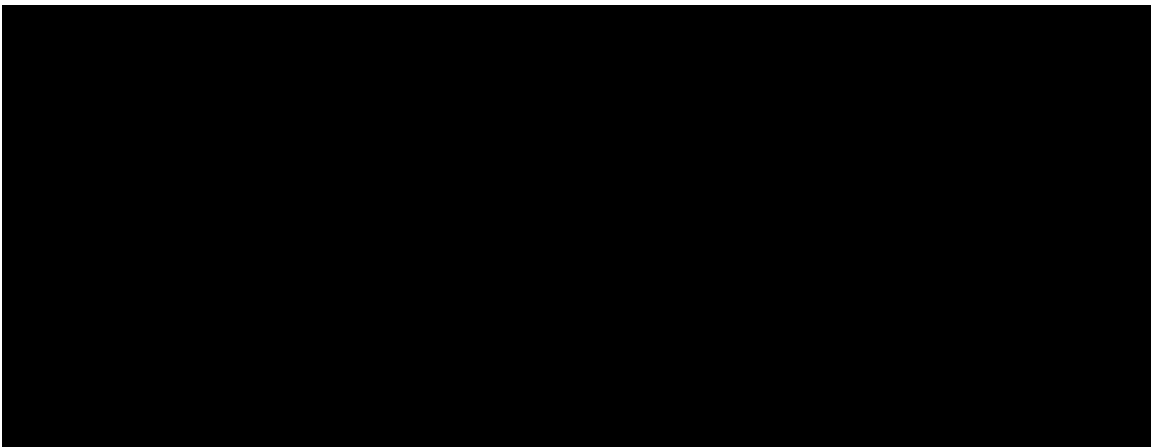


Fig. 1. 1 Block of CMOS transceiver

However, despite the characteristics of low cost, high integration, CMOS technology also reveals thin metals, high loss substrate disadvantages, which brings challenges in the design of high quality (Q) factor inductors and filters, low phase noise VCO, and high efficiency PA.

In recent years, micro electro-mechanical systems (MEMS) technology has become new solutions to compensate the demerits of CMOS. High performances RF-MEMS devices, such as RF-MEMS switches [4-6], variable capacitors [7-9], filters [10-12], and resonators [13-15] have been reported and several approaches for integrating MEMS with CMOS [16-18] have been published, which makes monolithic MEMS-CMOS RFIC possible and become the trend of development of RFIC in the future.

1.2. Motivation

Oscillators which are used to generate local oscillation signals such as voltage controlled oscillator or reference frequency signals such as quartz crystal oscillators are one of the most important building blocks of RF transceivers. To realize a high performance RF transceiver, a high accuracy frequency reference and a VCO which has the features of low phase noise, low power consumption and small area are required. For frequency reference, quartz crystal oscillators are usually adopted as the low phase noise and high accuracy. But the frequency of quartz crystal oscillators is very low and they cannot be integrated because of the incompatibility of the silicon substrate and the large size of quartz crystal. For VCOs' design, two main topologies, which are usually adopted, are ring and inductor-capacitor (LC). Ring VCOs are composed of a series of back-to-back-connected inverters, and LC-VCOs employ CMOS transistors as driving circuits and

oscillate at the resonance frequency of inductor-capacitor based resonator. However, since the low quality (Q-) factor of on-chip inductors, the phase noise of LC-VCOs is always very poor, normally about $-120 \sim -130$ dBc/Hz at 1 MHz offset frequency [19, 20]. For ring VCOs, because no resonator is used, the phase noise is even as poor as $-90 \sim -100$ dBc/Hz at 1 MHz offset frequency [21, 22]. In practice, to overcome the poor phase noise problem, when designing RF transceivers, researchers always employ low phase noise quartz crystal oscillators as frequency reference and make up PLL based frequency synthesizers which can generate GHz frequency signals by multiplying the reference frequency by factor N [23]. By PLLs, although the in-band phase noise can be improved by the low phase noise frequency reference, the out-band phase noise is still poor and spurious caused by reference frequency is not easy to suppress. Thus, it is necessary to find other solutions to create a kind of oscillators which have low phase noise and is able to be integrated with CMOS technology.

Film bulk acoustic resonators (FBAR), a kind of MEMS resonator, have very high estimated Q-factor around 1000 or even more [24-26]. Using them to replace the low Q-factor on-chip inductors to design low phase noise GHz-range oscillators, has been of great interest and some FBAR-oscillators which have low phase noise around -140 dBc/Hz at 1 MHz offset frequency are able to obtain by some published papers [24-26].

Based on the introduces above, it can be shown that FBAR-oscillators have the potential to satisfy the low phase noise and integration requirement, but the challenges to design FBAR-oscillators are multi-frequency, differential output, the further improvement of phase noise, low frequency instability and monolithic integration. The low phase noise potential and those challenges give the motivation for this research.

1.3. Research Objective

The first objective of this research is to design a low phase noise FBAR based digital controlled oscillator (DCO) using for 2.4GHz frequency. The proposed designs employ Pierce oscillator based architecture and inverter based architecture.

The second objective is to design a low phase noise differential output FBAR-VCO operating at 1.9 GHz and a low phase noise multiband FBAR-VCO for 0.65 GHz, 0.98 GHz, 1.96 GHz and 3.92 GHz. The designs use cross-coupled architecture and extend oscillation frequency by divider and multiplier.

The third objective is to design a 1.9 GHz FBAR-VCO based PLL to further improve the in-band phase noise of FBAR-VCO.

1.4. Thesis Organization

This thesis is organized as follows. In Chapter II, in the first, the basic of FBAR resonator is introduced. Then a brief introduction to oscillators is presented, covering basic LC-tanks, negative resistance theory, tuning method model and phase noise.

Chapter III focuses on analysis and design of Pierce FBAR-DCO and inverter architecture based FBAR-DCO. Circuit's analysis based on oscillation condition and post-layout simulation results are discussed.

In Chapter IV, the design of cross-coupled architecture based FBAR-VCO and multiband FBAR-VCO is explained with their specifications such as oscillation frequency and low phase noise. Post-layout simulation results are provided.

In Chapter V, the design of FBAR-VCO based PLL is explored. Each part of PLL including phase frequency detector (PFD), charge pump (CP) and divider has been designed, and the simulation of phase noise has been completed.

Finally, summarizes the contributions of this research, and suggests future research in Chapter VI.

Chapter II

FBAR Resonator and Oscillator Fundamentals

2.1. Introduction

An FBAR-oscillator mainly consists of two parts: FBAR resonator and CMOS active circuit. Thus, in this chapter, firstly the structure and equivalent circuit of FBAR resonator is described briefly. Then the oscillator fundamentals including Barkhausen criteria, negative resistance theory, frequency tuning methods and phase noise model are introduced.

2.2. Review of FBAR Resonators

Micro-electro-mechanical system (MEMS) resonators with hundreds of micrometers sizes, have a number of eigen frequencies and transduction mechanisms. Transduction mechanisms cause MEMS resonators to vibrate, if appropriate excitation signal which is of a frequency close to one of the eigen frequencies of MEMS resonators is input. According to the different implement approaches, the micromechanical and the acoustical, MEMS resonators can be divided into two categories. FBAR resonators are one kind of acoustical wave resonators.

2.2.1. Structure of FBAR Resonators

FBAR resonators are composed of one piezoelectric film and two metal electrodes, which employ metal-piezoelectric-metal structure, as shown in Fig. 2.1. FBAR is fabricated above Si substrate and two metal electrodes are always made of aurum (Au) or

chromium (Cr). For the piezoelectric layer, many piezoelectric materials such as aluminum nitride (AlN), zinc oxide (ZnO), or cadmium sulfide (CdS) can be explored. Considering the high acoustic wave velocity, low temperature coefficient and the possibility of CMOS compatibility, AlN is chosen in this research. The air gap is used to reduce the electromechanical coupling to the substrate to obtain high Q-factor.

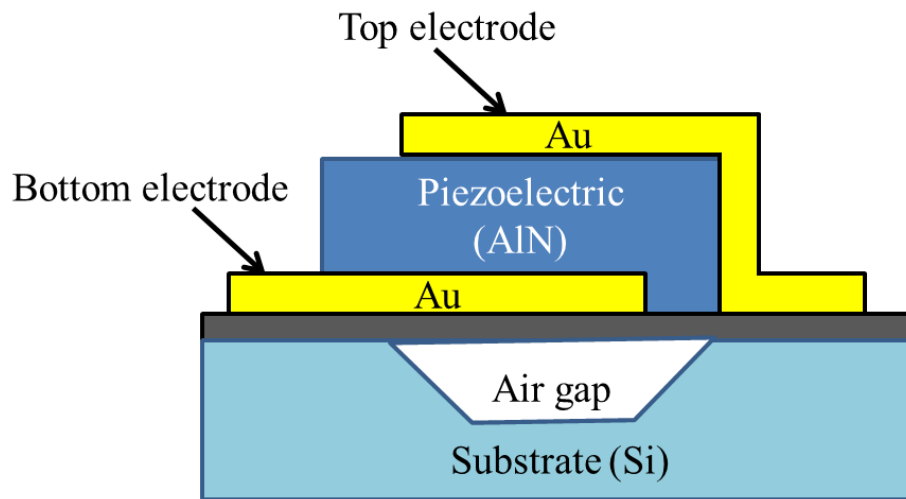


Fig. 2. 1 Structure of FBAR

2.2.2. Equivalent Circuit of FBAR Resonators

The equivalent circuit of FBARs can be represented by the Butterworth-Van-Dyke (BVD) model which is also suitable for crystal resonators and other MEMS resonators [27]. It is shown in Fig. 2.2 that the BVD model has two parallel branches which are called the static capacitance arm and the motional arm respectively. The static capacitance arm is composed of the parallel-plate capacitance C_0 formed between the top and bottom electrodes of FBARs while the motional branch is formed by the series motional inductance L_m , capacitance C_m , and resistance R_m , which relates to process-dependent parameters and material constants.

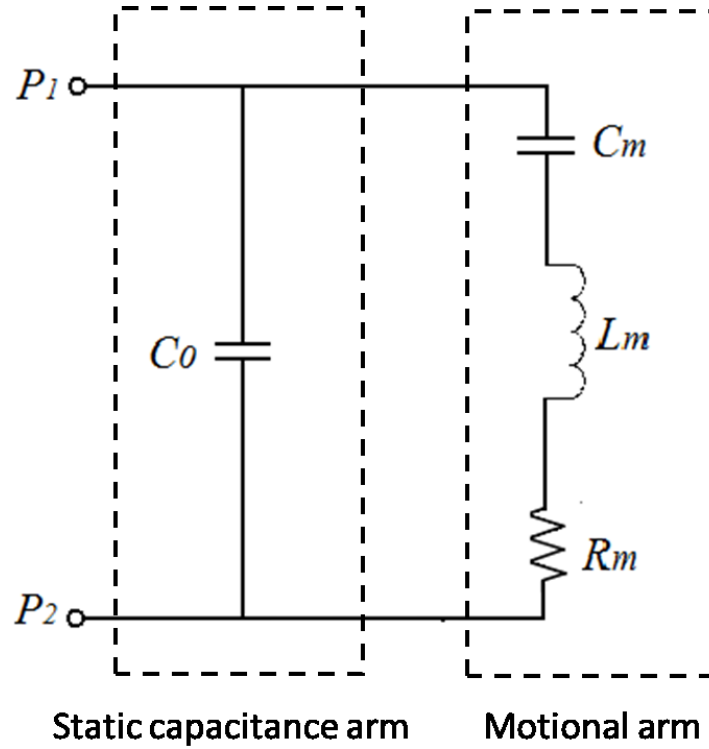


Fig. 2. 2 BVD model of FBAR

Because the two branches are connected in parallel, two resonance frequencies of FBARs, the series resonance frequency (f_s) and the parallel resonance frequency (f_p), are presented by the BVD model. The two resonance frequencies can be calculated by:

$$f_s = \frac{1}{2\pi\sqrt{L_m C_m}} \quad (2.1)$$

$$f_p = \frac{1}{2\pi\sqrt{L_m \left(\frac{C_m C_0}{C_m + C_0} \right)}} \quad (2.2)$$

The series resonance frequency f_s is always referred to as the resonance frequency, as the impedance at this frequency is minimized, while the parallel resonance frequency f_p

is often called the anti-resonance frequency, since the impedance at this frequency is maximum.

The parameters of BVD model can be calculate by follow [28]:

$$C_0 = \frac{\epsilon A}{t} \quad (2.3)$$

$$\frac{C_m}{C_0} = \frac{8k_{eff}^2}{N^2\pi^2} \quad (2.4)$$

$$L_m = \frac{v}{64f_s^3 \epsilon A k_{eff}^2} \quad (2.5)$$

$$R_m = \frac{\eta \epsilon}{16f_s \rho A v k_{eff}^2} \quad (2.6)$$

where A is the area of the parallel-plate capacitor; ϵ , t , ρ and v are the absolute permittivity, thickness, density, and speed sound of the piezoelectric material, respectively; N is the acoustic mode, and η is the acoustic viscosity related to the imaginary part of the wave vector; k_{eff}^2 is the piezoelectric coupling coefficient.

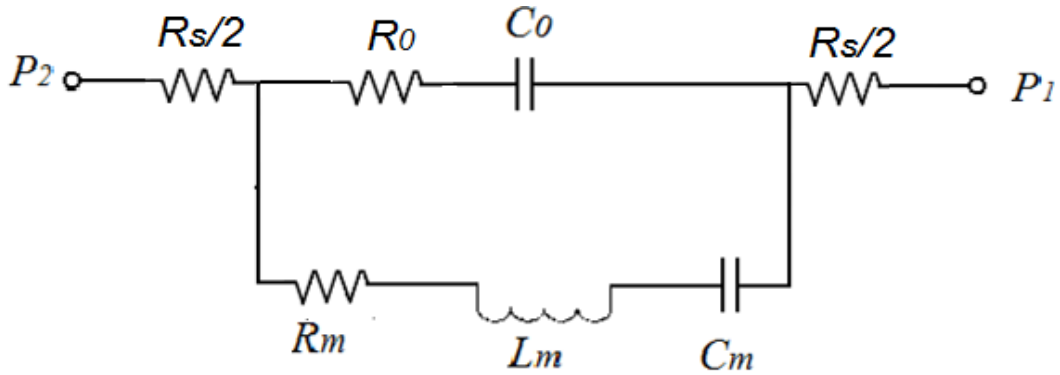
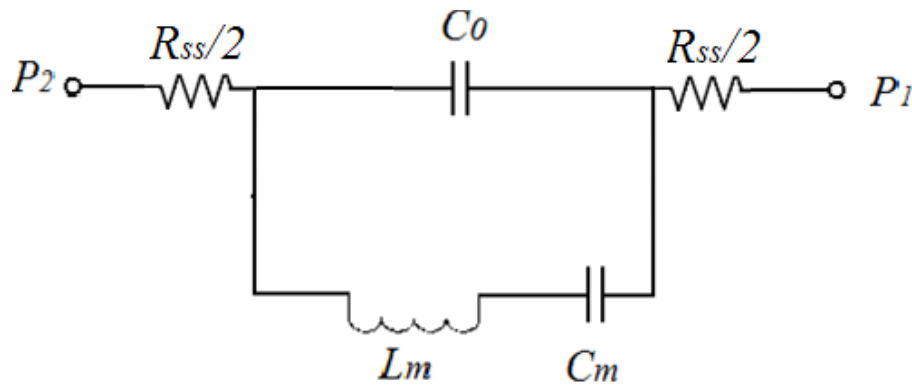


Fig. 2. 3 MBVD model of FBAR

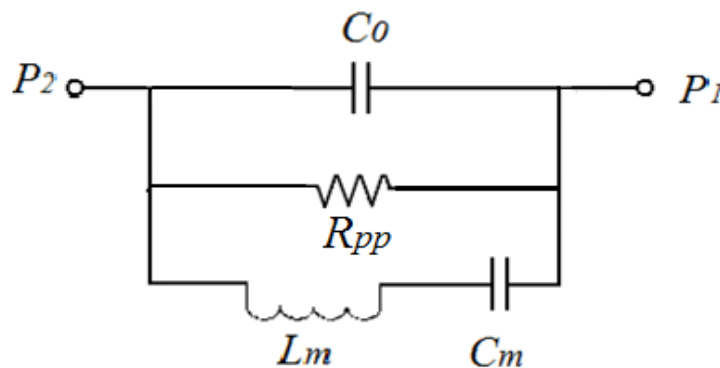
From the BVD model and (2.3) to (2.6), the physical constants of the process can be obtained. However, the modified Butterworth-Van-Dyke (MBVD) model [29] gives a

more realistic representation of FBARs, because it accounts for dielectric and ohm losses in the piezoelectric material and the transmission line by using resistances R_0 and R_s respectively, as shown in Fig. 2.3. The differences between the MBVD model and BVD model are in the parallel-plate capacitance arm, R_0 is serially connected to C_0 , and the two components of resistance $R_s/2$ are added, which corresponds to the bottom and top electrode line losses respectively.

At f_p and at f_s the MBVD model can also be simplified into a model with a single series resistance, R_{ss} and a single shunt resistance, R_{pp} , as shown in Fig.2.4.



(a)



(b)

Fig. 2. 4 Simplified model used only at f_s (a) and at f_p (b)

With the MBVD model, the impedance characteristic of FBARs can be depicted in Fig. 2.5. Thus the Q-factor at the series resonance frequency (Q_s) and the Q-factor at the parallel resonance frequency (Q_p) can be computed as:

$$\begin{aligned} Q_s &\approx f_s / \Delta f_s \\ Q_p &\approx f_p / \Delta f_p \end{aligned}$$

(2.7)

where Δf_s and Δf_p are the -3 dB frequency widths of the impedance magnitude of FBAR at f_s and f_p respectively. From experiment, it is known that the Q-factor of FBAR is always larger than 1000 [24-26].

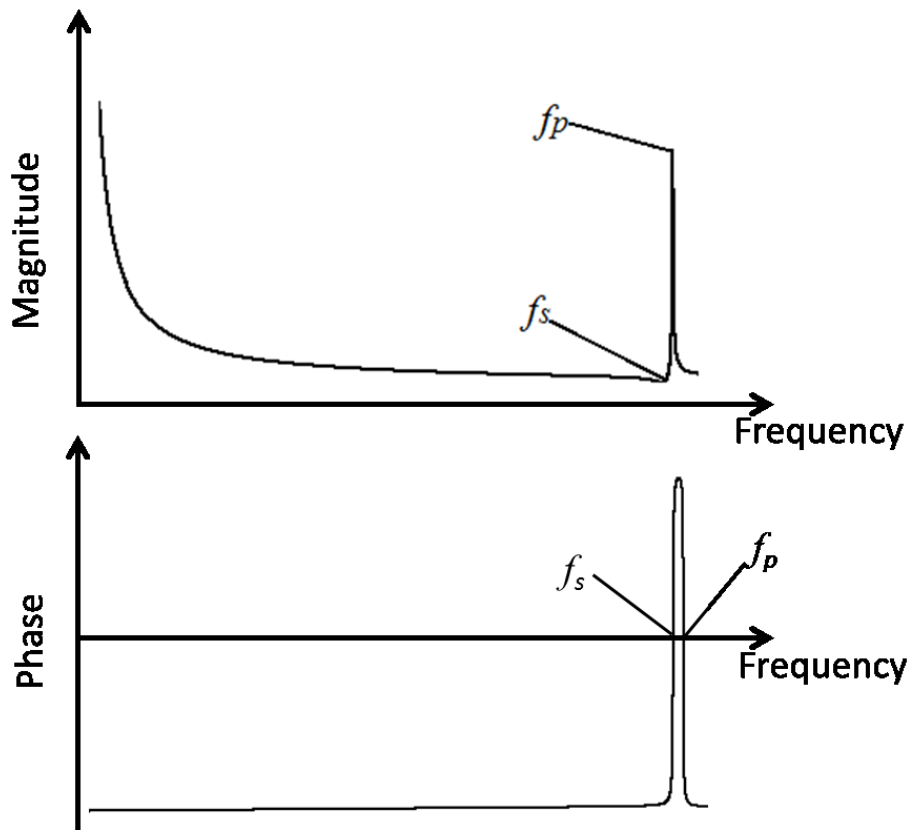


Fig. 2. 5 Magnitude and phase of FBAR impedance

2.3. Oscillator Fundamentals

In this subsection, it focuses on discussion of the oscillation condition and the phase noise model of oscillators.

2.3.1. Barkhausen Criteria and Negative Resistance Theory

In order to keep oscillator oscillate, it is necessary to satisfy the Barkhausen criteria [30]. The Barkhausen criteria are based on feedback systems. Fig. 2.6 shows an unity-gain negative feedback system, where $H(s)$ is called the feed-forward network.

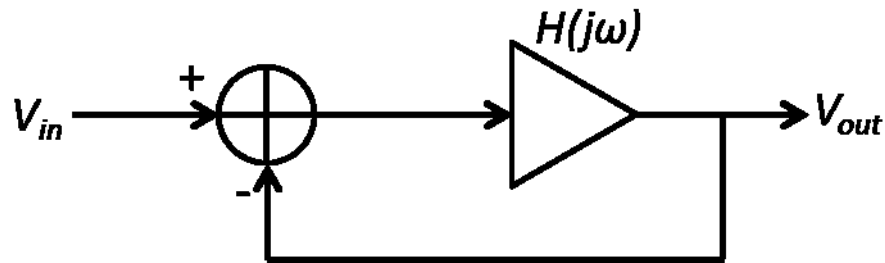


Fig. 2. 6 Unity-gain negative feedback system

Then the closed-loop gain of the system in Fig. 2.6 is

$$\frac{V_{out}}{V_{in}} = \frac{H(j\omega)}{1 + H(j\omega)} \quad (2.8)$$

If for a frequency ω_0 , $H(j\omega) = -1$, then the closed-loop gain approaches infinity at ω_0 .

Under this condition, if a little noise is input in this system, it will be amplified indefinitely and infinite output will be generated continuously which is also called oscillation. Actually, for the oscillation to begin, the condition $H(j\omega) \leq -1$ is necessary. This condition is able to resolve to the magnitude part and the phase shift part as follow:

$$H(j\omega) = -1 \quad (2.9)$$

$$\angle H(j\omega) = 180^\circ \quad (2.10)$$

These two conditions are called “Barkhausen criteria”.

It is worth notice that the second Barkhausen criterion (2.10) presents a frequency-dependent phase shift not a total phase shift. In Fig. 2.6, the system already produces a DC phase shift of 180° because of the negative feedback. Thus, the total phase shift is 360° not 180° .

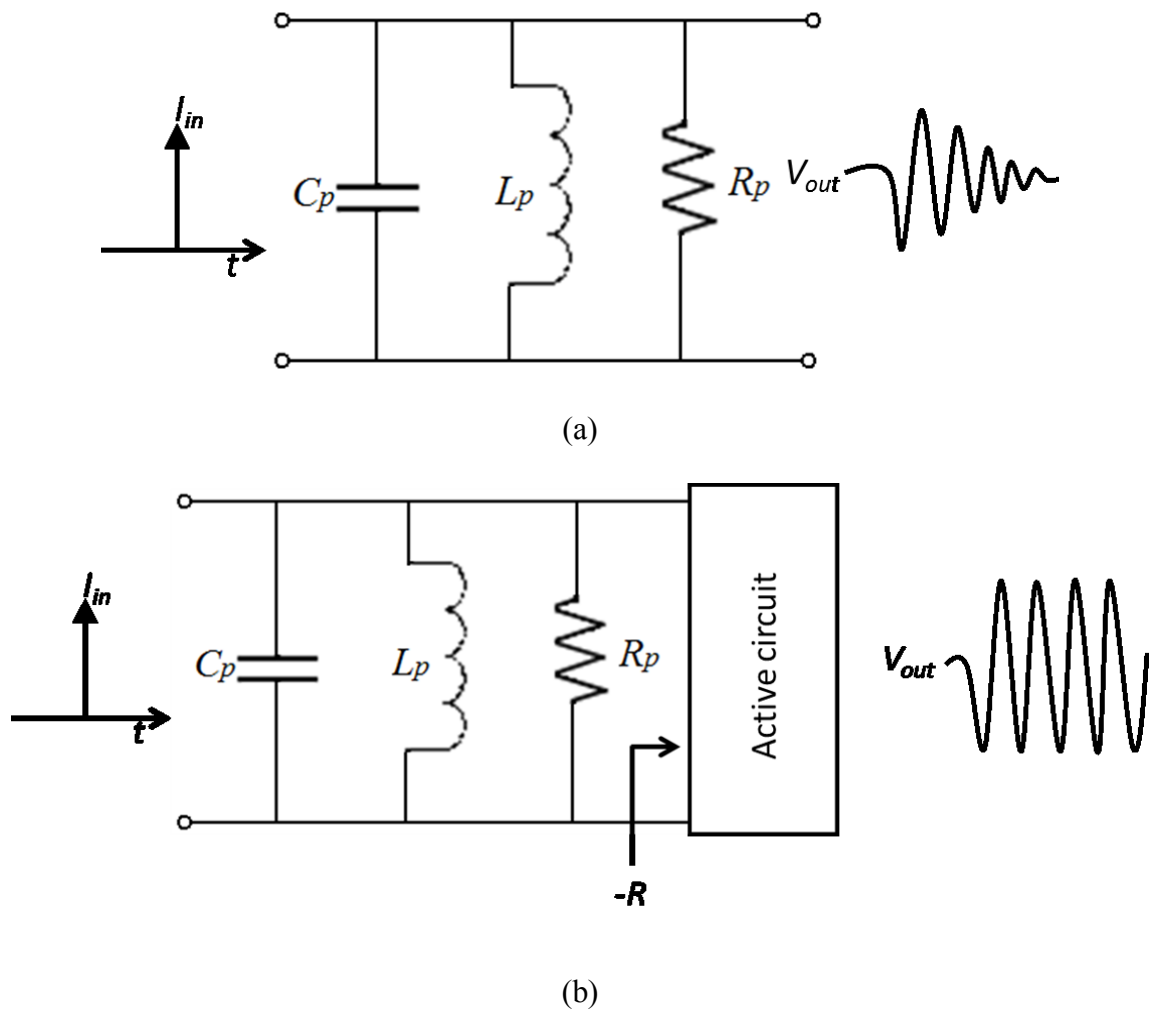


Fig. 2. 7 (a) Damped oscillation, (b) add a negative resistance provided by active circuit to cancel the loss of R_p

All analyses above are based on feedback systems, however, in practice another theory of “negative resistance,” [31] can provide an easier way to analysis and design an FBAR-VCO. Because at f_p FBAR also can be considered an equivalent inductor-capacitor in parallel, a simple parallel LC-tank is used to describe the negative resistance theory, as shown in Fig. 2.7. If a current impulse is input in this parallel LC-tank, the response is a damped oscillation because of the loss of R_p , as shown in Fig. 2.7 (a). If the loss of R_p is absolutely compensated by a negative resistance $-R$, which is usually composed of active circuit, satisfying $-R // R_p = \infty$, as shown in Fig. 2.7 (b), the LC-tank can oscillate indefinitely.

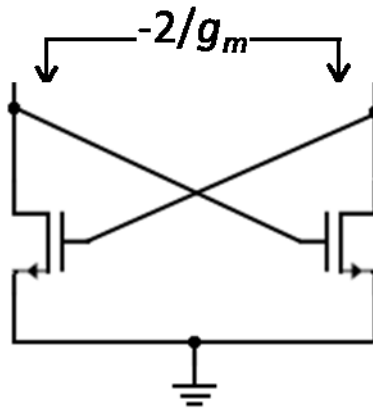


Fig. 2. 8 A NMOS cross-coupled pair based negative resistance generation circuit

A NMOS cross-coupled pair based negative resistance generation circuit is shown in Fig. 2.8. It can be proved that the negative resistance of the circuit in Fig.2.8 is equal to $-2/g_m$, where g_m is the trans-conductive of transistors. If $R_p - 2/g_m \geq 0$, the AC power provided by the negative resistance generation circuit is larger than loss R_p , the oscillation will start and the oscillation amplitude will be increasing. When the amplitude is large enough, the transistors will be cutoff in a part of each period, which makes the loss is equal

to the AC power provided by the negative resistance generation circuit, and make the oscillation amplitude become stable.

2.3.2. Frequency Tuning Method of FBAR Oscillator

It has been known from (2.2) the parallel resonance frequency f_p is decided by L_m , C_m and C_0 . Therefore, the only method of changing f_p is that connecting a tunable capacitor C_1 in parallel and changing the capacitance of it, as shown in Fig 2.9. In this situation, f_p is decided by:

$$f_p = \frac{1}{2\pi \sqrt{L_m \left(\left(\frac{C_m C_0}{C_m + C_0} \right) // C_1 \right)}} \quad (2.11)$$

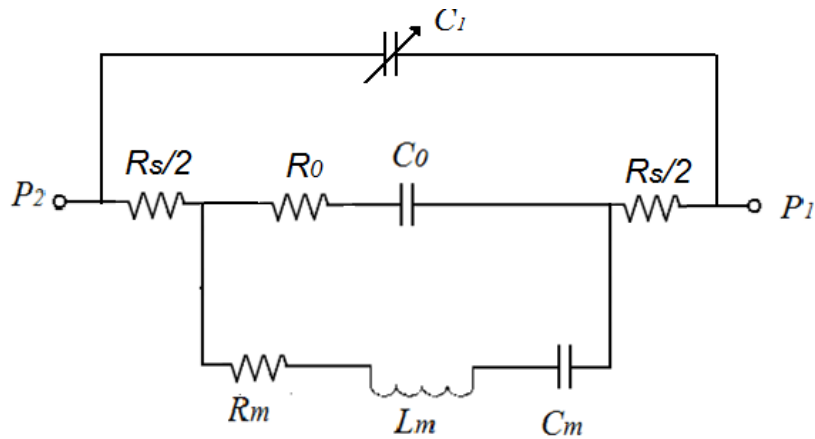


Fig. 2. 9 FBAR with tunable capacitor in parallel

Normally, two methods can be used to realize the tunable C_1 . The first one uses digital control logic employing a capacitor bank in which each capacitor is controlled by an NMOS switch, as shown in Fig 2.10. The capacitance is binary weighting which makes the N bits capacitor bank provide 2^N discrete frequencies.

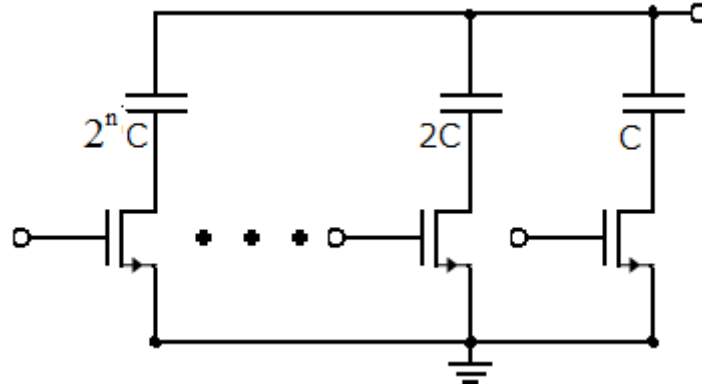


Fig. 2. 10 N bits capacitor bank

Although the capacitor bank can provide several discrete frequencies, in many VCOs, the oscillation frequency is the linear function of the control voltage,

$$\omega_{out} = \omega_c + K_{VCO}V_{cont} \quad (2.12)$$

where, ω_c is the oscillation frequency when the control voltage $V_{cont}=0$; K_{VCO} is the gain of VCO.

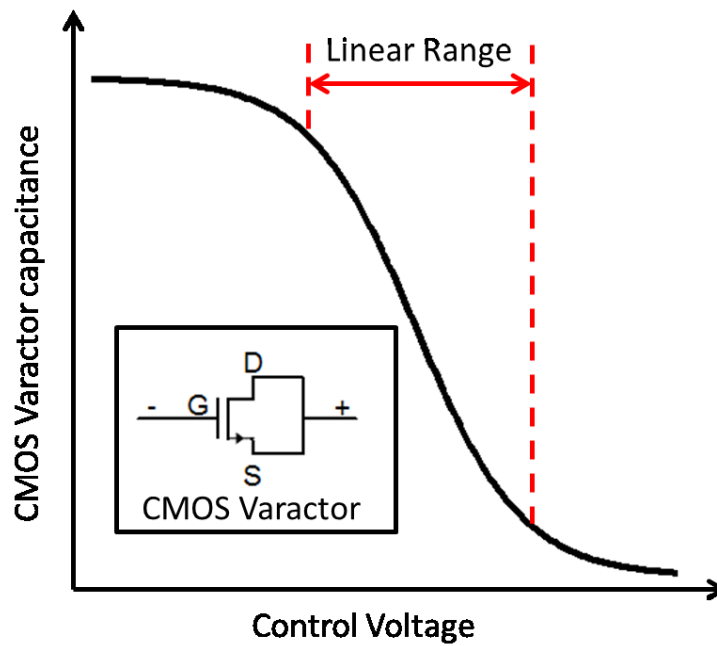


Fig. 2. 11 Capacitance-voltage characteristic of CMOS varactor

In this situation, CMOS varactors are needed to be used to realize tunable C_l . In standard CMOS process, varactors are realized by CMOS transistors. A CMOS varactor and its capacitance-voltage characteristic are shown in Fig. 2.11. When the drain and source of transistor is connected together, the capacitance between the gate and the drain and source is changing with the control voltage.

2.3.3. Phase Noise Model of FBAR oscillator

Based on the analyses above, because at f_p FBAR can be considered an equivalent inductor-capacitor-loss resistor in parallel, the phase noise model of LC oscillators is able to be used in the FBAR oscillator analyses. Assume the negative resistance generator is noise-free, thus the loss resistor is the only noise source of the circuit. Considering the thermal noise of resistor and the definition of phase noise, the phase noise of an ideal oscillator is [32]

$$L(\Delta\omega) = 10 \log \left(\frac{2kT}{P_{sig}} \left(\frac{\omega_c}{2Q\Delta\omega} \right)^2 \right) \quad (2.13)$$

where, $L(\Delta\omega)$ is the phase noise at frequency offset $\Delta\omega$; k and T are constants; P_{sig} is the oscillation power. It is shown that the phase noise is inversely proportional to the second power of offset frequency, however actually the relationship between experiment phase noise and offset frequency is much different with the ideal model, because of other noise sources such as the noise of negative resistance generator and the $1/f$ noise of CMOS. Considering these factors, Leeson proposed a famous phase noise model [32], as shown in (2.14) and Fig.2.12. In Leeson phase noise model, phase noise is separated by three regions: the $1/(\Delta\omega)^3$ region in which the phase noise is proportional to $1/(\Delta\omega)^3$; the $1/(\Delta\omega)^2$

region in which the phase noise is proportional to $1/(\Delta\omega)^2$; and noise floor. An experiment factor F is used to account for the increased noise in the $1/(\Delta\omega)^3$ region, and ω_{1/f^3} is the boundary between the $1/(\Delta\omega)^2$ region and the $1/(\Delta\omega)^3$ region.

$$L(\Delta\omega) = 10 \log \left[\left(\frac{2FkT}{P_{sig}} \left(1 + \frac{\omega_c}{2Q\Delta\omega} \right)^2 \right) \left(1 + \frac{\omega_{1/f^3}}{\Delta\omega} \right) \right] \quad (2.14)$$

From the Lesson model, it is known that increasing the Q-factor of resonators is an effective method to improve the phase noise of VCO. That is the reason that high Q-factor FBAR resonators are employed in our design to take place of LC-tanks.

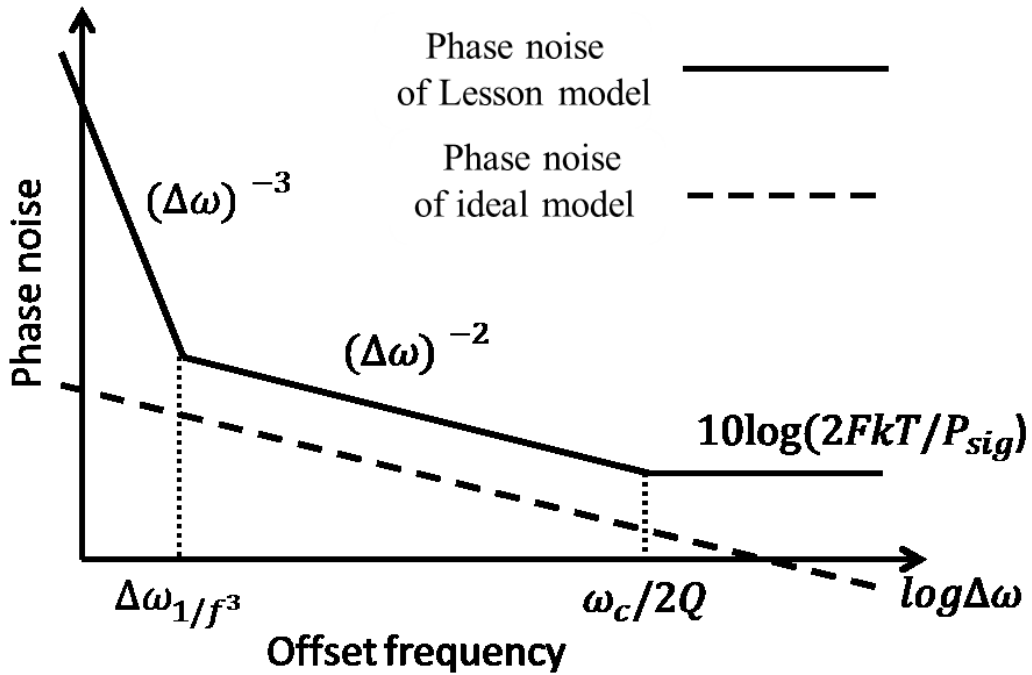


Fig. 2. 12 Phase noise curve of Lesson model

2.4. Conclusion

In this chapter, firstly the review of FBAR resonators including the structure and the equivalent circuit is presented briefly. Then the oscillator fundamentals included

Barkhausen criteria, negative resistance theory, frequency tuning methods are introduced. Finally, the phase noise model is presented, which makes us know that good phase noise performance is able to obtain if using high Q-factor FBAR resonators.

Chapter III

Pierce and Inverter FBAR-DCO

3.1. Introduction

In this chapter, the design and analysis of two kinds of single ended FBAR-DCO is presented. The first one is called Pierce FBAR-DCO which employs Pierce three-point architecture [33] and the second one is inverter architecture base FBAR-DCO. These two kinds of architecture have the advantages of simplicity and low power consumption and low phase noise.

3.2. Pierce FBAR-DCO

3.2.1 Pierce FBAR-DCO Design and Analyses

In this design, the parameters of the adopted FBAR are shown in Fig. 3.1. The parallel resonance frequency is 2.49 GHz and the series resonance frequency is 2.44 GHz. The parameter values can be obtained from (2.3)-(2.6). The Q_p and the Q_s of the FBAR, calculated by (2.7), are about 3550 and 175, respectively.

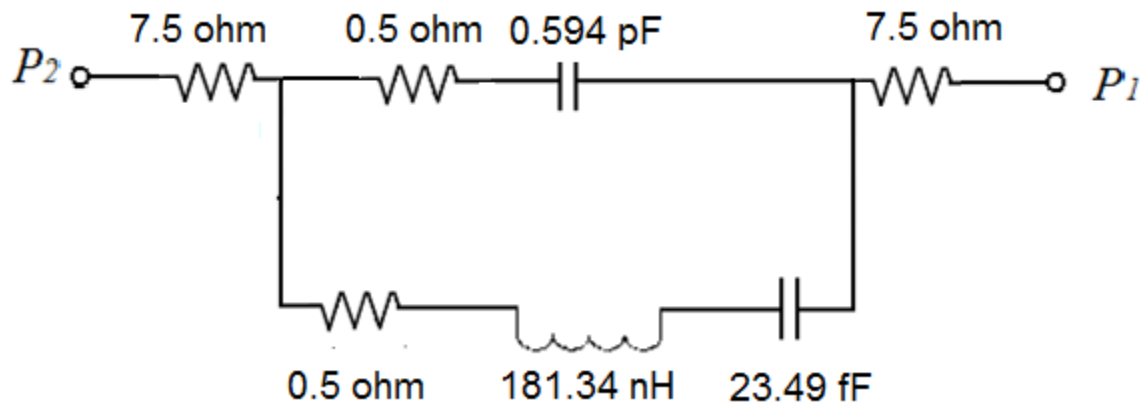


Fig. 3. 1 Parameters of the adopted FBAR

The proposed Pierce FBAR-DCO is shown in Fig.3.2. The transistor M_2 is used to generate negative resistance, and a gate bias voltage V_{bias} keeps M_2 in saturation region through a large resistor R_{bias} . The bias current of the whole circuit is provided by transistor M_3 , and a 5 bits capacitor bank is used to provide wide tuning range. In addition, an LC-tank based buffer is used to keep large amplitude output and prevent phase noise deterioration.

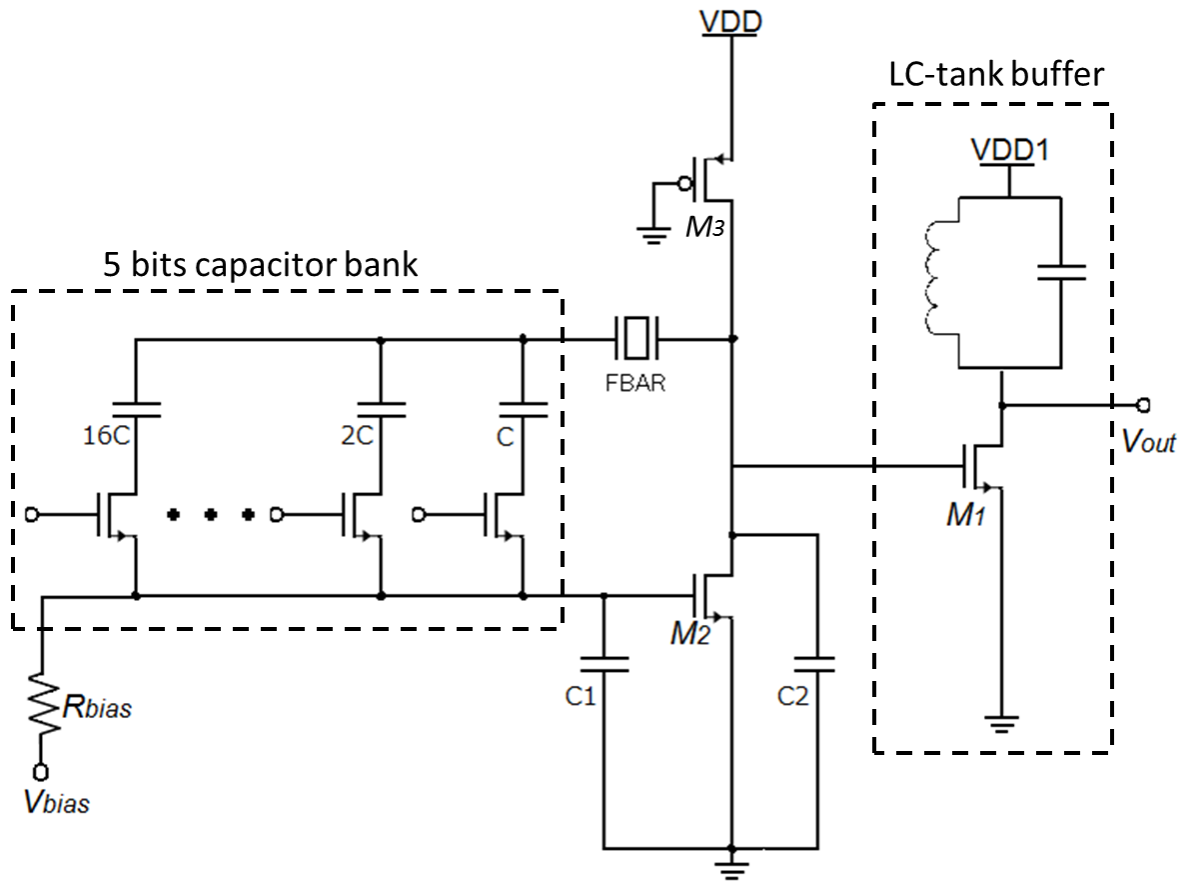


Fig. 3. 2 Circuit of the proposed Pierce FBAR-DCO

Ignoring the effect of capacitor bank and LC-tank buffer and considering all transistors as ideal transistors, the equivalent circuit of the proposed Pierce FBAR-DCO is shown in Fig. 3.3.

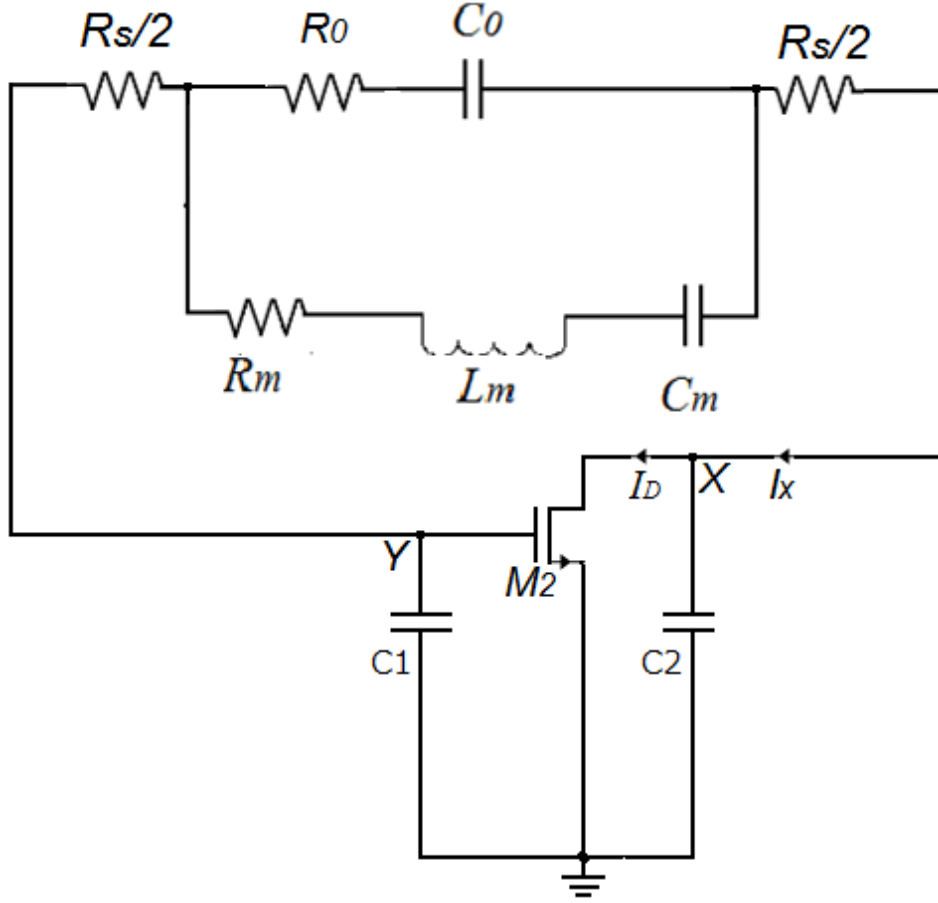


Fig. 3. 3 Equivalent circuit of the proposed Pierce FBAR-DCO

From Fig. 3.3, the drain current of M_2 is

$$I_D = V_{XY} g_m = (-I_X / (j\omega C_1)) g_m \quad (3.1)$$

And then the voltage between the node X and the node Y is

$$V_{XY} = \left(I_X - \frac{I_X}{j\omega C_1} g_m \right) \frac{1}{j\omega C_1} + \frac{I_X}{j\omega C_1} \quad (3.2)$$

Therefore, the input impedance between the node X and the node Y can be obtained by rewriting (3.2) as

$$Z_{XY} = -\frac{g_m}{C_1 C_2 \omega^2} + \frac{1}{j\omega C_2} + \frac{1}{j\omega C_1} \quad (3.3)$$

It is shown that the real part of Z_{XY} is a negative resistance and the imaginary part is the series impedance of C_1 and C_2 . Thus, the equivalent circuit can be simplified to Fig. 3.4,

where R_n is equal to $-\frac{g_m}{C_1 C_2 \omega^2}$ and C_n is equal to $\frac{C_1 C_2}{C_1 + C_2}$.

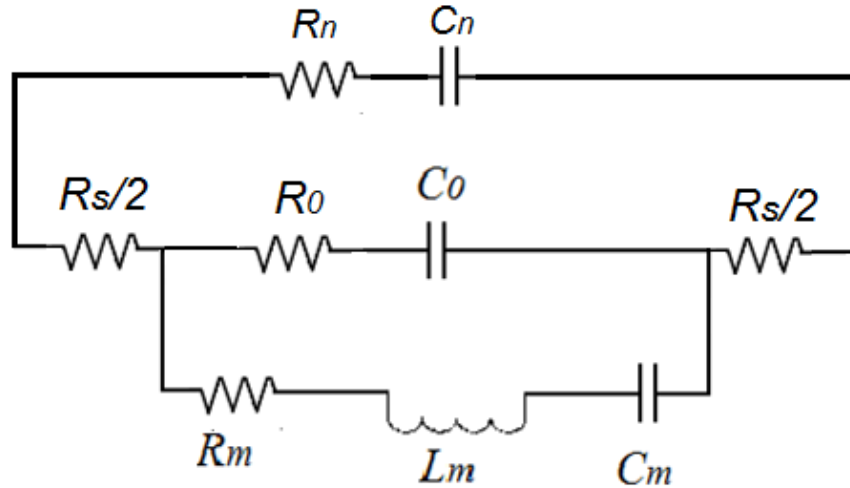


Fig. 3. 4 Simplified equivalent circuit

The total admittance of the circuit is

$$Y_{total} = \frac{1}{Z_{FBAR}} + \frac{1}{Z_{XY}} \quad (3.4)$$

If at one frequency at which the imaginary part of $Y_{total}=0$, also can be written as

$$imag\left(\frac{1}{Z_{FBAR}}\right) + imag\left(\frac{1}{Z_{XY}}\right) = 0 \quad (3.5),$$

the real part of Y_{total} is

$$real(Y_{total}) = real\left(\frac{1}{Z_{FBAR}}\right) + real\left(\frac{1}{Z_{XY}}\right) < 0 \quad (3.6),$$

it means that the loss of FBAR is completely compensated by the negative resistance generated by transistors and the circuit starts oscillate.

As shown in Fig. 3.5, because at f_{osc} the admittance of the proposed Pierce FBAR-DCO satisfies the conditions in (3.5) and (3.6), the oscillator can operate at f_{osc} . Oscillation judgment can also be done by the stability analysis simulation. Fig. 3.6 shows the small signal loop gain and phase shift of proposed Pierce FBAR-DCO. It is indicated that in the frequency about 2.45 GHz, the loop gain is larger than zero and the total phase shift of the circuit is zero, satisfying the Barkhausen criteria.

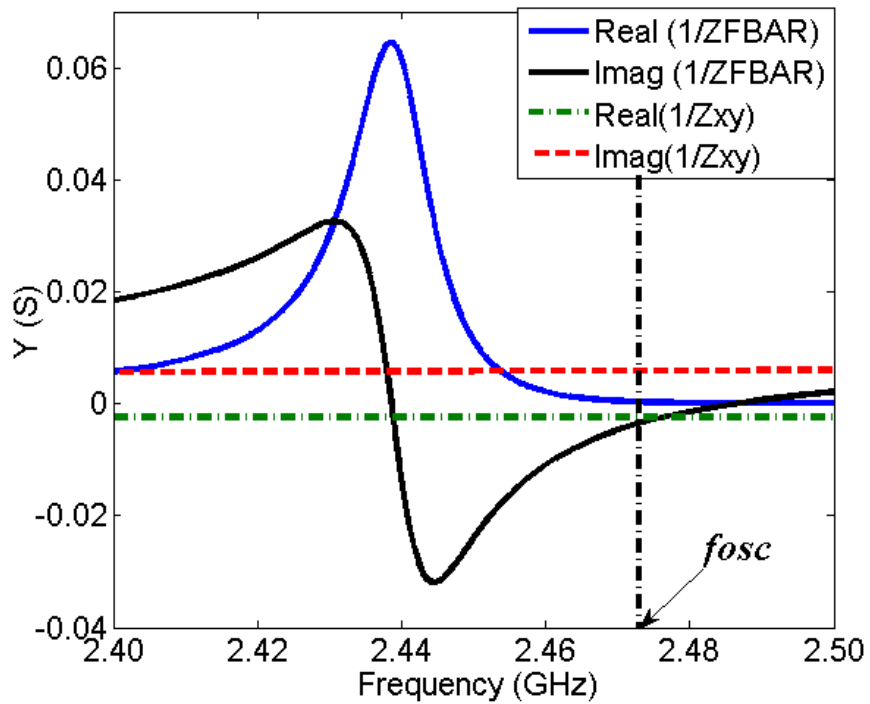


Fig. 3. 5 Admittance of the proposed Pierce FBAR-DCO

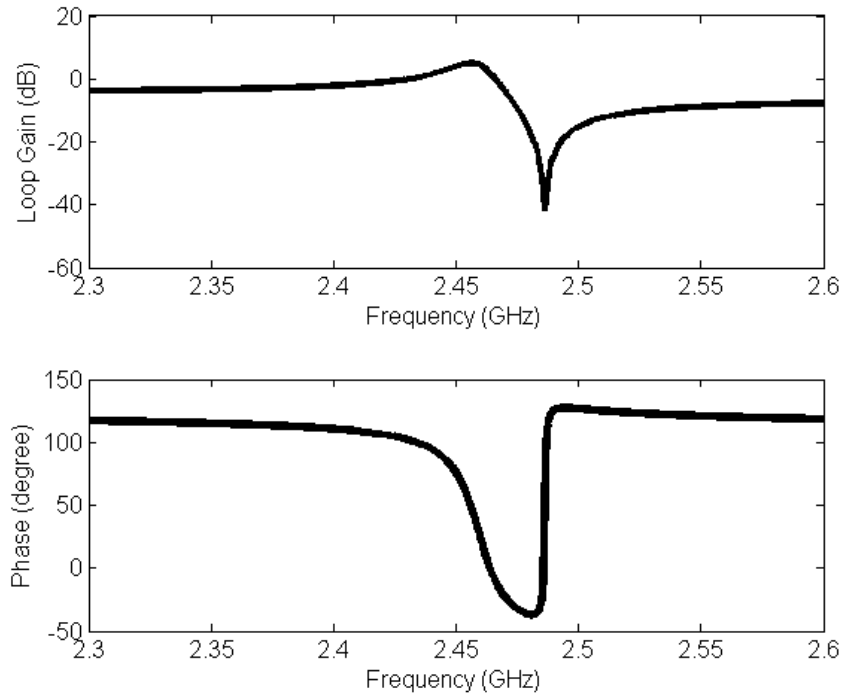


Fig. 3. 6 Small signal loop gain and phase of proposed Pierce FBAR-DCO

3.2.2 Simulation Result

The proposed Pierce FBAR-DCO is designed in TSMC 0.18 μm CMOS technology. The frequency tuning curve is shown in Fig. 3.7. In the proposed design, frequency tuning is realized by a 5 bits capacitor bank. The 5 bits capacitor bank provide a tuning range about 10 MHz. Compared to LC-VCO, the tuning range of FBAR oscillator is always narrow, because FBAR shows inductance characteristic only between f_s and f_p , and the frequency difference of f_s and f_p is very small.

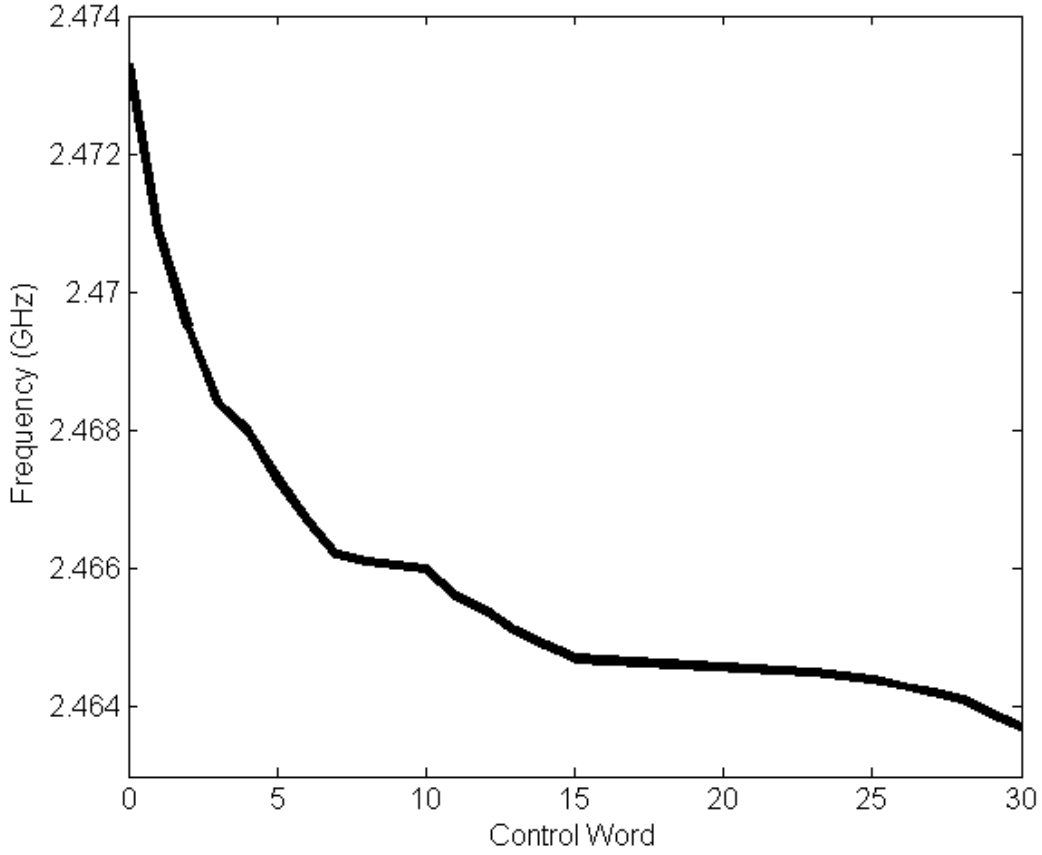


Fig. 3. 7 Tuning curve of the proposed FBAR-DCO

The output waveform is shown in Fig. 3.8 and Fig. 3.9 is the phase noise performance. It is indicated that with 0.65 V voltage supply, the peak to peak voltage of the output reached 0.6 V, and the phase noise is about -148 dBc/Hz at 1 MHz offset frequency. Compared to LC-VCO, the phase noise has been improved about 20dB. The FOM is able to be calculated by [34]

$$FOM = L(\Delta f) - 20\log\left(\frac{f_0}{\Delta f}\right) + 10\log\left(\frac{P_{DC}}{1mW}\right) \quad (3.7)$$

where $L(\Delta f)$ is the phase noise at the offset frequency from the oscillation frequency $f_0=2.46$ GHz, and P_{DC} is the DC power consumption. Thus, the FOM is about -210.36 dB.

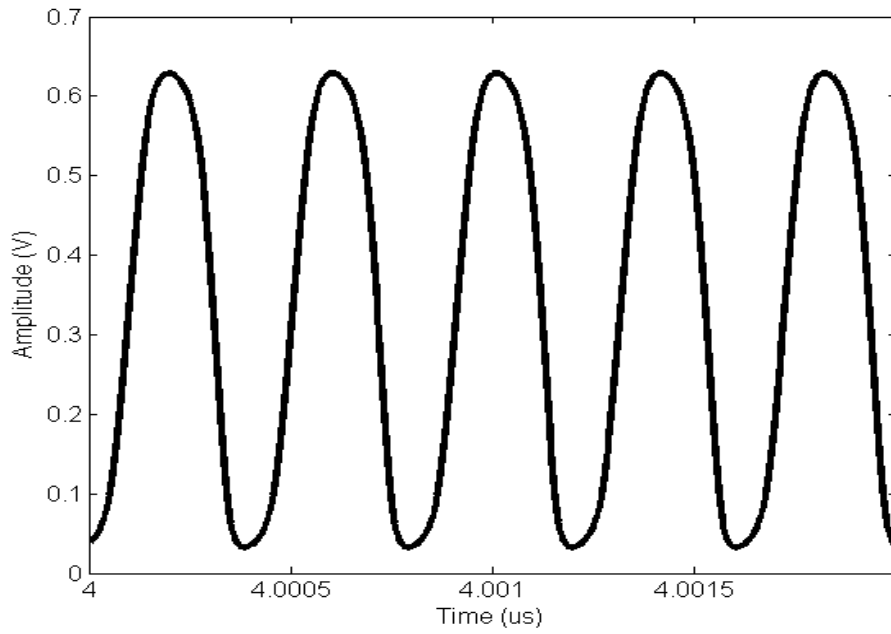


Fig. 3. 8 Output waveform of the proposed Pierce FBAR-DCO

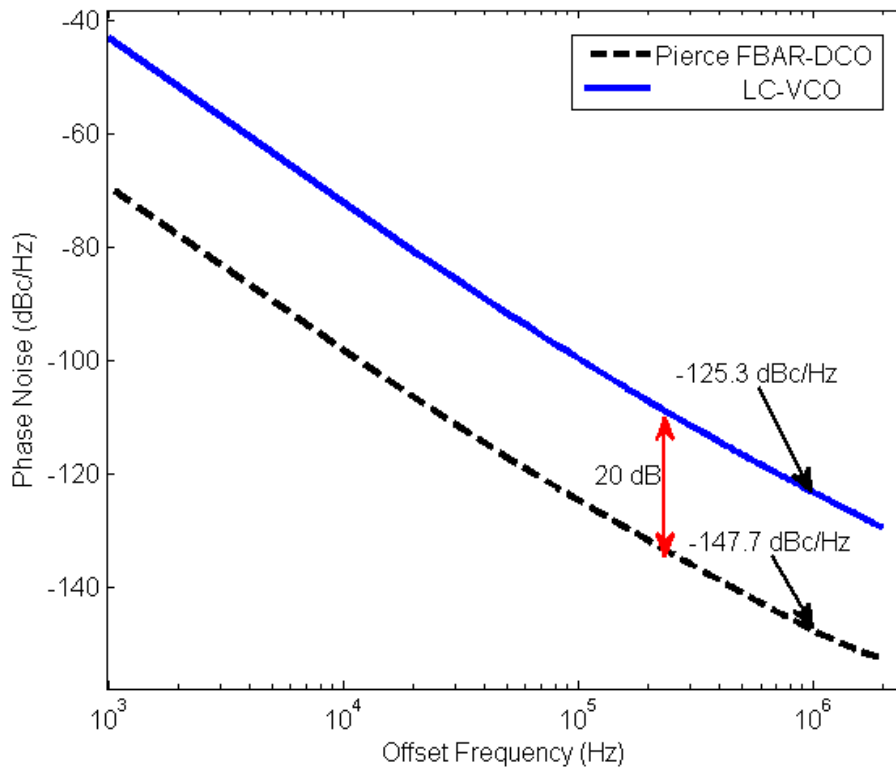
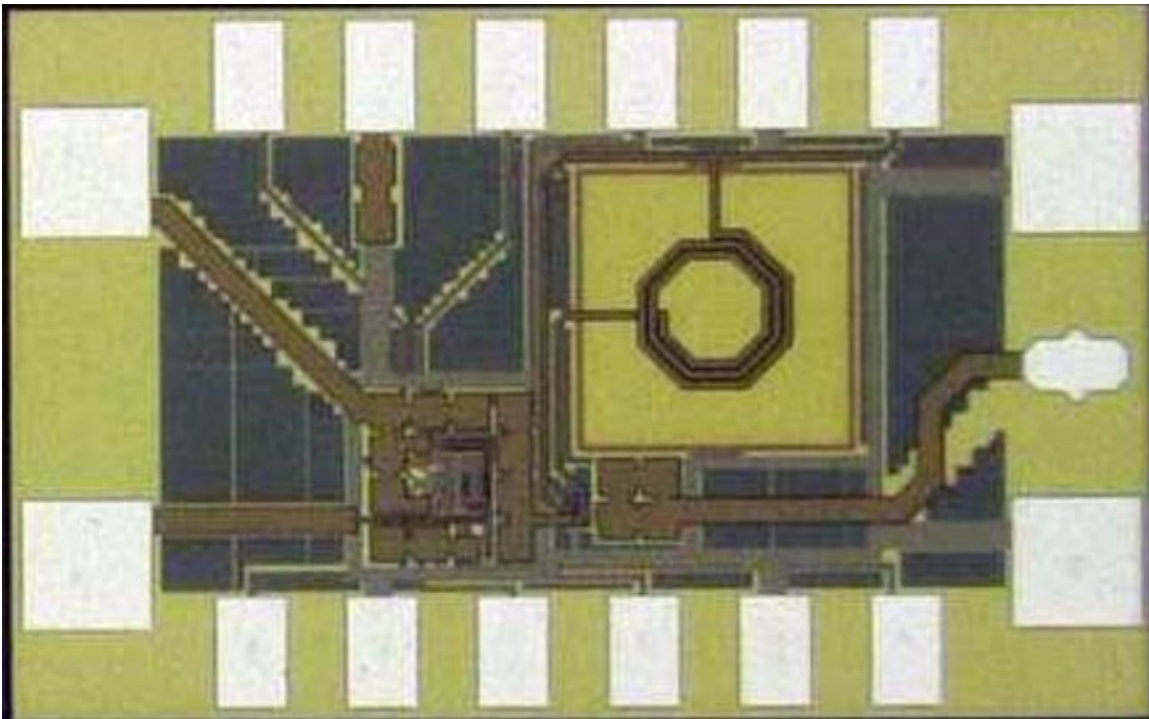


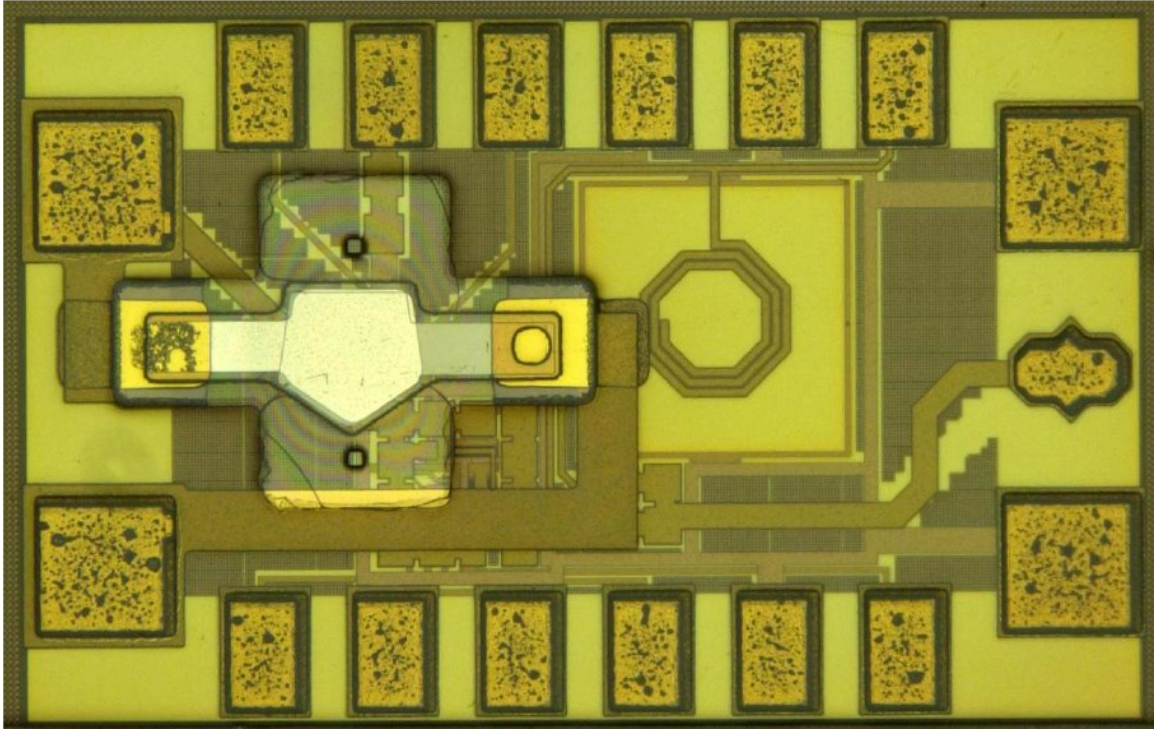
Fig. 3. 9 Phase noise comparison between the proposed FBAR-DCO and LC-VCO

3.2.3 Chip Fabrication

The proposed Pierce FBAR-DCO was fabricated in TSMC 0.18 μm CMOS technology. Chip photograph is shown in Fig. 3.10 (a), where the size including pads is 850 μm \times 550 μm . When integrating FBAR to the chip, we employed monolithic FBAR-CMOS integration method [35] instead of using bonding wire, directly integrating FBAR above CMOS substrate, to reduce the parasitic inductance between FBAR and CMOS pads and not increase the size of the final chip, as shown in Fig. 3.10 (b). However, the chip was failed because the measured R_m of the FBAR is as high as 550 Ohm. In the condition of the high R_m , the FBAR doesn't have a resonance around 2.4 GHz.



(a)



(b)

Fig. 3. 10 Photograph of Pierce FBAR-DCO (a) without FBAR,
(b) with FBAR integrated

3.3. Inverter based FBAR-DCO

3.3.1 Inverter based FBAR-DCO Design and Analyses

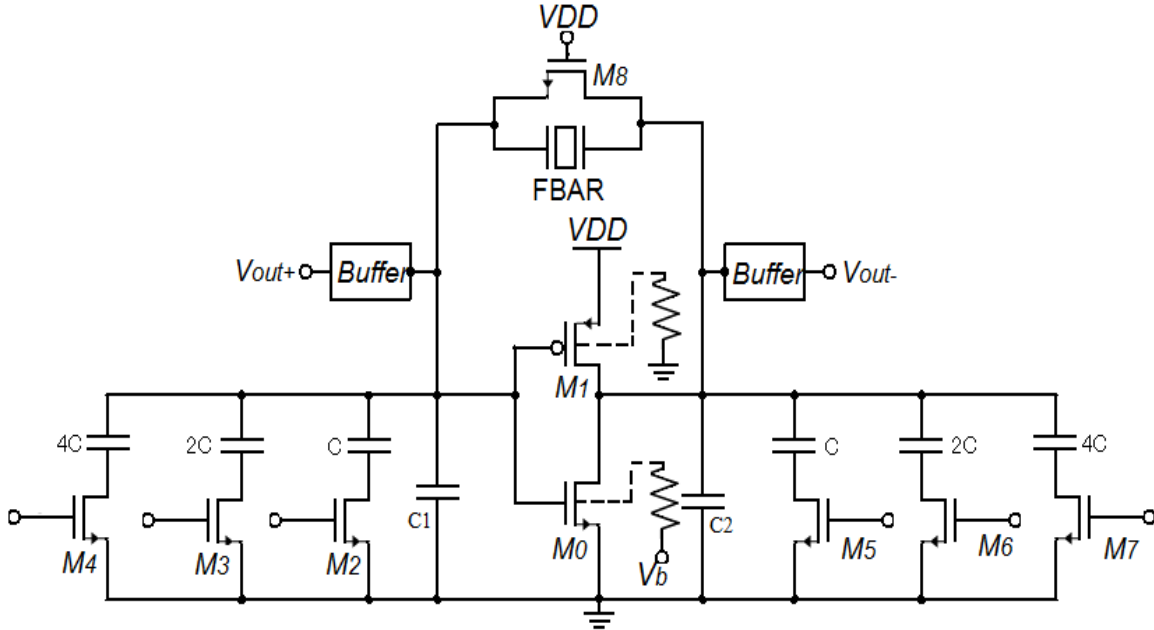


Fig. 3. 11 Circuit of the proposed inverter based FBAR-DCO

The proposed inverter based FBAR-DCO is shown in Fig.3.11. In the proposed FBAR-DCO, PMOS transistor M_1 and NMOS transistor M_2 constitutes an inverter and M_8 is kept in transistor region as a large resistor to provide gate bias voltage. Transistors (M_2 - M_7) make up a 3 bits capacitor bank. In this architecture, both M_1 and M_2 are used to generate negative resistance and the current of the circuit is reused. The generated negative resistance can be described by modifying (3.3) to

$$-\frac{g_{pm} + g_{nm}}{C_1 C_2 \omega^2} + \frac{1}{j\omega C_2} + \frac{1}{j\omega C_1} \quad (3.8)$$

where g_{pm} and g_{nm} are the trans-conductance of PMOS transistors and NMOS transistors respectively. Therefore, the generated negative resistance is $-\frac{g_{pm} + g_{nm}}{C_1 C_2 \omega^2}$. Compared to the previous one in Fig.3.2, It is clear that the inverter based FBAR-DCO can generate larger negative resistance, with same bias current.

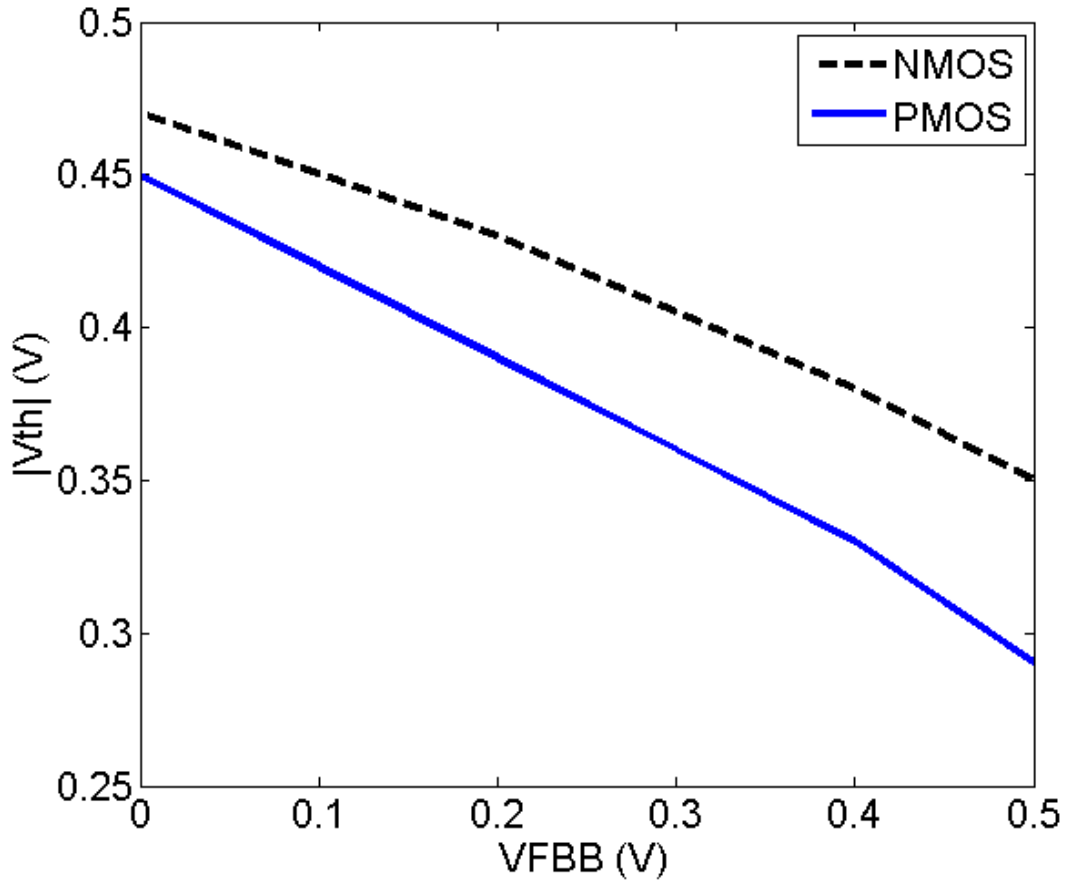


Fig. 3. 12 Curve of $|V_{th}|$ - VFBB

In order to reduce the power consumption, forward body bias (FBB) technique is employed in the proposed design. Unlike normal connection of transistors, in FBB technique, both the bodies of PMOS and NMOS transistors are connected to a low bias

voltage (V_{FBB}) to reduce the threshold voltage of transistors (V_{th}). It is usually used in the design of high-speed prescaler to reduce power consumption and increase the operation frequency [36]. The curve of $V_{th}-V_{FBB}$ for 0.18 μm CMOS transistors is shown in Fig. 3.12. As can be seen, the threshold voltage declines as the forward body bias voltage increases. In the proposed circuit, the bodies of PMOS and NMOS transistors are connected to bias voltage respectively through large resistors. The purpose of large resistors between the bodies of transistors and bias voltage is to prevent from excessively high bias voltage to avoid large leakage current. With connecting the body bias voltage, the $|V_{th}|$ of PMOS is decrease to 350 mv, and the V_{th} of NMOS is decrease to 400 mv. Finally, benefit from the FBB technique, the proposed circuit can work under 1 V voltage supply with 0.5 mA current consumption.

3.3.2 Simulation Result

The proposed inverter based FBAR-DCO is designed in TSMC 0.18 μm CMOS technology. The output waveform is shown in Fig. 3.13 and Fig. 3.14 is the phase noise performance. It is indicated that with 1.0 V voltage supply and 0.5 mA current consumption the proposed DCO operates at 2.48 GHz and the peak to peak voltage of the output reached 0.8 V; the phase noise is about -139.4 dBc/Hz at 1 MHz offset frequency and the FOM is about -210.50 dB.

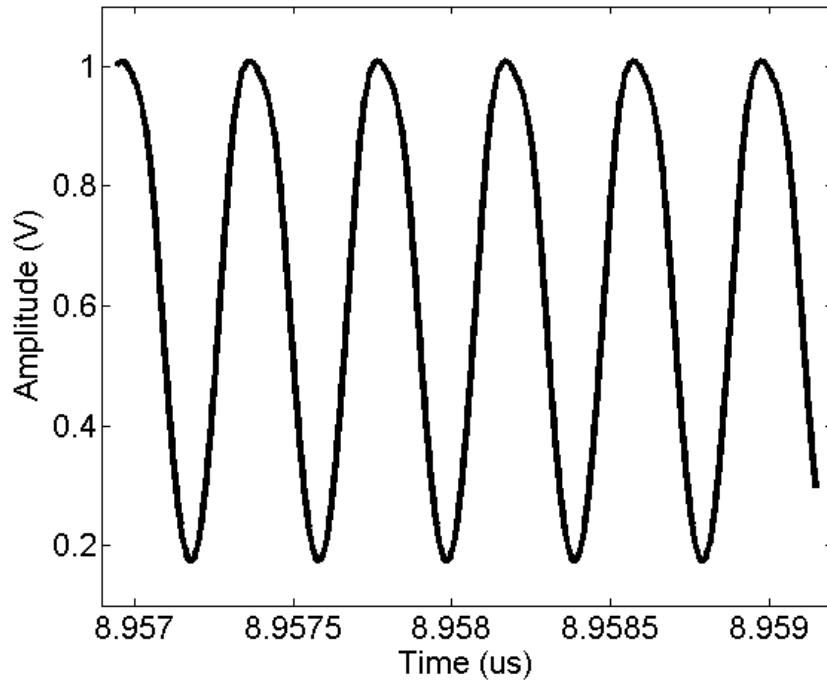


Fig. 3. 13 Output waveform of the proposed inverter based FBAR-DCO

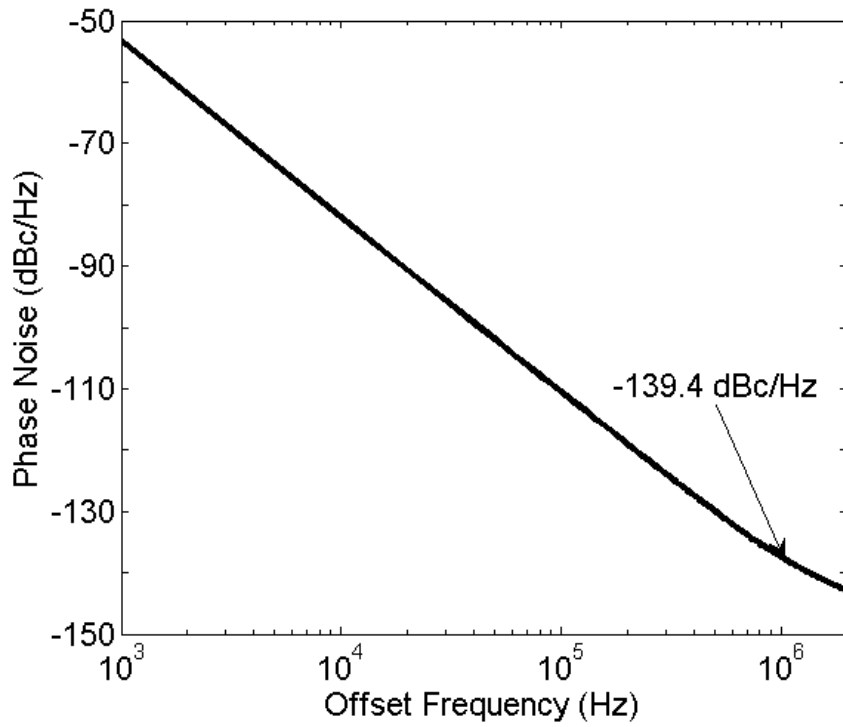


Fig. 3. 14 Phase noise of the proposed inverter based FBAR-DCO

3.3.3 Chip Fabrication

The proposed inverter based FBAR-DCO was fabricated in TSMC 0.18 μm CMOS technology. Chip photograph is shown in Fig. 3.15, where the size including pads is 850 μm \times 750 μm . The monolithic FBAR-CMOS integration method was also used in this fabrication. It is a pity that the chip was failed either because the parallel impedance of FBAR is decreased too much as the measured R_m of the FBAR, which is about 17 ohm, is too high for an FBAR resonator.

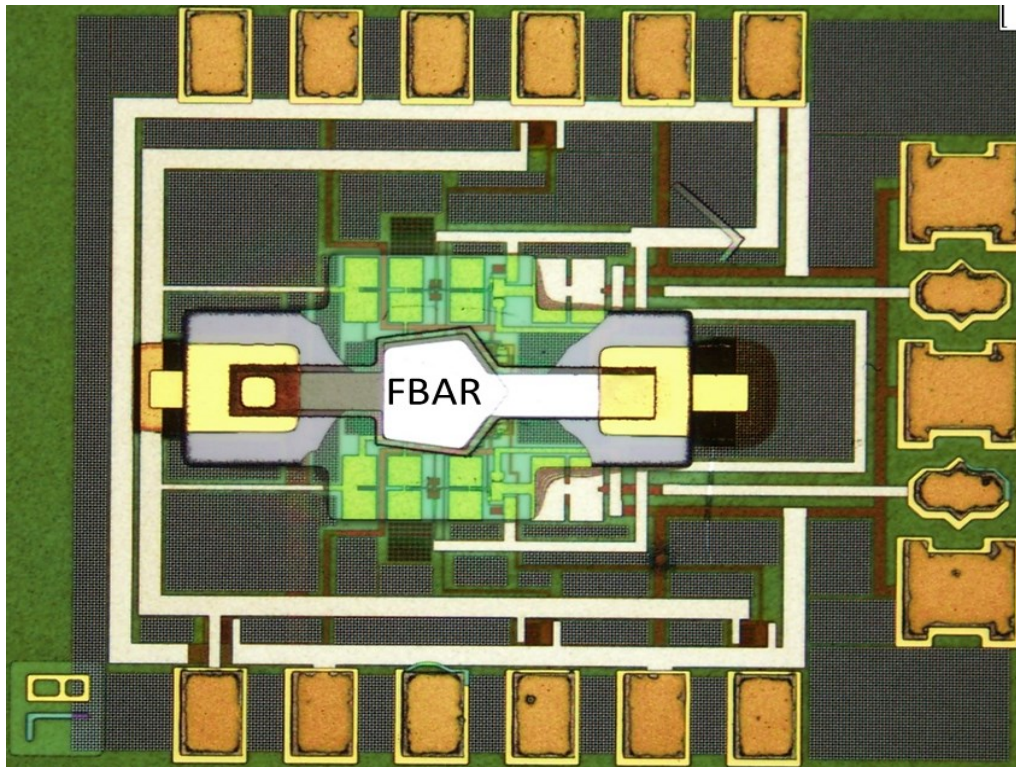


Fig. 3. 15 Photograph of inverter based FBAR-DCO

3.4 Conclusion

In this chapter, a Pierce FBAR-DCO and an inverter based FBAR-DCO are presented. The circuit design is described and the oscillation condition is analyzed in detail.

The post-layout simulation results show that both two FBAR-DCO have low power consumption and low phase noise. Table 3.1 shows the comparison between the two proposed FBAR-DCO and other published VCO. It is clear that the proposed FBAR-DCOs have better FOMs.

Table 3.1 Comparison with other published oscillators

	Post-layout simulation result of proposed Pierce FBAR-DCO	Post-layout simulation result of proposed inverter FBAR-DCO	[24]	[25]	[26]
Process	0.18 μ m CMOS	0.18 μ m CMOS	0.25 μ m BiCMOS	0.13 μ m CMOS	0.18 μ m CMOS
Vdd (V)	0.65	1.0	2.4	1.0	1.8
f_0 (MHz)	2460	2480	2100	1575	1500
Power (mW)	3.25	0.5	58	0.5	3.78
Tuning range (MHz)	10	9	37	1.35	1
$L(\Delta f)$ @ 1MHz (dBc/Hz)	-147.7	-139.4	-144	-138	-142
FOM	-210	-210	-193	-204	-200

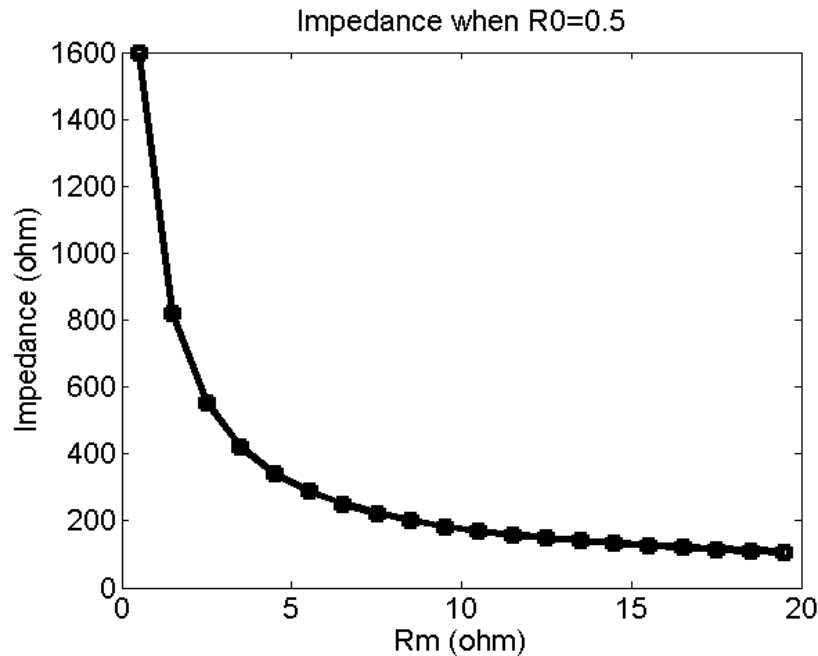


Fig. 3. 16 Parallel resonance impedance of FBAR when R_0 is kept at 0.5 ohm

Nevertheless, although the two proposed FBAR-DCO was fabricated in TSMC 0.18 μm CMOS technology and used monolithic FBAR-CMOS integration method in the fabrication, both of them cannot start oscillation. The most probable reason is the measured R_m of the FBAR is too large. For the Pierce FBAR-DCO, the R_m is as high as 500 ohm. For the inverter based FBAR-DCO, the R_m is 17 ohm. Both of the two R_m are far greater than the desired 0.5 ohm. Fig. 3.16 shows that when R_0 is kept at 0.5 ohm, the parallel resonance impedance is reduced shapely with the increasing of R_m . Thus, in order to make these two FBAR-DCOs oscillate successfully, the reduction of R_m in fabrication is necessary.

Chapter IV

Cross-coupled and Multiband FBAR-VCO

4.1. Introduction

FBAR-VCOs are not only able to be used to in transceivers to replace LC-VCO. In the fields of frequency reference and high precision sensors which use frequency as the output variable, low phase noise miniature oscillator is greatly demanded [37-39]. Traditionally, quartz crystal oscillators are widely used because of the excellent phase noise performance [37, 38]. However, large physical size, incompatibility with CMOS technology and low frequency output has severely limited the applications of quartz crystal oscillators in GHz-range and in highly miniaturized sensors in the future.

In response to the growing demand for GHz-range frequency and miniaturization, FBAR resonators which have Q-factor around 1000 or even more, have been used to design low phase noise GHz-range oscillators [37-39] for frequency reference and highly reliable sensors to replace quartz crystal oscillators in recent years. Nevertheless, simple single-ended architecture is employed and the phase noise of these FBAR oscillators needs further optimization.

In this chapter, a 1.9 GHz cross-coupled FBAR-VCO and a 0.65 GHz, 0.98 GHz, 1.96GHz and 3.92 GHz multiband FBAR-VCO are presented. The low frequency instability problem is analyzed and the solution methods are proposed. An excellent phase noise and high loop gain are obtained by considering the effect of transistors' size on the Q-factor and impedance of FBAR and Oscillation frequencies are extended by a divider and a multiplier.

4.2. 1.9 GHz cross-coupled FBAR-VCO

4.2.1 Circuit Design

In this design, the parameters and the impedance response of the adopted FBAR are shown in Fig. 4.1. The parallel resonance frequency f_p is 1.96 GHz and the series resonance frequency is f_s 1.92 GHz. The parameter values is also obtained from (2.3)-(2.6). The Q_p and the Q_s of the FBAR, calculated by (2.7), are about 1200 and 800, respectively.

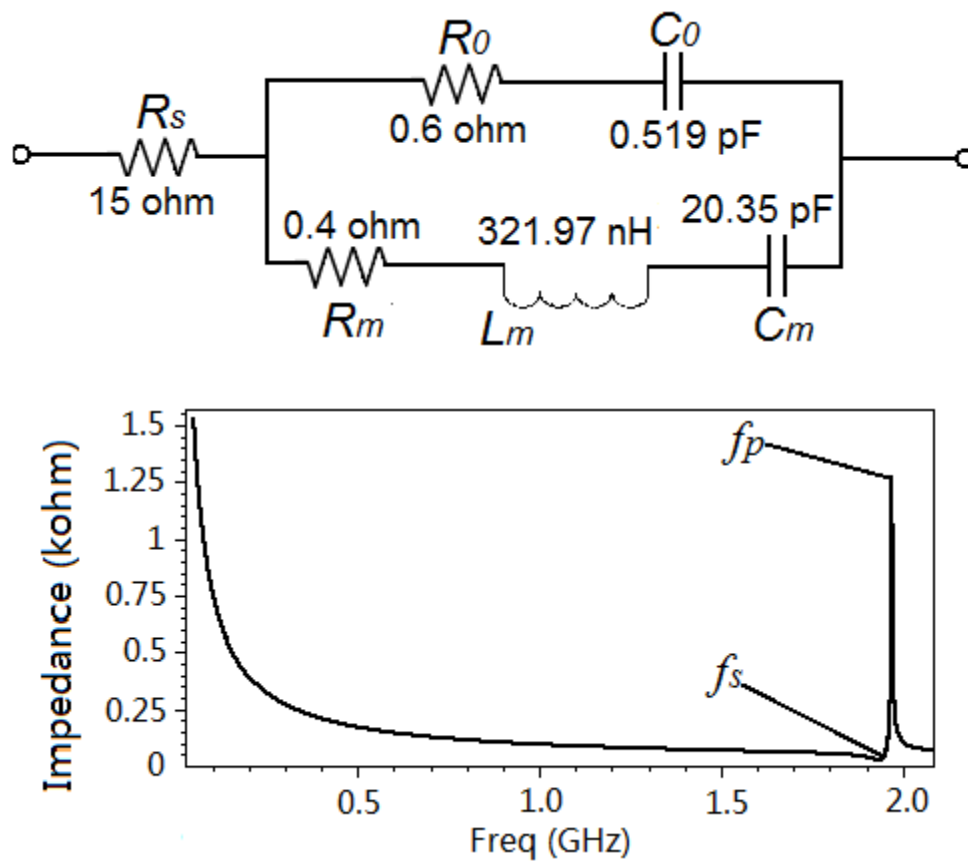


Fig. 4. 1 Parameters and impedance response of the adopted FBAR

Because cross-coupled FBAR-VCO suffers from low frequency instability problem, simple single ended architecture is employed in most of the published FBAR-VCO [36-38]. In [25], although a cross-coupled FBAR-VCO is proposed, the phase noise

performance is not good and the reason and solution of low frequency instability is not explained in theory. In our design of FBAR-VCO, both NMOS (M_1, M_2) and PMOS (M_3, M_4) transistors are used to constitute two cross-coupled pairs to reuse current and provide larger negative resistance. Instead of obtaining gate bias voltage from the drains of cross-coupled transistors, two voltages V_1 and V_2 are added to the gates, which keep the

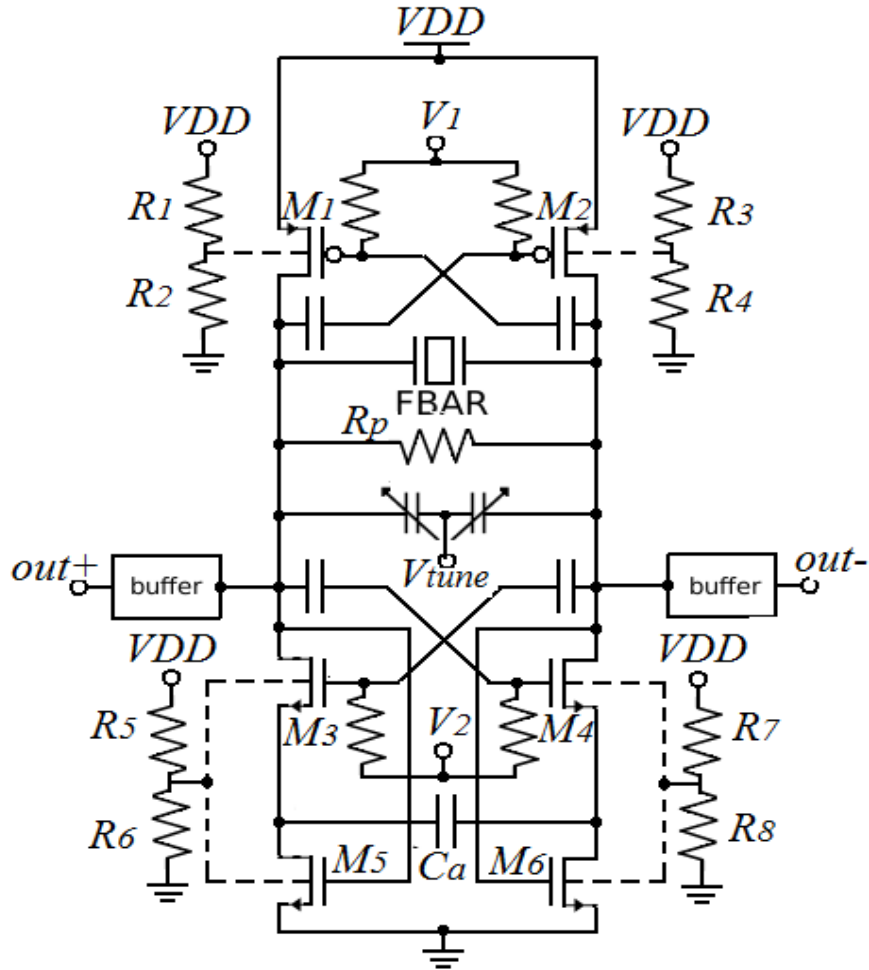


Fig. 4. 2 Circuit of the proposed FBAR-VCO

transistors working in saturation region. A tail feedback current source, composed of M_5 and M_6 , is used to control the common-mode drain voltage of the cross-coupled pairs and reduce $1/f$ noise furthermore. V_{tune} is used to control the oscillation frequency of the VCO.

Large resistors R_7 - R_8 are used as bias resistors to provide FBB bias voltage to all transistors. Capacitor C_a creates a high frequency path to eliminate the low frequency instability, which will be presented in detail in section 4.2.2. The sizes of all transistors are well optimized, which prevents large Q-degeneration of FBAR caused by parasitic capacitance and on-resistance to get a low phase noise and a high loop gain. The optimized method will be described in section 4.2.3.

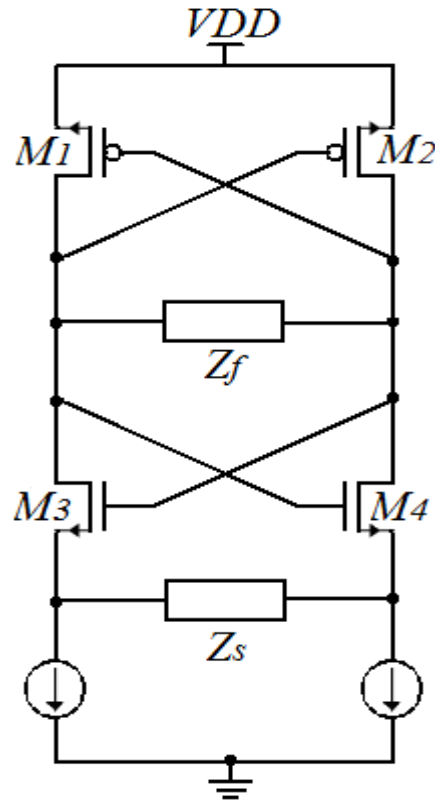


Fig. 4. 3 Equivalent circuit of the proposed FBAR-VCO

4.2.2. Low Frequency Instability Analyses and Elimination

In the design of a cross-coupled FBAR-VCO, because FBAR resonators are very similar to LC resonators at the parallel resonance frequency, the cross-coupled architecture of LC-VCO can also be employed. But the major challenge is to solve the instability in low

frequency which causes parasitic oscillation. In this subsection, not only the reason of instability is analyzed in theory, but also the solution methods are proposed. The first method employs a capacitor and while the other one employs a series inductor-capacitor.

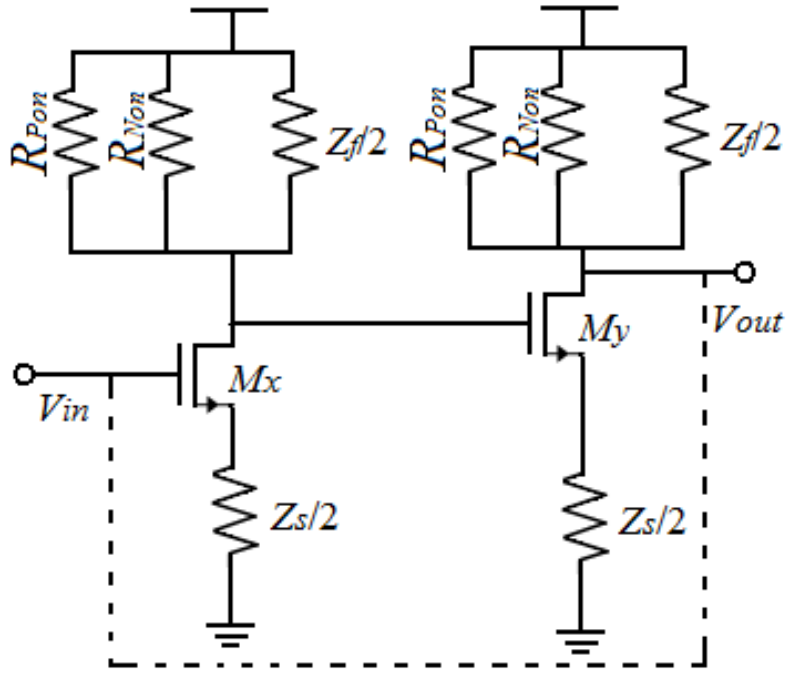


Fig. 4. 4 Redrawn equivalent circuit of the proposed FBAR-VCO

To describe the instability problem, the equivalent circuit of this FBAR-VCO is shown as Fig. 4.3, where Z_f is the impedance of FBAR, and Z_s is the impedance between two sources of cross-coupled pair. Because both two cross-coupled pairs are used to generate negative resistance, in order to calculate the loop gain, this equivalent circuit can be redrawn in Fig.4.4, where R_{Pon} and R_{Non} are the on-resistance of PMOS transistors and NMOS transistors respectively; the trans-conductance of M_x and M_y (g_m) is the sum of the trans-conductance of PMOS transistors g_{pm} and NMOS transistors g_{nm} . In order to calculate loop gain, the cross-coupled pair is cut from the gate of M_x and the input and output are named as V_{in} and V_{out} , respectively. Thus the small signal equivalent circuit of Fig 4.4 can

be drawn in Fig. 4.5, where V_{gsx} and V_{gsy} are the voltages between the gate and source of M_x and M_y respectively.

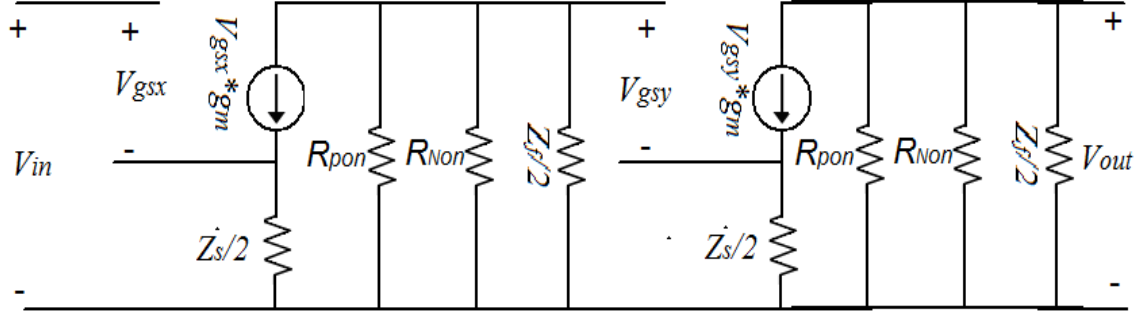


Fig. 4. 5 Small signal equivalent circuit of the circuit in Fig. 4.4

Based on the small signal equivalent circuit, the equations of V_{out} , V_{in} and V_{gsy} can be written as (4.1), (4.2) and (4.3) respectively.

$$V_{out} = V_{gsy} g_m (R_{Non} \parallel R_{Pon} \parallel \frac{Z_f}{2}) \quad (4.1)$$

$$V_{in} = V_{gsx} + V_{gsx} g_m \frac{Z_s}{2} \quad (4.2)$$

$$V_{gsy} = V_{gsx} g_m (R_{Non} \parallel R_{Pon} \parallel \frac{Z_f}{2}) - V_{gsy} g_m \frac{Z_s}{2} \quad (4.3)$$

Then rearranging (4.3), the relationship between V_{gsx} and V_{gsy} can be gotten as (4.4).

$$\frac{V_{gsy}}{V_{gsx}} = \frac{g_m (R_{Non} \parallel R_{Pon} \parallel \frac{Z_f}{2})}{1 + g_m \frac{Z_s}{2}} \quad (4.4)$$

Using (4.1), (4.2) and (4.4), the loop gain can be calculated as (4.5), based on the definition of loop gain.

$$Gain = \frac{V_{out}}{V_{in}} = \left(\frac{g_m (R_{Non} // R_{Pon} // \frac{Z_f}{2})}{1 + g_m \frac{Z_s}{2}} \right)^2 \quad (4.5)$$

From (4.5), it is clear that high loop gain occurs not only at the frequency f_p , but also occurs in low frequency as FBAR also has high impedance in low frequency as shown in Fig. 4.1, and Z_s is always small in normal condition. For this reason, low frequency instability and parasitic oscillation will happen if loop gain exceeds 0 dB satisfying Barkhausen's criterion which is illustrated in Fig. 4.6.

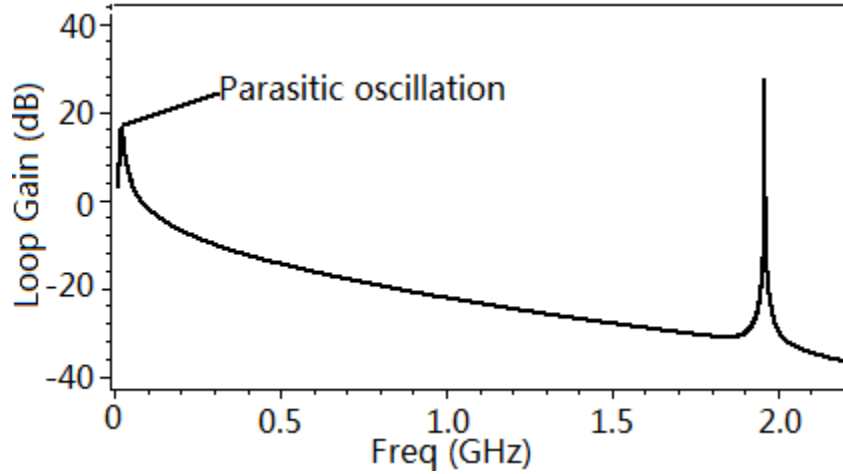


Fig. 4. 6 Parasitic oscillation of a cross-coupled FBAR-VCO

To prevent parasitic oscillation, the high loop gain in low frequency should be reduced by increasing Z_s in low frequency. The two methods to enhance Z_s are shown in Fig. 4.7. For the first one, the capacitor C_a is added between the sources of M_3 , M_4 . This capacitor which creates a high frequency path reduces the loop gain in low frequency. If the value of C_a is not large enough, it will cause an undesirable reduction of the loop gain at the frequency f_p . If the value of C_a is too large, parasitic oscillation will not be eliminated.

Thus, in this letter, C_a is set to 2 pF for the trade-off between low frequency stability and loop gain.

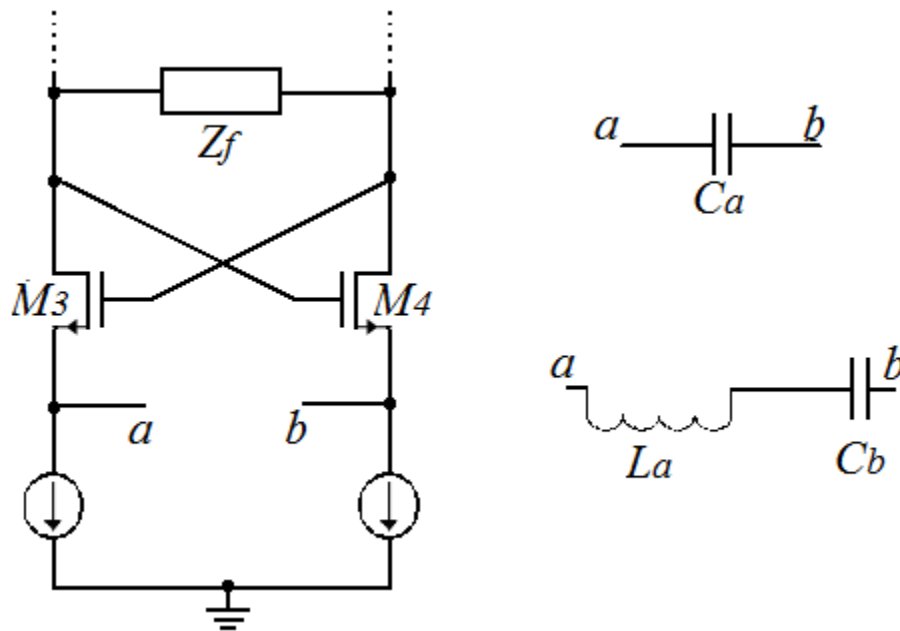


Fig. 4. 7 Two methods for enhancing Z_s in low frequency

In the second one, a series inductor-capacitor (series- $L_a C_b$) which has resonance frequency at f_p is used. In this letter, to get low series resonance impedance, the L_a and the C_b are set to 6 nH and 1.1 pF respectively. It provides lower impedance around f_p and higher impedance in low frequency as shown in Fig. 4.8. In Fig. 4.9 (a), it can be seen that in low frequency, the loop gain for series- $L_a C_b$ is lower by 0.6 dB compared to that for C_a only; and in (b), the loop gain for series- $L_a C_b$ is increased by 12 dB compared to that for C_a only in high frequency.

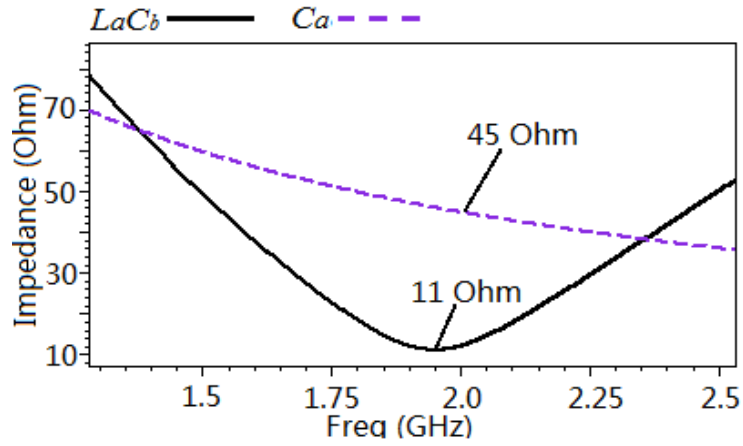
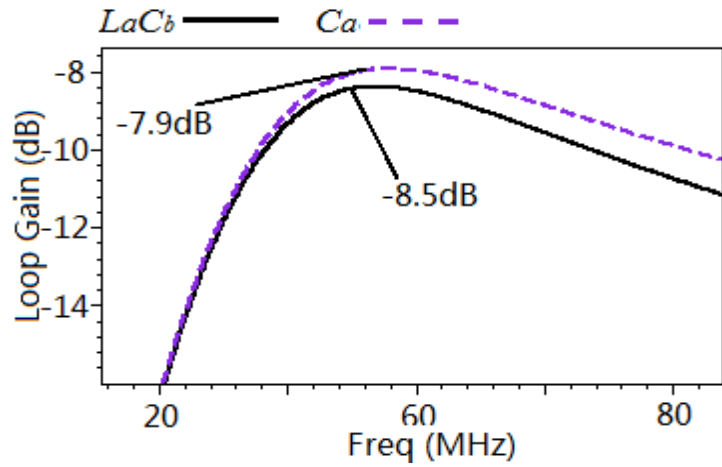
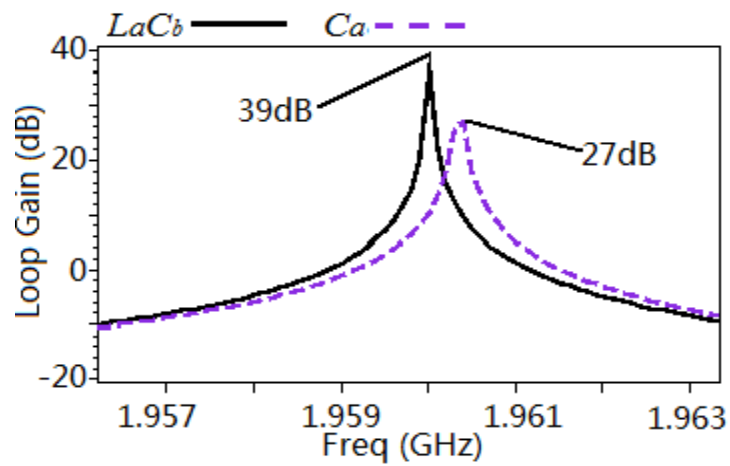


Fig. 4. 8 Impedance comparison of C_a and series- $LaCb$



(a)



(b)

Fig. 4. 9 Loop gain comparison by using the two methods for enhancing Z_s

The two methods of enhancing Z_s can solve the parasitic oscillation in low frequency. In addition, other methods are also employed to further improve the gain margin in low frequency.

The first method is to reduce Z_f in low frequency. In the proposed VCO, the resistor R_p is connected to FBAR in parallel to decrease the infinite impedance of FBAR in low frequency. Since the parallel resistor also leads to the impedance reduction of FBAR at parallel frequency, 10K ohm resistor is selected to avoid the deterioration of Q-factor.

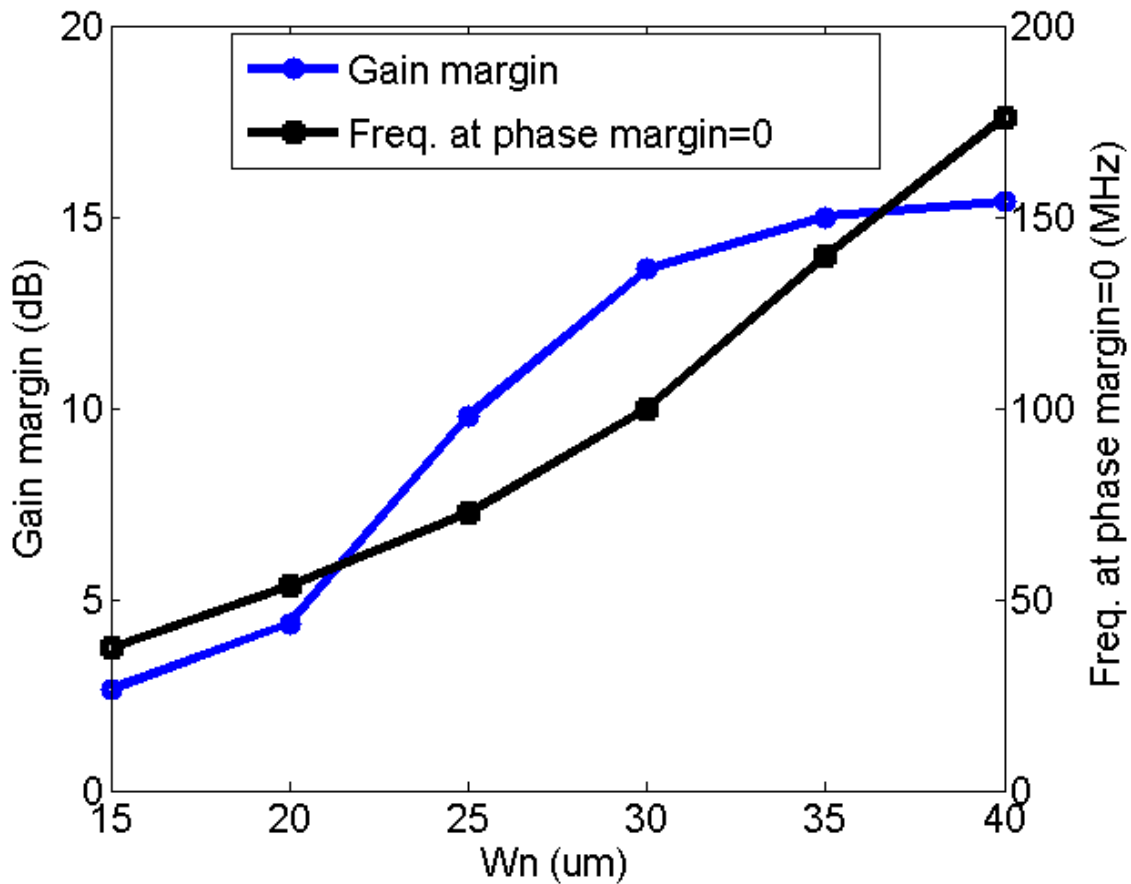


Fig. 4. 10 Low frequency gain margin with the size changing of the NMOS transistors M_3 and M_4 (W_n)

For the second one, the effect of the size of NMOS transistors on the gain margin in low frequency is considered. Fig. 4.10 shows that the gain margin in low frequency

decreases with the decrease in the size of NMOS transistors M_3 and M_4 (W_n). The reason is that the impedance of FBAR has a great growth with frequency decrease and the frequency in which phase margin is equal to zero, is decreasing with the decrease of W_n . In this letter, W_n is set to 30 μm .

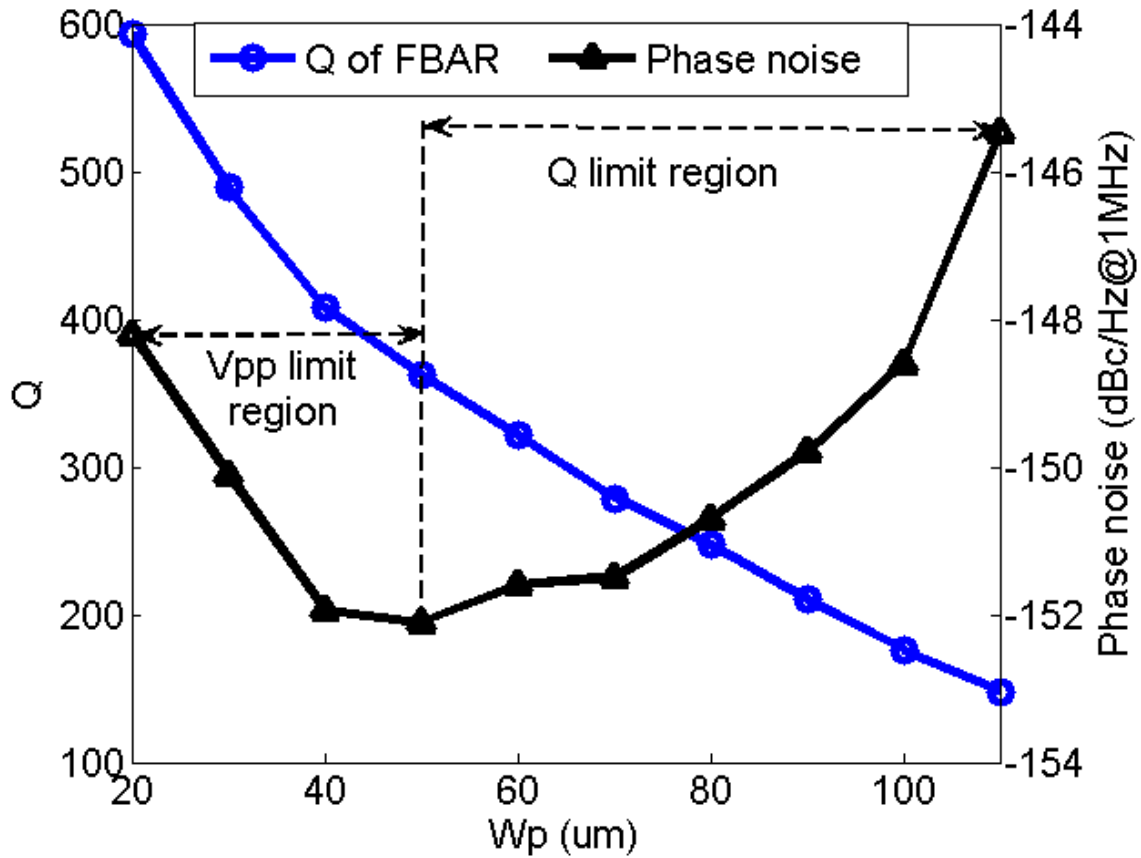
4.2.3. Optimization of Phase Noise and Loop Gain

In Leeson phase noise model, the relationship between Q and phase noise is given by:

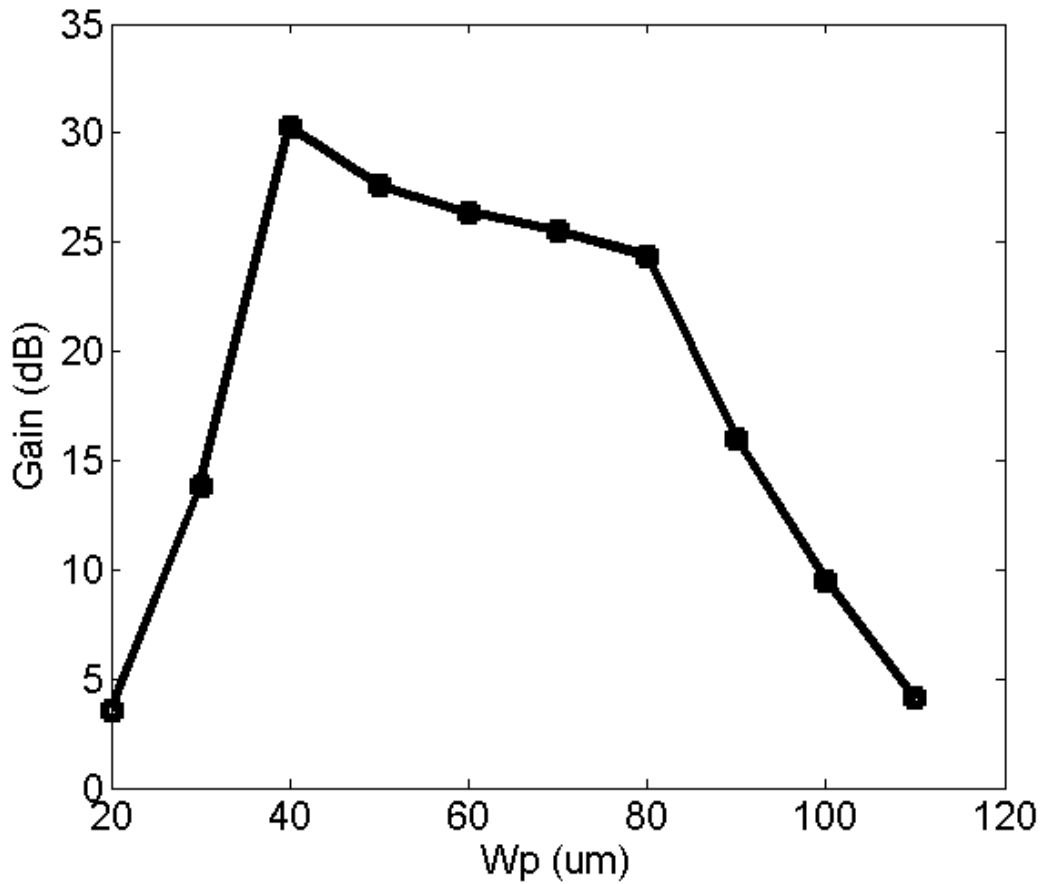
$$L(f_m) \propto \frac{kT}{P_{out}} \cdot \frac{1}{2Q^2} \cdot \frac{f_0^2}{f_m^2} \quad (4.6)$$

where k and T are constants; $L(f_m)$ is the phase noise at the offset frequency f_m from the oscillation frequency f_0 and P_{out} is the output power. It is known that phase noise improves as both the carrier power and Q-factor increase. Because the Q-factor of FBAR will be deteriorated by the on-resistance reduction of transistors, large size transistors should be avoided. Both the size reduction of PMOS transistors and that of NMOS transistors can raise the on-resistance, but based on the analysis in subsection 4.2.2, the size reduction of NMOS transistors will decrease the gain margin in low frequency. Therefore, only the size of PMOS transistors is adjusted to optimize the phase noise. In Fig. 4.11 (a), it is shown that when the size of PMOS transistor M_1 and M_2 (W_p) is decreasing from 110 μm to 50 μm , the Q-factor of FBAR is increasing and the phase noise is improving. Thus, this region is called Q limit region in this paper. When W_p is below 50 μm , although the Q-factor is still increasing, the phase noise is not improving because of the reduction of the oscillation amplitude, which is called peak to peak voltage (V_{pp}) limit region. For the loop gain, it can

be known from (4.5) that since the loop gain also increases with the increase in on-resistance of transistors, the optimal size which can get the best phase noise, can also obtain high loop gain, as shown in Fig. 4.11 (b).



(a)



(b)

Fig. 4. 11 Relationship among the size of PMOS transistor M_1 and M_2 (W_p), Q-factor, phase noise (a) and loop gain (b)

4.2.4. Simulation Result

Using the proposed solutions of low frequency instability, the proposed 1.9 GHz FBAR-VCO is designed in 0.18 μm CMOS successfully. Fig. 4.12 is the layout and Fig. 4.13 is the differential output waveform. The simulation phase noise is shown in Fig. 4.14. It is shown that enhancing Z_s by using series- $L_a C_b$ can achieve better phase noise, because series- $L_a C_b$ has lower loss at f_p . The phase noise is improved from -151.5 dBc/Hz to -153.5 dBc/Hz at 1 MHz offset frequency. The FOM is also improved from -215 dB to -217 dB.

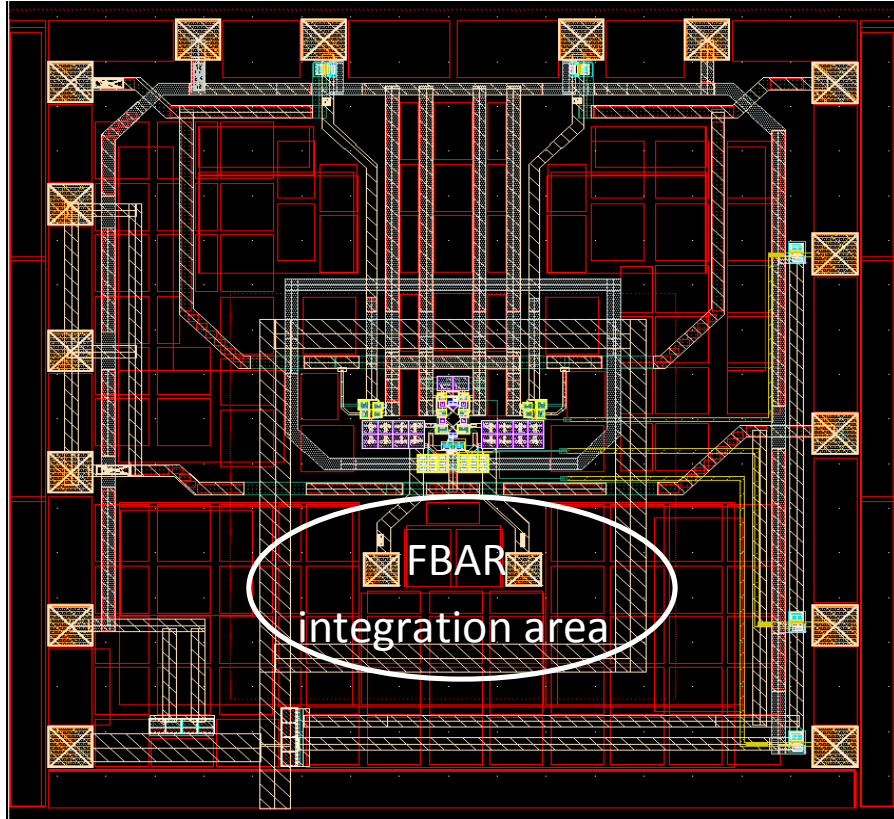


Fig. 4. 12 Layout of the proposed cross-coupled FBAR-VCO

Although enhancing Z_s by using series- $L_a C_b$ can get a better performance, it takes larger chip size because of a 6nH inductor. And it can be known from Fig.4.9 that enhancing Z_s by only using C_a , the 7.9dB gain margin is enough to suppress the parasitic oscillation and the -151.5dBc/Hz phase noise is also enough for most application. Therefore, to save the cost of fabrication, only C_a is adopted in the final design. The tuning range is narrow because the FBAR shows inductance characteristic only between f_s and f_p , and the frequency difference of f_s and f_p is very small.

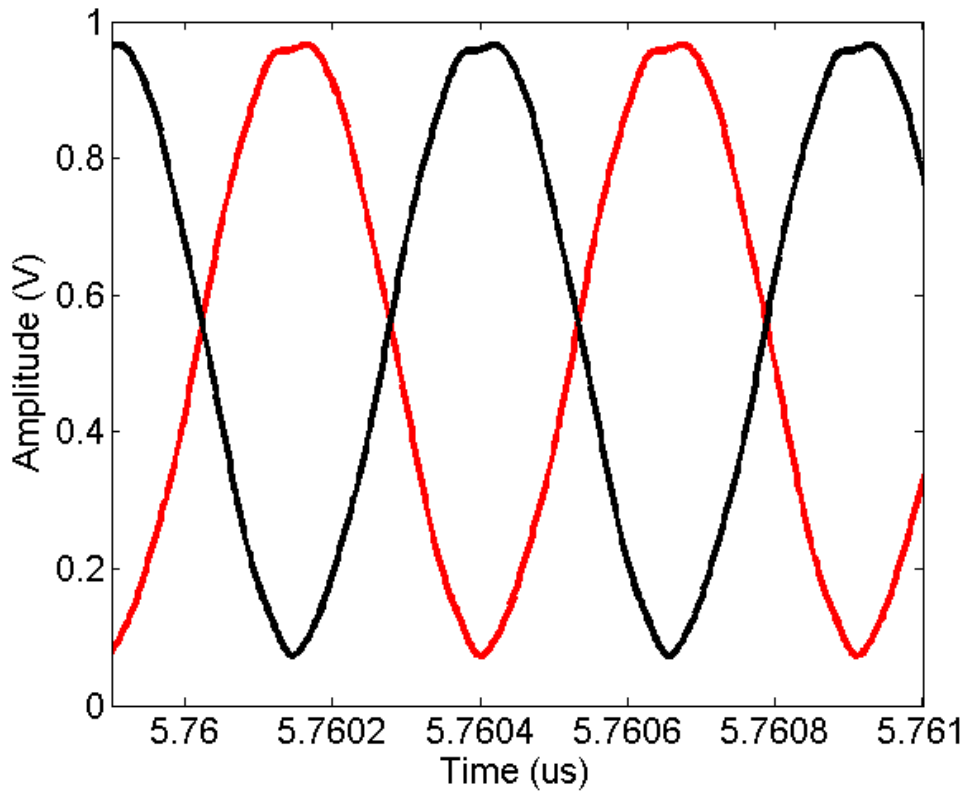


Fig. 4. 13 Output waveform of the proposed FBAR-VCO

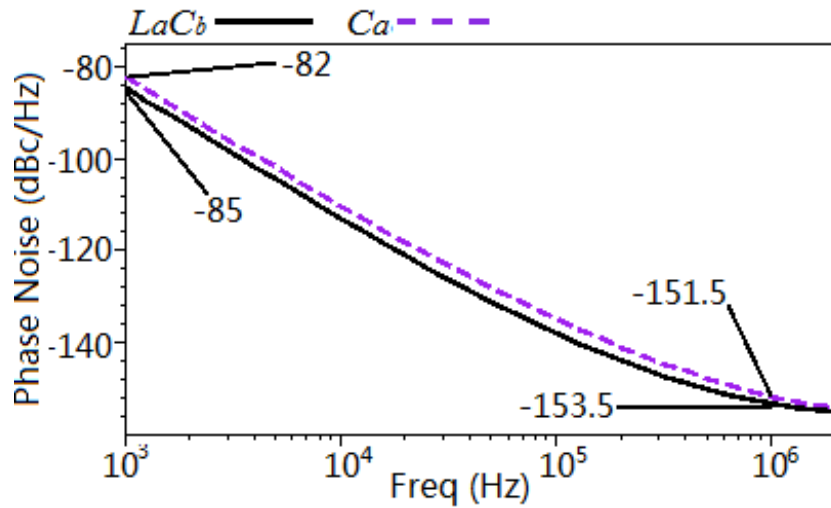


Fig. 4. 14 Phase noise comparison of FBAR-VCO by using the two methods for enhancing Z_s

Table 4.1 shows the comparison between this work and other published works. Compared to other published FBAR-VCOs, the proposed FBAR-VCO has better phase noise and FOM.

Table 4.1 Comparison with other published oscillators

	This work with C_a (Post-layout)	This work with $L_a C_b$ (Post-layout)	[24]	[25]	[26]
Process	0.18 μ m CMOS	0.18 μ m CMOS	0.25 μ m BiCMOS	0.13 μ m CMOS	0.18 μ m CMOS
Vdd (V)	1.1	1.1	2.4	1.0	1.8
f_0 (MHz)	1962	1962	2100	1575	1500
Power (mW)	1.7	1.7	58	0.5	3.78
Tuning range (MHz)	2	2	37	1.35	1
$L(\Delta f)$ @ 1MHz (dBc/Hz)	-151.5	-153.5	-144	-138	-142
FOM	-215	-217	-193	-204	-200

4.3. Multiband FBAR-VCO

4.3.1. Circuit Design

In this design, we employed the cross-coupled FBAR-VCO as a VCO core and to extend output frequencies, an extended true single phase clock logic (E-TSPC) based divide-by-2 or 3 divider is used to generate 0.65 GHz and 0.98 GHz output, and a current mode logic (CML) based multiply-by-2 multiplier is employed to generate 3.92 GHz frequency. The architecture of the proposed multiband FBAR-VCO is shown in Fig. 4.15.

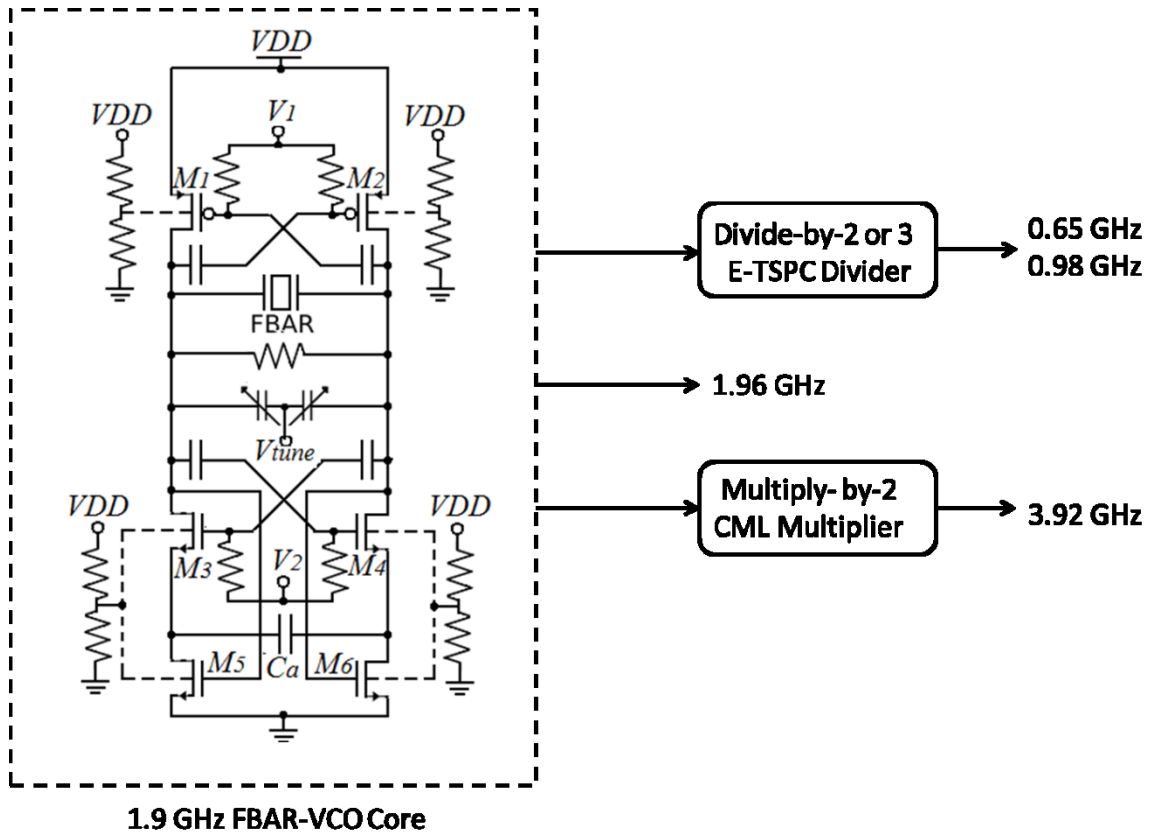


Fig. 4. 15 Proposed multiband FBAR-VCO

In order to extend oscillation frequencies below 1 GHz without using CMOS switch, a high-speed frequency divide-by-2 or 3 divider is adopted in this work. Conventionally, current mode logic (CML), injection-locked logic and extended true single phase clock logic (E-TSPC) are the main solutions of high-speed frequency dividers. However, because all transistors of CML must be biased in saturation region, CML logic costs more current compared to E-TSPC logic in 1.9 GHz band. For injection-locked logic, on-chip inductors lead to large chip area and it is not easy to cover the divider ratio of both 1/2 and 1/3.

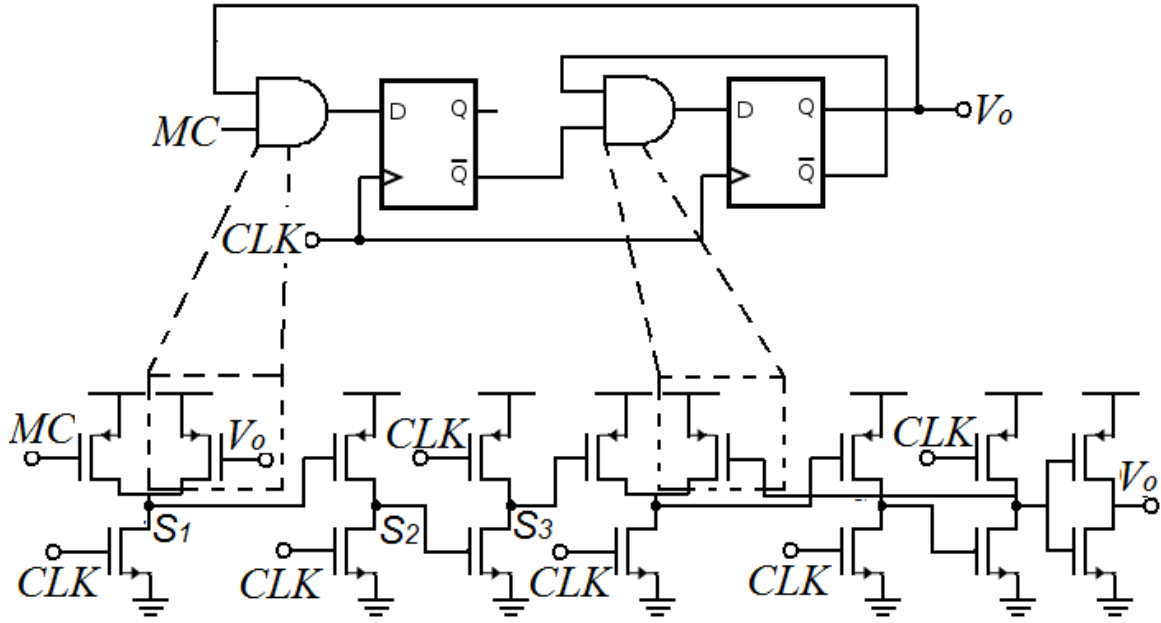


Fig. 4. 16 Schematic of divide-by-2 or 3 divider

Based on the analyses above, the E-TSPC logic is utilized in this design, as shown in Fig. 4.16. CLK is the input port and V_0 is the output port. The divider is composed of two E-TSPC D-flip flops in which two AND gates are embedded. The divider ratio is simply controlled by the potential of MC . When MC is low, node S_1 is set to logically high, and both S_2 and S_3 are disabled. Thus only one D-flip flop is activated and the divider is operated as divide-by-2. Conversely, when MC is high, the divider operates in the mode of divide-by-3.

In order to generate higher frequency, a frequency multiply-by-2 multiplier is included in our work. Traditionally, frequency multipliers are realized by the nonlinearity of CMOS transistors. However, harmonics suppression and large power consumption are their challenges.

In our work, a CML logic based high-speed frequency multiplier is employed, as shown in Fig. 4.17. If two signals with same frequency but out of phase by 90 degree are

input to an XOR gate, the frequency of output signal will be two times the input signal frequency. In this work, the differential output signals of VCO are input to a passive RC phase shift network to generate quadrature signals. And the quadrature signals are used to drive the CML logic based high-speed XOR gate. Because this multiplier is not realized by the nonlinearity of CMOS transistors, the harmonics suppression problem doesn't occur and the power consumption is also decreased.

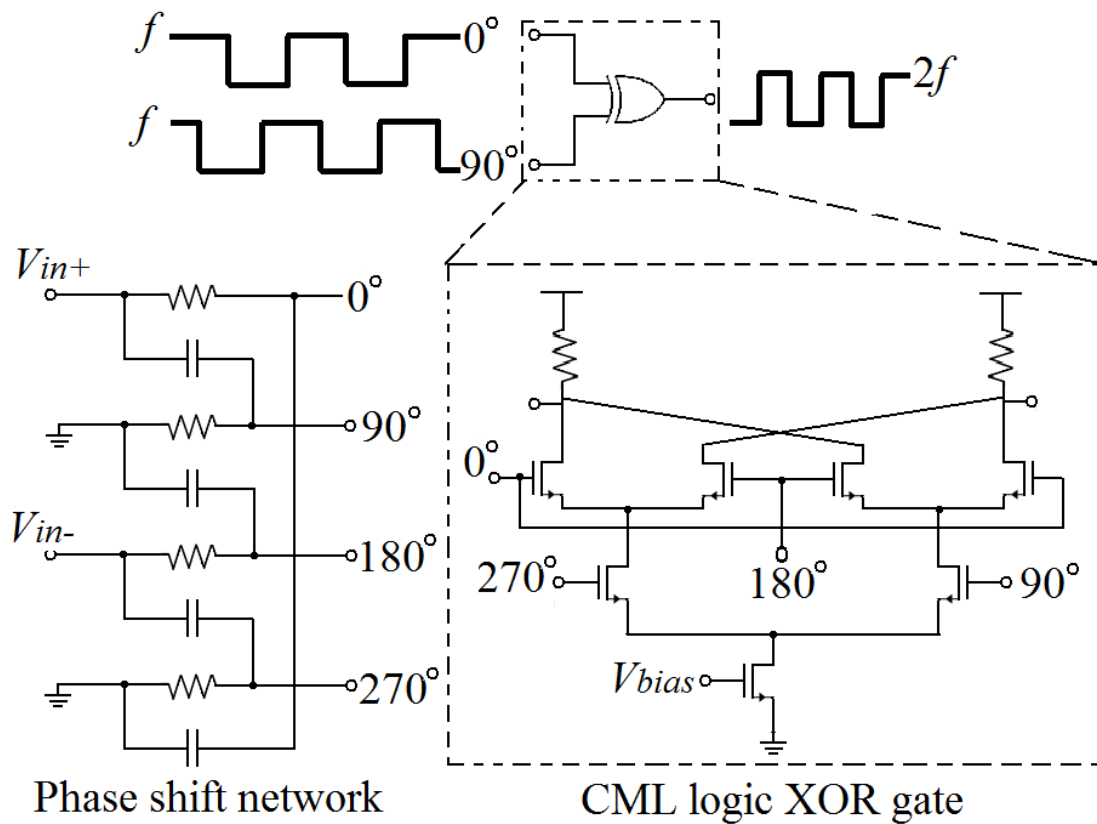


Fig. 4. 17 Schematic of multiply-by-2 multiplier

4.3.2. Simulation Result

The proposed multiband FBAR-VCO designed in 0.18 μm CMOS operates at 0.65 GHz, 0.98 GHz, 1.96 GHz and 3.92 GHz successfully. The layout is shown in Fig. 4.18 and the output waveform is shown in Fig. 4.19. Fig. 4.20 shows the post-layout simulation phase noise is. Table 4.2 is the comparison between this work and other published works. It is shown that below 1.96 GHz, the proposed multiband FBAR-VCO has very low phase noise below -150 dBc/Hz at 1 MHz offset and even in 3.9 GHz, the phase noise is still below -140 dBc/Hz. All the FOMs of four bands are below -200 dB and the minimum FOM is as low as -215 dB, much better than other published works.

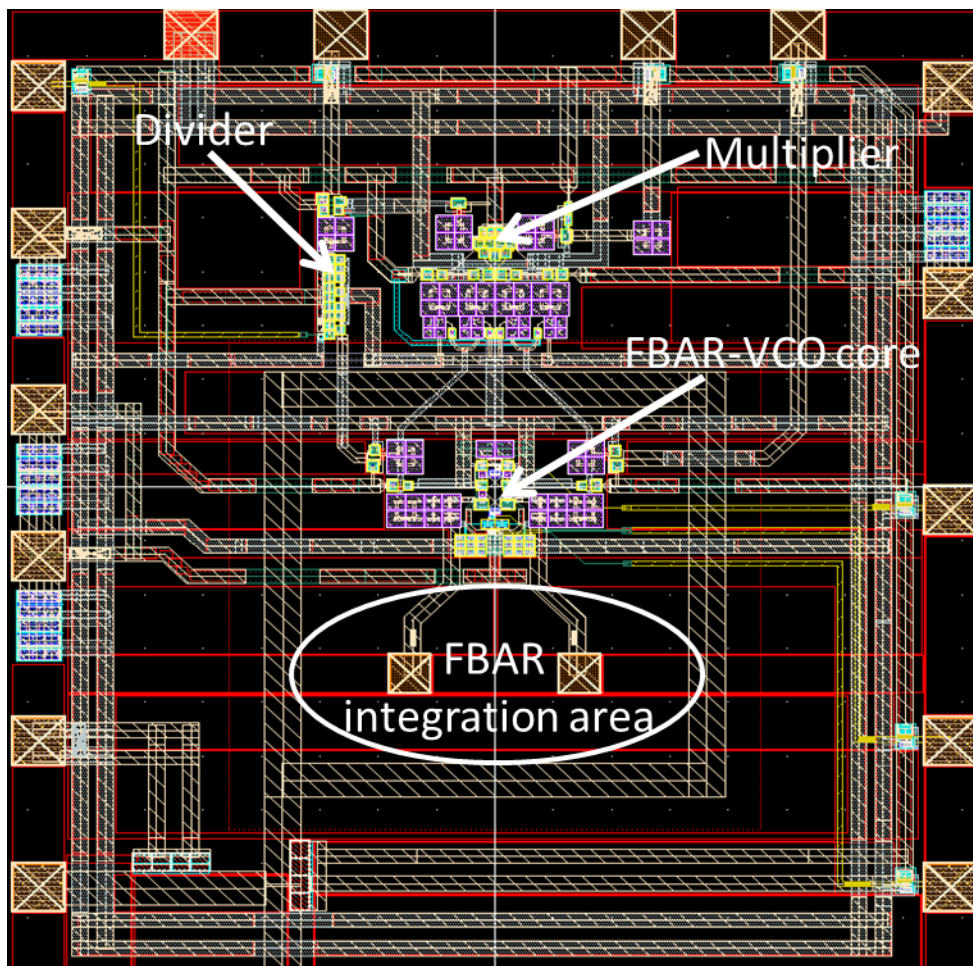


Fig. 4. 18 Layout of the proposed multiband FBAR-VCO

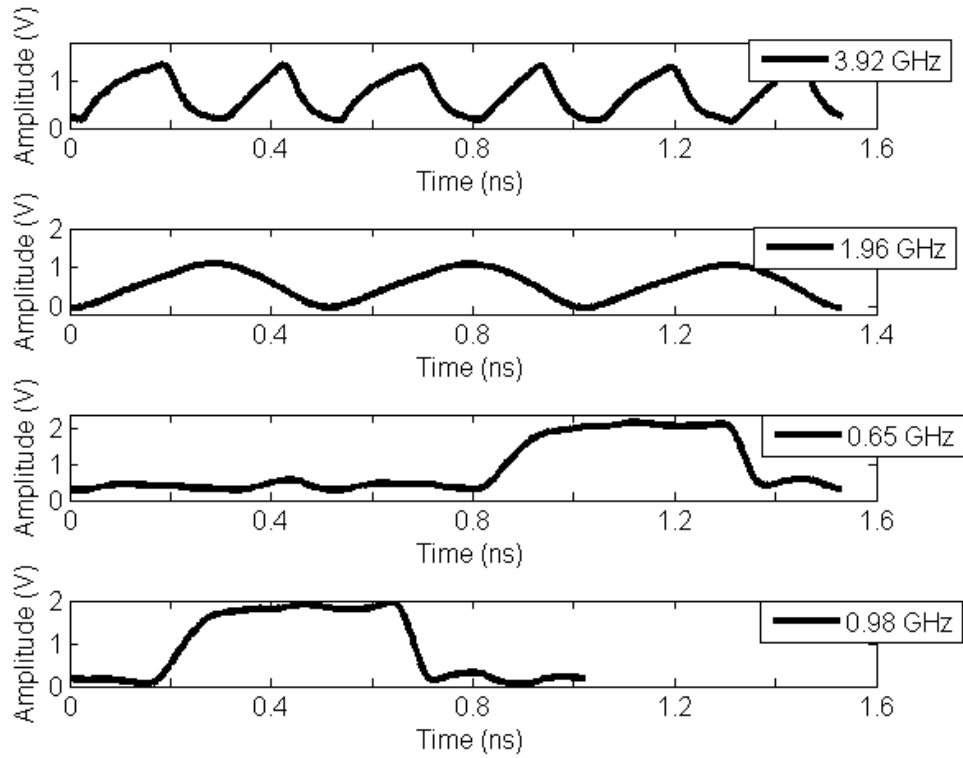


Fig. 4. 19 Output waveform of the proposed multiband FBAR-VCO

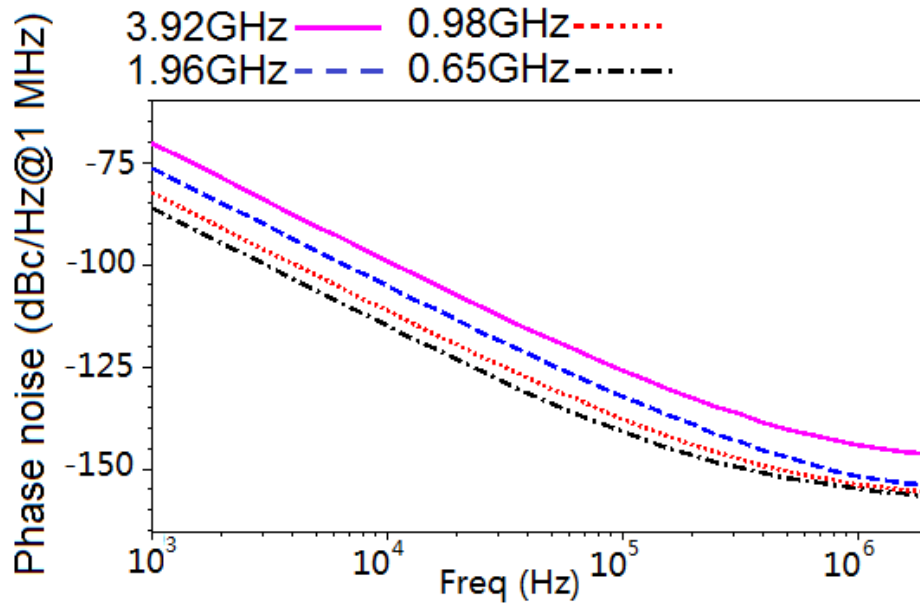


Fig. 4. 20 Phase noise of the proposed multiband FBAR-VCO

Table 4.2. Comparison with other published oscillators

	Proposed multiband FBAR-VCO (Post-layout)				[25]	[26]
Process	0.18 μm CMOS				0.13 μm CMOS	0.18 μm CMOS
Vdd (V)	1.1				1.0	0.8
f_0 (MHz)	650	980	1960	3920	1575	1500
Power (mW)	3.97	4	1.7	4.3	0.5	3.78
Tuning range (MHz)	0.67	1	2	4	1.35	1
$L^{(Af)}$ @ 1MHz (dBc/Hz)	-154.6	-153.5	-151.5	-143.2	-138	-142
FOM	-205	-207	-215	-209	-204	-200

4.4. Conclusion

In this Chapter, a 1.9 GHz cross-coupled FBAR-VCO and a multiband FBAR-VCO operating at 0.65 GHz, 0.98 GHz, 1.96 GHz and 3.92 GHz for frequency reference or highly miniature sensors are presented. The reason and solutions of low frequency instability in cross-coupled FBAR-VCO is discussed and by novel optimization method, an excellent phase noise and FOM value is obtained.

Chapter V

FBAR-VCO based PLL

5.1. Introduction

In this Chapter, instead of LC-VCOs in the traditional PLL, the presented cross-coupled FBAR-VCO is employed to design an FBAR-VCO based PLL. It is composed of phase frequency detector (PFD), charge pump (CP), low pass filter (LPF), FBAR-VCO and divider, as shown in Fig. 5.1. The novel charge pump design based on complementary logic switches is adopted to reduce the mismatch current and the current noise. The proposed PLL proves the possibility of FBAR-VCO based PLL and the simulation result shows the phase noise of FBAR-VCO is further improved.

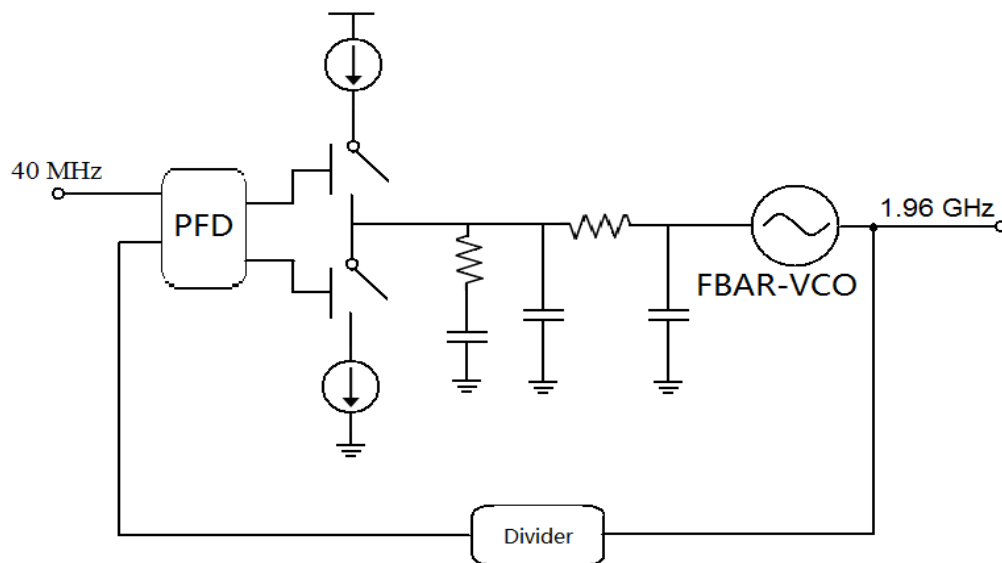


Fig. 5. 1 Structure of FBAR-VCO base PLL

The flow of design is shown as follow:

1. Set basic parameter such as reference frequency, tuning range of VCO, divide ratio, current of CP, loop-bandwidth and phase margin;

2. Design LPF and analyze stability;
3. Make behavior model and simulate locking process by Verilog-A;
4. Circuit design of each part;
5. Extract noise of each part by Spectre-RF and simulate the total phase noise of PLL;
6. Layout and Post-layout simulation.

5.2. Design of FBAR-VCO based PLL

5.2.1. Stability Analysis and LPF Design

Since PLL is a close loop feedback system, it is important to keep the stability of PLL. Fig. 5.2 shows the linear phase model of PLL [40].

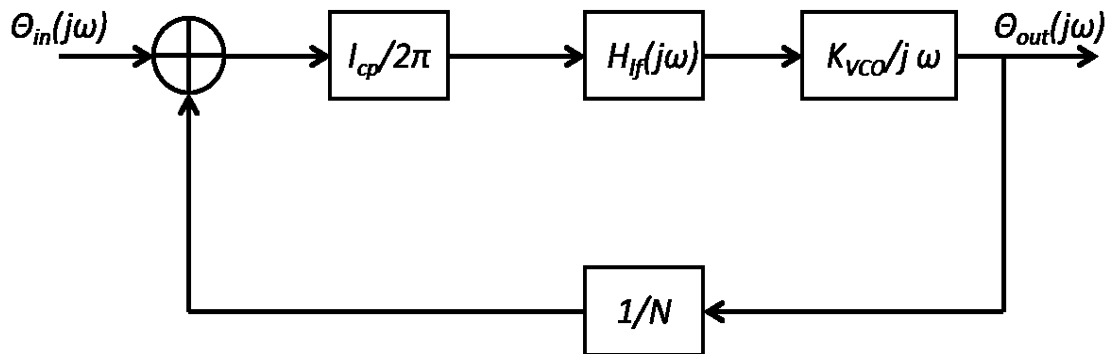


Fig. 5. 2 Linear phase model of PLL

where, I_{cp} is the current of CP (A/rad); K_{vco} is the gain of VCO ($rad/s/V$); N is the divide ratio of divider; and $H_{lf}(j\omega)$ is the transform function of LPF. In our design, a third-order passive LPF is adopted as shown in Fig. 5.3.

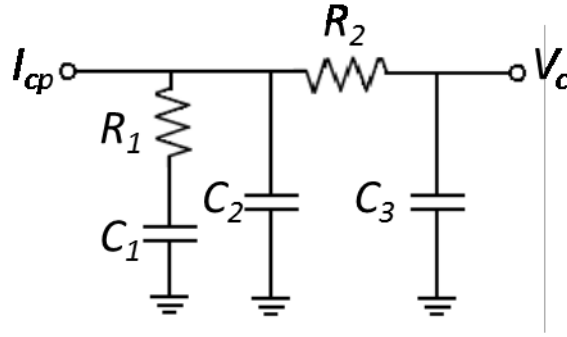


Fig. 5. 3 Third-order passive LPF

Thus, the transform function of LPF is

$$H_f(j\omega) = \frac{1}{j\omega} \cdot \frac{(1 + j\omega R_1 C_1)/(C_1 + C_2 + C_3)}{1 + j\omega \frac{R_1 C_1 (C_2 + C_3) + R_2 C_3 (C_1 + C_2)}{C_1 + C_2 + C_3} + (j\omega)^2 \frac{R_1 R_2 C_1 C_2 C_3}{C_1 + C_2 + C_3}} \quad (5.1)$$

As $C_1 \gg C_2, C_3$

$$\begin{aligned} H_f(j\omega) &\approx \frac{1}{j\omega (C_1 + C_2 + C_3)} \cdot \frac{(1 + j\omega R_1 C_1)}{1 + j\omega R_1 (C_2 + C_3) + (j\omega)^2 R_1 R_2 C_2 C_3} \\ &= \frac{1}{j\omega (C_1 + C_2 + C_3)} \cdot \frac{(1 + j\omega/\omega_z)}{(1 + j\omega/\omega_{p2})(1 + j\omega/\omega_{p3})} \end{aligned} \quad (5.2)$$

Where,

$$\omega_z = \frac{1}{R_1 C_1} \quad (5.3)$$

$$\omega_{p2} = \frac{1}{R_1 (C_2 + C_3)} \quad (5.4)$$

$$\omega_{p3} = \frac{1}{R_2 C_2 C_3 / (C_2 + C_3)} \quad (5.5)$$

In order to calculate the component value of the LPF, first we need to set some basic parameter as Table 5.1:

Table 5.1 Basic parameter of PLL

Locking time T_{lock}	400 μ S
Maximum frequency of VCO f_{max}	1961 MHz
Minimum frequency of VCO f_{min}	1959 MHz
Maximum control voltage of VCO V_{max}	1.4 V
Minimum control voltage of VCO V_{min}	0.4 V
Current of CP I_{cp}	100 μ A
Divide ratio N	40
Open loop phase margin ϕ_m	53°

Since the open loop gain of PLL is

$$H_{ol}(j\omega) = \frac{I_{cp} K_{vco} H_f(j\omega)}{2\pi N j\omega} \quad (5.6)$$

Where,

$$K_{vco} = \frac{2\pi(f_{max} - f_{min})}{V_{max} - V_{min}} \quad (5.7)$$

The bandwidth of PLL is solved from $|H_{ol}(j\omega)| = 1$:

$$\omega_c = K \frac{C_1}{C_1 + C_2 + C_3} \cdot \frac{\cos(\phi_{p2}) \cos(\phi_{p3})}{\sin(\phi_z)} \quad (5.8)$$

Where,

$$K = \frac{I_{cp} K_{vco} R_1}{2\pi N} \quad (5.9)$$

$$\phi_z = \tan^{-1}(\omega_c / \omega_z) \quad (5.10)$$

$$\phi_{p2} = \tan^{-1}(\omega_c / \omega_{p2}) \quad (5.11)$$

$$\phi_{p3} = \tan^{-1}(\omega_c / \omega_{p3}) \quad (5.12)$$

Thus, the open loop phase margin is

$$\begin{aligned} \phi_m &= \phi_z - \phi_{p2} - \phi_{p3} = \tan^{-1}(\omega_c / \omega_z) - \tan^{-1}(\omega_c / \omega_{p2}) - \tan^{-1}(\omega_c / \omega_{p3}) \\ &\approx \tan^{-1}(\omega_c / \omega_z) - \tan^{-1}(\omega_c / \omega_{p2}) \end{aligned} \quad (5.13)$$

To keep stability, when $|H_{ol}(j\omega)| = 1$, maximum phase margin should be obtain,

$$\omega_c = \sqrt{\omega_{p2}\omega_z} = \sqrt{d}\omega_z \quad (5.14)$$

Where,

$$d = \frac{C_1}{C_2 + C_3} \quad (5.15)$$

Then,

$$\phi_{m \max} = \tan^{-1}(\sqrt{\omega_{p2} / \omega_z}) - \tan^{-1}(\sqrt{\omega_z / \omega_{p2}}) = \tan^{-1} \frac{d-1}{2\sqrt{d}} \quad (5.16)$$

Since $\sin(\phi_z) = \cos(\phi_{p2}) \cos(\phi_{p3})$, (5.8) is simplified as

$$\omega_c = K \frac{C_1}{C_1 + C_2 + C_3} = K \frac{1+d}{d} \quad (5.17)$$

As ω_c is also equal to

$$\omega_c \approx 2\pi \frac{4}{T_{lock}} \quad (5.18)$$

From (5.14)-(5.18) and the basic parameter in Table 5.1, K , d , ω_z , ω_{p2} and ω_c is able to be calculated, and then from (5.3)-(5.5), (5.7) and (5.9), R_1 , R_2 , C_1 , C_2 , C_3 can be obtained. The calculated parameters are shown in Table 5.2.

Table 5.2 Parameters of LPF

R_1	17.427 K Ohm
R_2	15.186 K Ohm
C_1	2513.2 pF
C_2	231.89 pF
C_3	100 pF

After the parameters of LPF are calculated, the stability analyses should be done by Simulink. The bode graph of the proposed PLL is shown in Fig. 5.4.

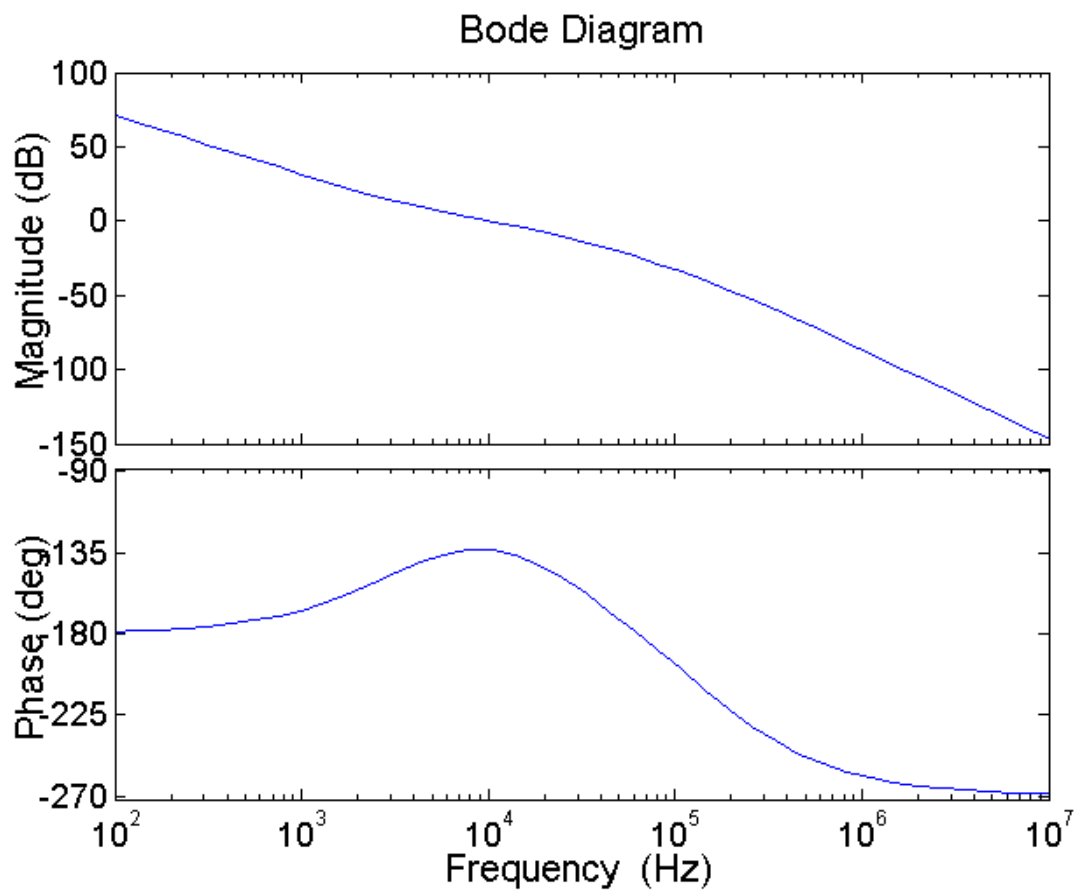


Fig. 5. 4 Bode graph of the proposed PLL

It is known in Fig. 5.4 that the bandwidth of PLL is about 10 KHz and the phase margin is about 45° , which can keep the stability of the proposed PLL. In addition, because of C_I cannot be integrated, an off-chip capacitor is used in our design.

After calculating the parameters of LPF, the behavior simulation result of locking process is shown in Fig. 5.5. It is know that the PLL is locked at about 400 μS .

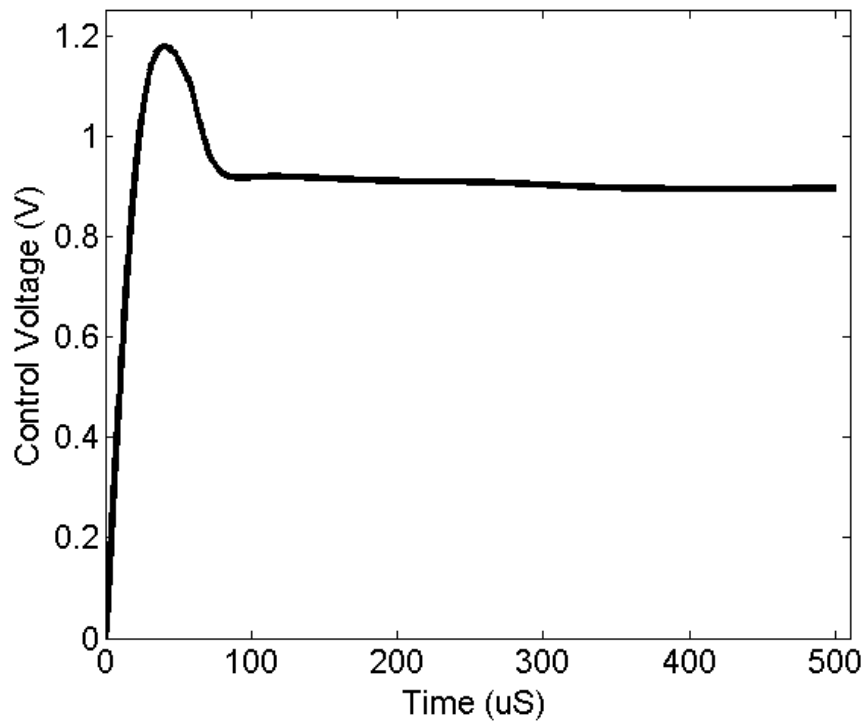


Fig. 5. 5 Locking process of PLL

5.2.2. Circuit Design

5.2.2.1. PFD and CP design

PFD detects the phase difference between the reference signal and the feedback signal from divider. A traditional tri-state PFD [31] is employed in our design, as shown in Fig 5.6. It is based on two D-flip flops and an AND gate, and both D-flip flop inputs are tied high. The reference and the output of the divider are each fed into a clock input of one of the D-flip flops.

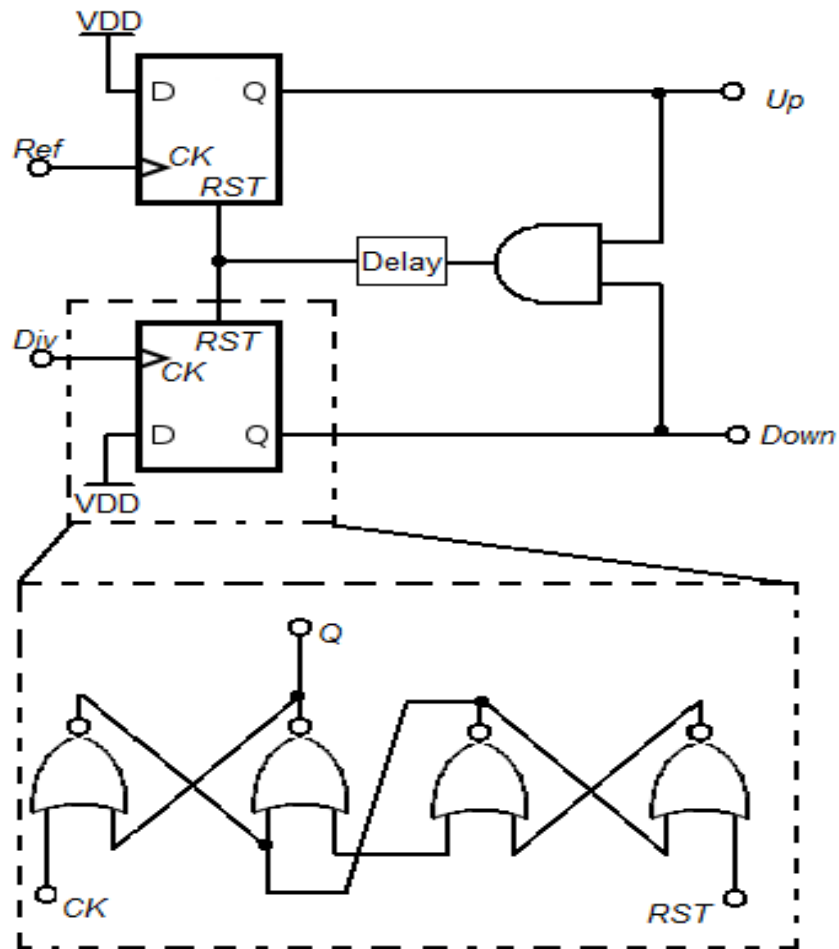


Fig. 5. 6 Traditional tri-state PFD

One of the most significant part of the PLL is the charge pump. The current mismatch of CP must be reduced as lower as possible to reduce the current noise. The schematic of proposed CP is shown in Fig 5.7. Transistors M_1 - M_{12} are used to constitute a cascode current source to improve the output impedance and reduce the current mismatch of node X and Y . Transistors M_{13} - M_{20} make up four complementary logic switches to restrain clock feed-through, and an operation amplitude is used to keep the voltage of node A and B in equal to reduce charge sharing. The current mismatch characteristic of CP (a) and the current noise of PFD and CP (b) are shown in Fig. 5.8. It is shown that the current mismatch is below 0.1% and the current noise is also very low.

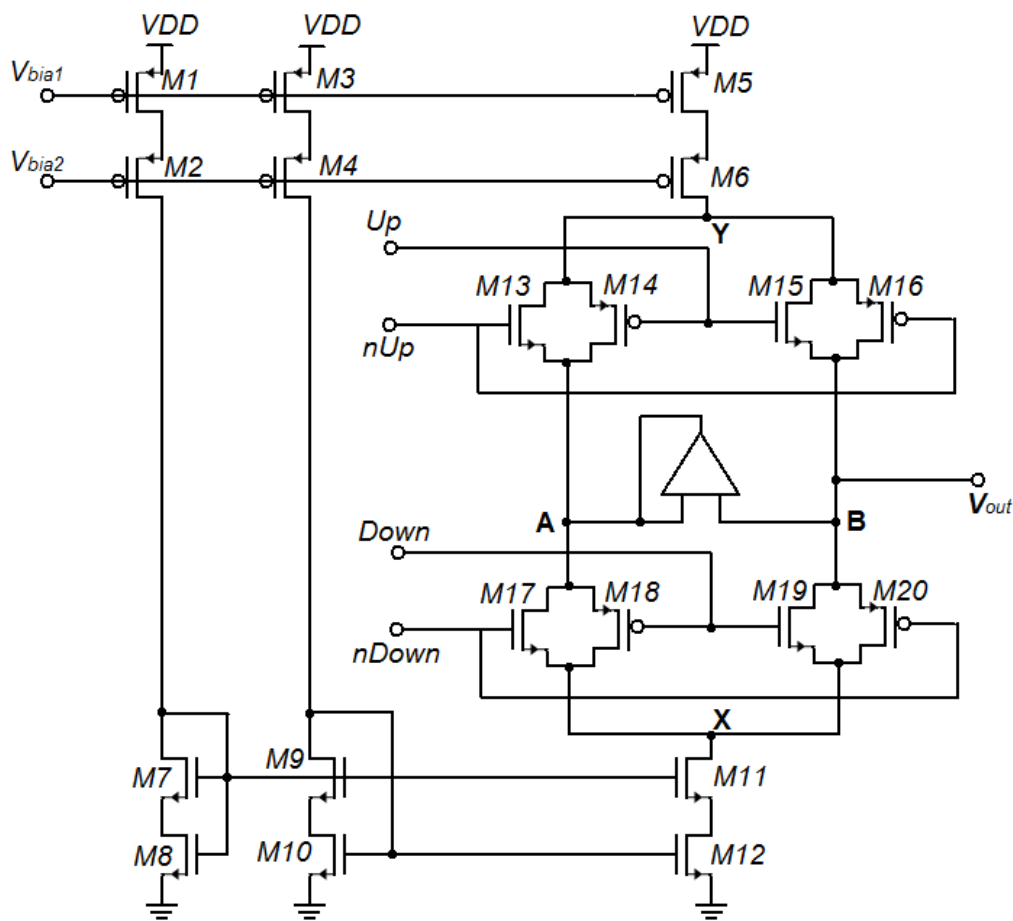
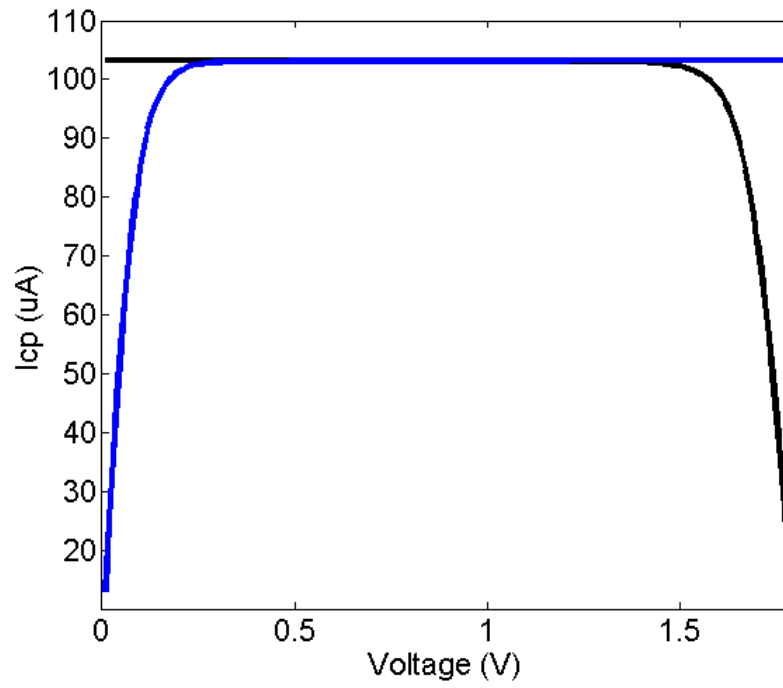
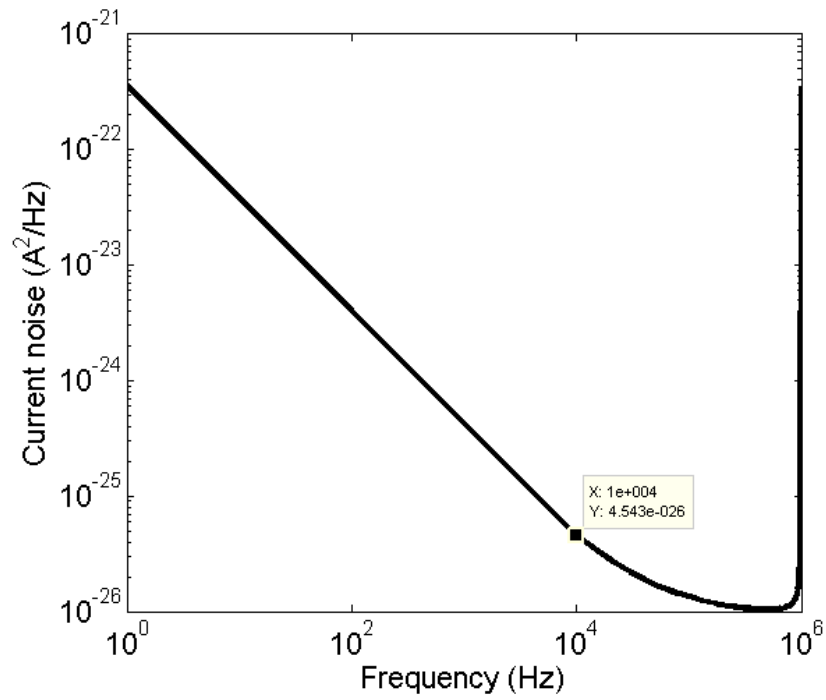


Fig. 5. 7 Schematic of CP



(a)



(b)

Fig. 5. 8 Current mismatch characteristic of CP (a) and current noise of PFD and CP (b)

5.2.2.2. Divider design

The proposed divider employs multi-modulus divider (MMD) architecture [41] which is based on divide-by 2/3 divider connected on series, as shown in Fig.5.9.

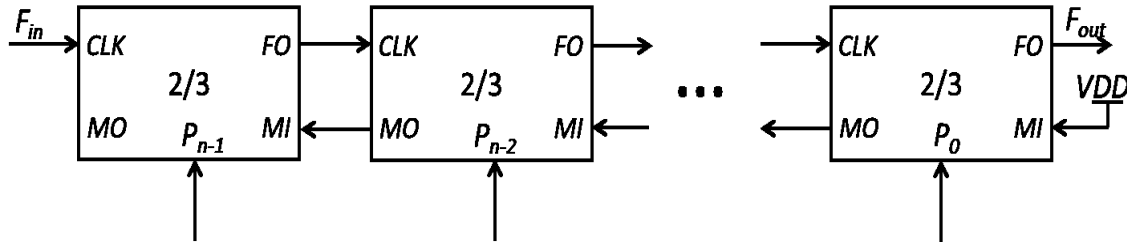


Fig. 5. 9 Divider based on MMD architecture

For this type of divider, a division ratio that increases in unity integer steps from 2^n to $2^{n+1}-1$ is able to be achieved, and the division ratio is given by:

$$N = P_0 + 2^1 P_1 + \dots + 2^{n-2} P_{n-2} + 2^{n-1} P_{n-1} + 2^n \quad (5.19)$$

Thus, in our design, for $N=49$, five divider cell are used and the control word is 10001 (P_4-P_0).

The proposed divide by 2/3 divider cell and the timing diagram is shown in Fig. 5.10. It is known that the divider cell is composed of two E-TSPC flip-flops and one inverter. The first flip-flop (DFF1) embeds a logic gate $A \& (B+C)$ and the second one (DFF2) embeds an AND gate. The proposed divider cell takes three input signals CLK , MI , and P , and produces two output signals MO and FO . When $P=0$ or $MO=0$, the mode select signal B is high resulting in the divide-by-2 mode. For the divider-by-3 mode, the signals $P=1$, $FO=1$, $MI=1$, and $FI=1$ before passing the line Ec . The falling edge of CLK at dash line Ec causes that MO is changed from 0 to 1 that causes B is changed from 1 to 0.

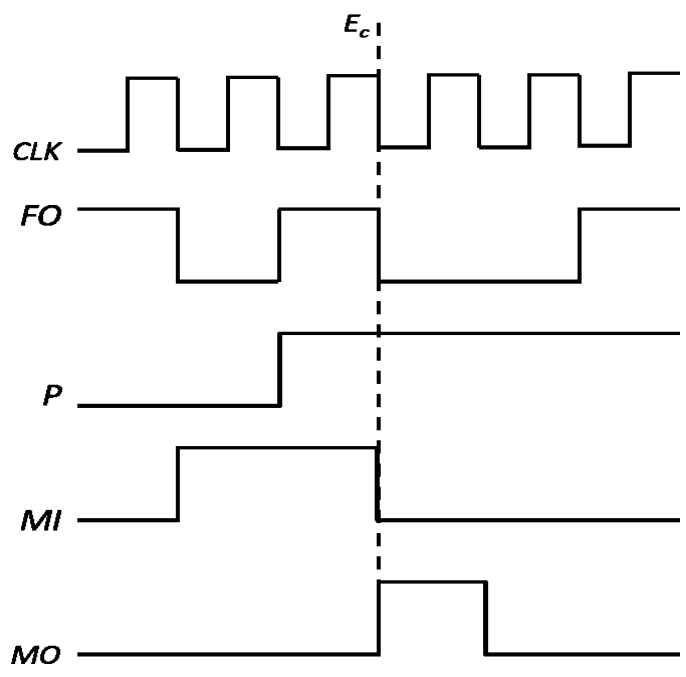
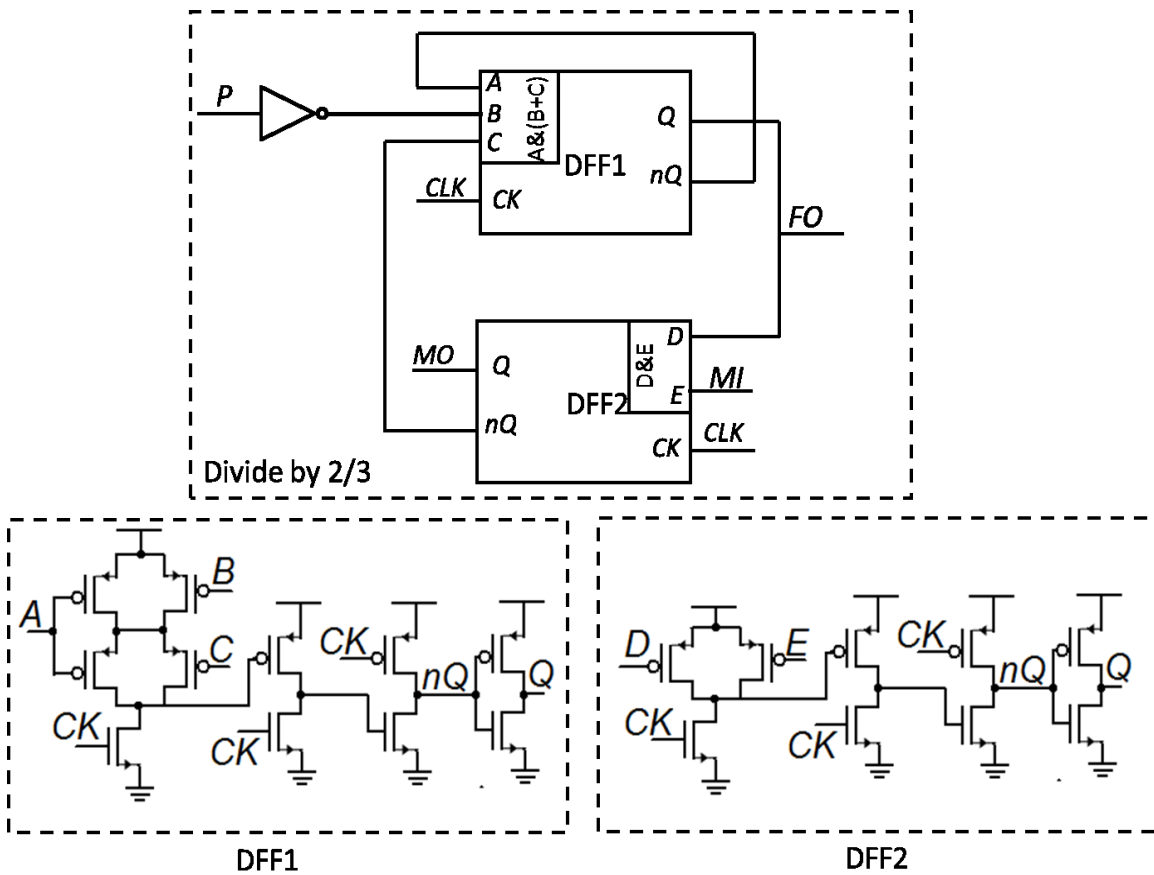
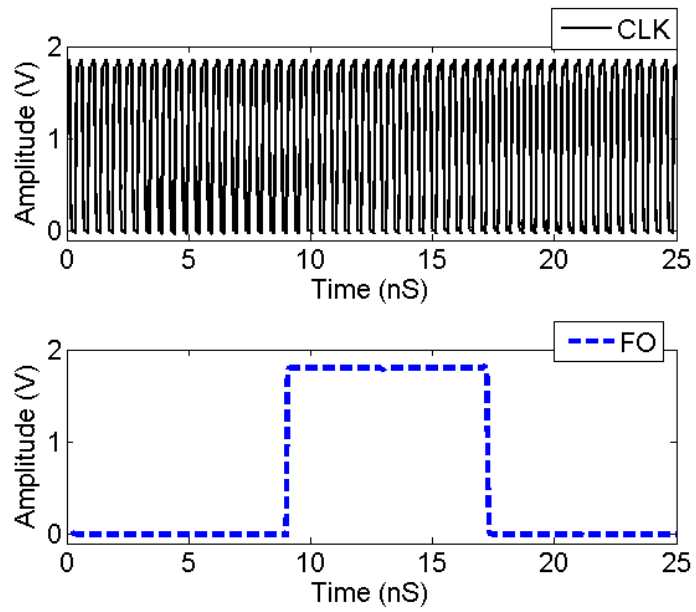


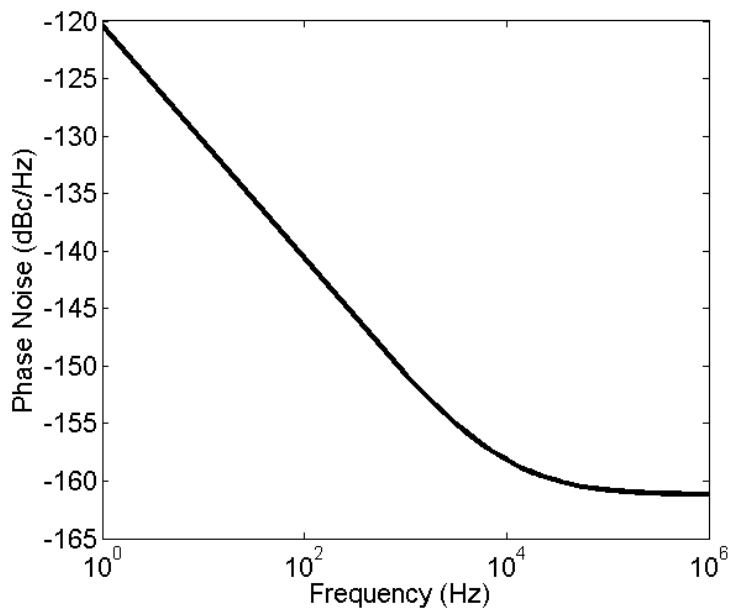
Fig. 5. 10 Proposed 2/3 divider cell and timing diagram

The output waveform (a) and output noise (b) of MMD based divider are shown in

Fig.5.11.



(a)



(b)

Fig. 5. 11 Output waveform (a) and output noise (b) of MMD based divider

5.2.3. Phase Noise Analysis

The linear phase model of PLL with noise generated by each building block is shown in Fig. 5.12[40].

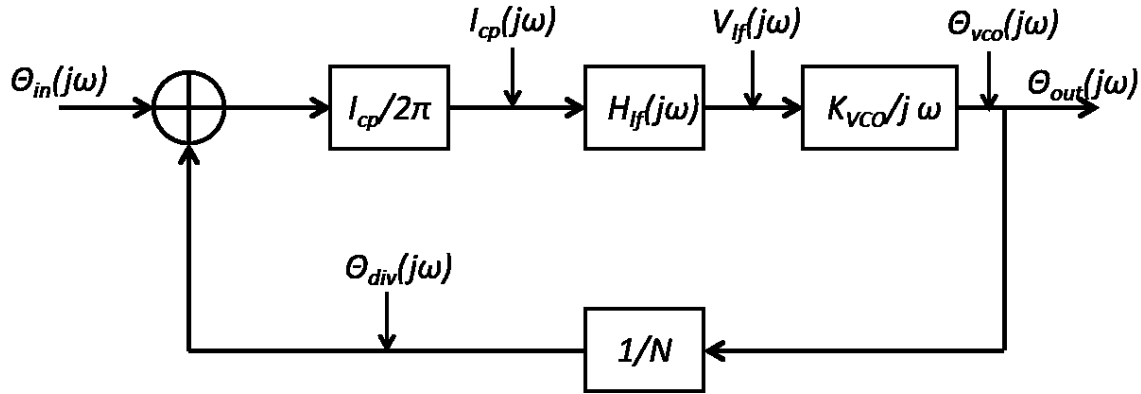


Fig. 5. 12 Linear phase model of PLL with noise of each block

Where, $\Theta_{in}(j\omega)$ is the phase noise from the reference signal; $I_{cp}(j\omega)$ is current noise associated with PFD and charge pump; $V_{lf}(j\omega)$ is voltage noise generated by LPF; $\Theta_{vco}(j\omega)$ is VCO output phase noise; $\Theta_{div}(j\omega)$ is phase noise generated by the divider; $\Theta_{out}(j\omega)$ is total PLL output phase noise.

From the noise model of PLL, the phase noise transfer function of each noise source to the output phase noise is listed in Table 5.3.

Table 5.3 Phase noise transfer function

Noise source	Phase transfer function	
Input noise	$H_{in,n}(j\omega) = \Theta_{out}(j\omega) / \Theta_{in}(j\omega)$	$N \frac{H_{ol}(j\omega)}{1 + H_{ol}(j\omega)}$
PFD/CP noise	$H_{cp,n}(j\omega) = \Theta_{out}(j\omega) / I_{cp}(j\omega)$	$\frac{2\pi N}{I_{cp}} \frac{H_{ol}(j\omega)}{1 + H_{ol}(j\omega)}$

LPF noise	$H_{lf,n}(j\omega) = \Theta_{out}(j\omega) / V_{lf}(j\omega)$	$\frac{K_{vco}}{j\omega} \frac{1}{1 + H_{ol}(j\omega)}$
VCO noise	$H_{vco,n}(j\omega) = \Theta_{out}(j\omega) / \Theta_{vco}(j\omega)$	$\frac{1}{1 + H_{ol}(j\omega)}$
Divider noise	$H_{div,n}(j\omega) = \Theta_{out}(j\omega) / \Theta_{div}(j\omega)$	$-N \frac{H_{ol}(j\omega)}{1 + H_{ol}(j\omega)}$

Since total output noise PSD is the contribution of noise PSD of each block, the total output noise PSD is:

$$S_{out}(\omega) = S_{in,n}(\omega) |H_{in,n}(j\omega)|^2 + S_{cp,n}(\omega) |H_{cp,n}(j\omega)|^2 + S_{lf,n}(\omega) |H_{lf,n}(j\omega)|^2 + S_{vco,n}(\omega) |H_{vco,n}(j\omega)|^2 + S_{div,n}(\omega) |H_{div,n}(j\omega)|^2 \quad (5.20)$$

Where, $S_{in,n}(\omega)$ is the phase noise PSD from the reference signal; $S_{cp,n}(\omega)$ is current noise PSD associated with PFD and charge pump; $S_{lf,n}(\omega)$ is voltage noise PSD generated by LPF; $S_{vco,n}(\omega)$ is VCO output phase noise PSD; $S_{div,n}(\omega)$ is phase noise PSD generated by the divider; $S_{out}(\omega)$ is total PLL output phase noise PSD.

For PFD/CP and LPF we can directly extract the voltage noise PSD by Spectre-RF; for VCO and divider, first we can extract the phase noise $L(\omega_m)$ by Spectre-RF, and convert to phase noise PSD $S_{\theta}(\omega_m)$ by [39]:

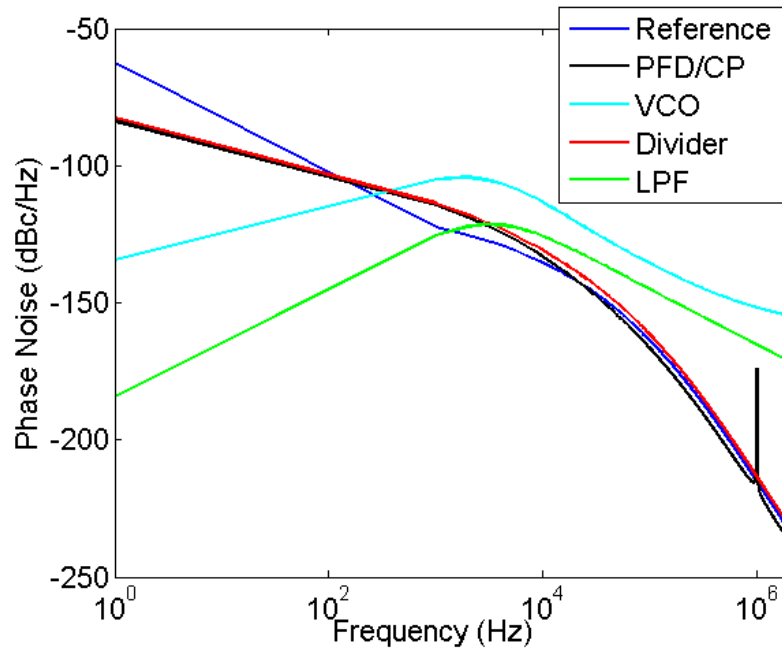
$$L(\omega_m) = 10 \log \left[\frac{S_{\theta}(\omega_m)}{2} \right] \quad (5.21)$$

For reference signal, the phase noise PSD can be found by [40]:

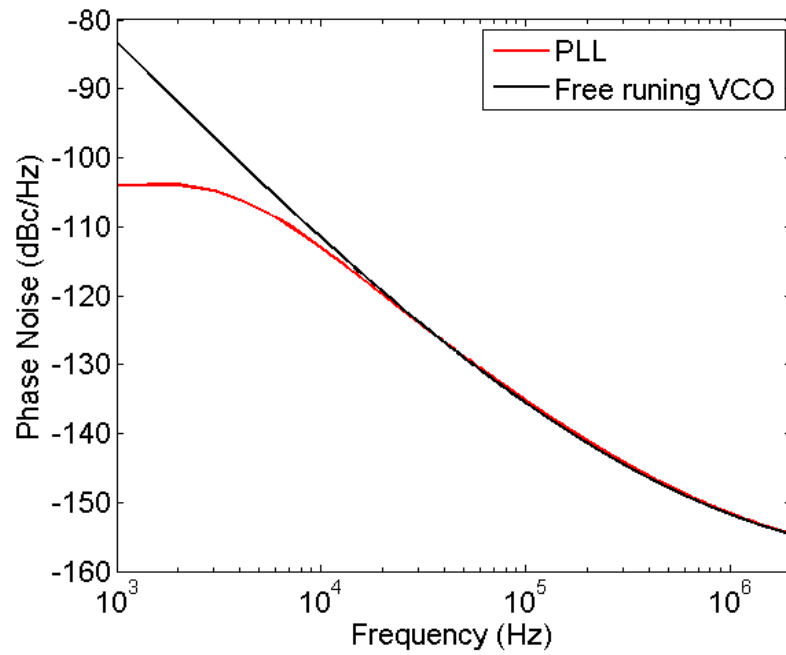
$$S_{in,n}(\Delta\omega) = 10^{-16\pm 1} \cdot \left[1 + \left(\frac{\omega_0}{2\Delta\omega Q_L} \right)^2 \right] \left(1 + \frac{\omega_c}{\Delta\omega} \right) \quad (5.22)$$

where ω_0 is the reference frequency; ω_c is the corner frequency, which is normally in the range 1-10 KHz; Q_L is the Q-factor of the resonator, which is in the order of 10^4 to 10^6 ; $\Delta\omega$ is offset frequency.

After obtaining total output noise PSD by (5.20), the total phase noise can be converted by (5.21). The output phase noise of each block (a) and the total phase noise of PLL (b) are shown in Fig. 5.13. The layout of proposed PLL is shown in Fig.5.14. In Fig. 5.13(b), it is demonstrated that the phase noise of the PLL is much better than the free running FBAR-VCO below 10 KHz offset frequency.



(a)



(b)

Fig. 5. 13 Output phase noise of each block (a) and the total phase noise of PLL (b)

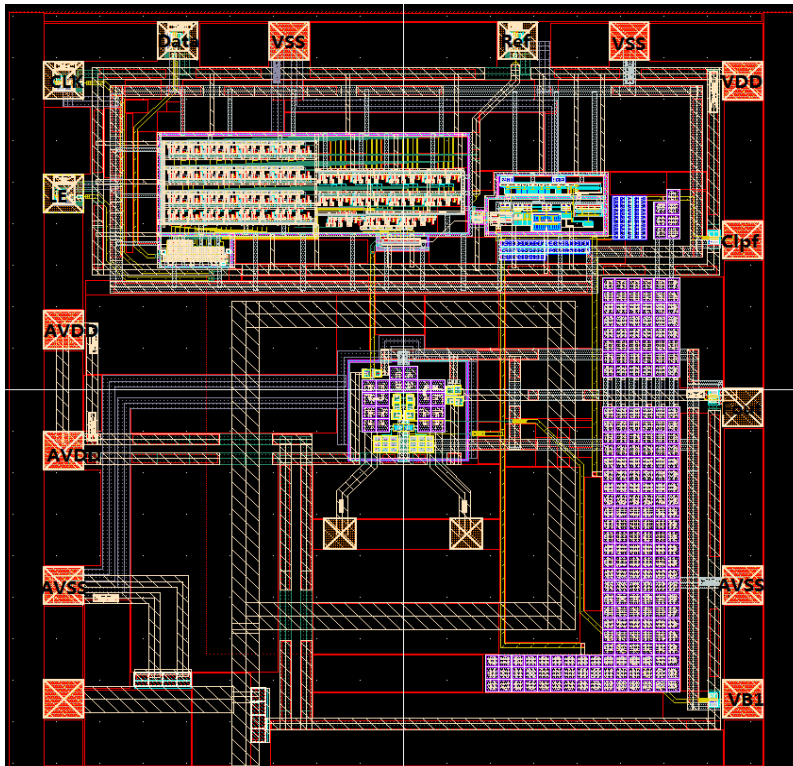


Fig. 5. 14 Layout of proposed PLL

5.3. Conclusion

In this Chapter, we replaced the LC-VCO of the traditional PLL by the presented cross-coupled FBAR-VCO, to design an FBAR-VCO based PLL. The LPF design method and stability analysis is presented and the circuit design of phase PFD, charge pump, and MMD divider is introduced. Especially for the design of charge pump, the architecture based on complementary logic switches is adopted to reduce the mismatch current and the current noise. Finally, the phase noise of PLL is analyzed and simulated. The simulation phase noise proves the possibility of FBAR-VCO based PLL and shows that the FBAR-VCO based PLL further improved the phase noise of FBAR-VCO.

Chapter VI

Conclusion and Future Work

6.1. Conclusion

This thesis mainly focuses on the design of monolithic low phase noise FBAR oscillator. In the beginning of this thesis, the demand of low cost, high performance and high integration of RFIC and the poor phase noise and high power consumption of the normal Ring-oscillators and LC-oscillators are emphasized. In order to solve these problem of current oscillators, researcher are trying using high Q-factor FBAR resonators to design low phase noise oscillators. Then the structure and equivalent circuit model of FBAR and the oscillator theory including Barkhausen criteria, negative resistance and phase noise model which can be used in FBAR oscillators are presented to provide the theoretical foundation of FBAR oscillator design. In the realization of FBAR oscillators, at first the Pierce FBAR-DCO and the inverter based FBAR-DCO are designed because of the simplicity structure. The oscillation condition of these two FBAR-DCOs is analyzed and the simulation result demonstrates that the FBAR-DCO is able to obtain a phase noise which is 20 dB lower than the phase noise of normal LC-oscillators. Then the second kind of FBAR oscillator in this thesis employs cross-couple architecture. Two methods to mitigate low frequency instability are proposed, which the first method employs a capacitor and while the other one employs a series inductor-capacitor. By considering the effect of transistors' size on the Q-factor and impedance of FBAR, excellent phase noise and high loop gain are obtained. Furthermore, based on the designed cross-coupled FBAR-VCO core, a multiband FBAR-VCO operating at 0.65 GHz, 0.98 GHz, 1.96 GHz and 3.92 GHz is presented. Although the traditional divider and multiplier are employed, the possibility

of a multiband VCO using FBAR-VCO as a core circuit has been demonstrated. Finally, we replaced the LC-VCO of the traditional PLL by the presented cross-coupled FBAR-VCO, to design an FBAR-VCO based PLL. For the design of charge pump, the architecture based on complementary logic switches is adopted to reduce the mismatch current and the current noise. The proposed PLL proves the possibility of FBAR-VCO based PLL and the simulation result shows the phase noise of FBAR-VCO is further improved.

6.2. Future work

This section will provide future research opportunities for the designed prototypes in this work.

1. In the design of the pierce FBAR-DCO and the inverter based FBAR-DCO, the final fabrication was failed because of the R_m is too large to oscillate. It is significant to find the approach to reduce R_m , or design an FBAR oscillator which can still oscillate even if the R_m is large.

2. FBAR oscillators have two main applications. The first one is used as frequency reference to replace the quartz crystal oscillators while the second one is used as local oscillator to replace the normal Ring-VCOs and LC-VCOs. For the first application, the demand of low phase noise is satisfied by our novel phase noise optimization method. While For the second application, both low phase noise and wide tuning range are needed. Thus, the tuning range of the proposed FBAR oscillator is necessary to be improved. Now the method of improving tuning range based on parallel inductor-FBAR has been under investigation and will reported in near future.

Reference

- [1] S. Lee, B. Kim, J. Y. Kim, ed., "An IEEE 802.15.4g SUN OFDM-based RF CMOS transceiver for Smart Grid and CEs," IEEE ICCE, pp. 520-521, Jan. 2013.
- [2] K. Zhou, J. Zhou, Z. Xu, "Design of a high performance RF transceiver for TDD-LTE system," IEEE MTT-S, pp. 1-3, June 2012.
- [3] A. Shirane, M. Otsuru, S. Lee, ed., "A process-scalable RF transceiver for short range communication in 90 nm Si CMOS," IEEE RFIC, pp. 455-458, June 2012.
- [4] J. Huang, Y. Hsu, Y. Lo, ed., "Design and fabrication of low-insertion loss and high-isolation CMOS-MEMS switch for microwave applications," IMPACT, pp. 1-3, Oct. 2010.
- [5] M. A. Llamas, D. Girbau, M. Ribo, ed., "RF-MEMS Uniplanar 180 Phase Switch Based on a Multimodal Air-Bridged CPW Cross," *IEEE Trans. Microw. Theory Techn.*, vol. 59, NO. 7, pp. 1769- 1777, July 2011.
- [6] R. Stefanini, M. Chatras, P. Blondy, ed., "Miniature RF MEMS metal-contact switches for DC-20 GHz applications," Microwave Symposium Digest, pp. 1-4, June 2011.
- [7] N. Zahirovic, R. R. Mansour, M. Yu, "A MEMS variable capacitor with piezoresistive position sensing fabricated in a standard 0.35um CMOS process," Microwave Symposium Digest, pp. 1, May 2010.
- [8] C. Han, D. Choi, S. Choi, ed., "MEMS variable capacitor with superior linearity and large tuning ratio by moving the plate to the increasing-gap direction," Micro Electro Mechanical Systems, pp. 772- 775, Jan. 2011.

- [9] M. A. Elshurafa, P. H. Ho, K. N. Salama, "Low voltage RF MEMS variable capacitor with linear C-V response," *Electronics Letters*, vol. 48, NO. 7, pp. 392- 393, March 2012.
- [10] Y. Shim, J. Ruan, Z. Wu, ed., "An integrated RF MEMS tunable filter," *Micro Electro Mechanical Systems*, pp. 15- 18, Jan. 2012.
- [11] H. Hsu, A. D. Margomenos, D. Peroulis, "A monolithic RF-MEMS filter with continuously-tunable center-frequency and bandwidth," *IEEE SiRF*, pp. 169- 172, Jan. 2011.
- [12] Y. Liu, X. Li, D. Fang, ed., "RF MEMS filter based on one step of copper electroplating," *IEEE NEMS*, pp. 945- 949, Jan. 2010.
- [13] M. Rinaldi, Y. Hui, C. Zuniga, ed., "High frequency AlN MEMS resonators with integrated nano hot plate for temperature controlled operation," *IEEE FCS*, pp. 1- 5, May 2010.
- [14] S. Qin, A. Qiu, S. Yan, ed., "Nonlinear oscillation characteristics of MEMS resonator," *ICMA*, pp. 1250- 1253, Aug. 2010.
- [15] J. Small, M. S. Arif, A. Fruehling, ed., "A Tunable Miniaturized RF MEMS Resonator With Simultaneous High Q (500–735) and Fast Response Speed," *Microelectromechanical Systems*, vol. 22, NO. 2, pp. 395- 405, April 2013.
- [16] H. Fujita, H. Toshiyoshi, T. Ishida, "From MEMS-CMOS towards heterogeneous integration over scale," *ECS Transactions*, vol. 45, NO. 6, pp. 93–99, 2012.
- [17] N. Zahirovic, R. R. Mansour, and M. Yu, "Piezoresistive position sensing for the detection of hysteresis and dielectric charging in CMOS-MEMS variable capacitors," *IEEE Trans. Microwave Theory Tech.*, vol. 58, NO. 12, pp. 3961–3970, Dec. 2010.

- [18] N. Sarkar, K. Trainor, and R. R. Mansour, "Temperature compensation in integrated CMOS-MEMS scanning probe microscopes," *IET Micro Nano Lett.*, vol. 7, NO. 4, pp. 297–300, Apr. 2012.
- [19] A. Italia, C. M. Ippolito, and G. Palmisano, "A 1-mW 1.13–1.9 GHz CMOS LC VCO Using Shunt-Connected Switched-Coupled Inductors," *IEEE Trans. Circuits Syst. I, Reg. Paper*, vol. 59, NO. 6, pp. 1145–1155, June 2012.
- [20] D. Ponton, G. Knoblinger, A. Roithmeier, ed., "LC-VCO in the 3.3- to 4-GHz Band Implemented in 32-nm Low-Power CMOS Technology," *IEEE Trans. Circuits Syst. II, Exp. Briefs*, vol. 58, NO. 8, pp. 467–471, Aug. 2011.
- [21] A. Sai, T. Ymaji, T. Itakura, "A 570fsrms integrated-jitter ring-VCO-based 1.21GHz PLL with hybrid loop," ISSCC, pp. 98- 100, Feb. 2011.
- [22] Y. Park, W. Choi, "Supply noise insensitive ring VCO with on-chip adaptive bias-current and voltage-swing control," ISCAS, pp. 229- 232, May 2011.
- [23] G. B. Razavi, "Monolithic Phase-Locked Loops and Clock Recovery Circuits: Theory and Design," Piscataway, NJ: IEEE Press, 1996.
- [24] K. Ostman, S. Sipila, I. Uzunov, ed., "Novel VCO architecture using series Above-IC FBAR and parallel LC resonance," *IEEE J. Solid-State Circuits*, vol. 41, NO. 10, pp. 2248- 2256, Oct. 2006.
- [25] J.Hu, W. Pang, R. Ruby, ed., "A 750 μm 1.575 GHz Temperature-Stable FBAR-Based PLL," IEEE RFIC, pp.317- 320, June 2009.
- [26] J.Hu, R. Parkery, R. Ruby, ed., "A wide-tuning digitally controlled FBAR-based oscillator for frequency synthesis," IEEE FCS, pp. 608- 612, June 2010.

- [27] Y. W. Lin, ed., "Series-Resonant VHF Micromechanical Resonator Reference Oscillators," *IEEE J. Solid State Circuits*, vol. 39, pp. 2477-2491, 2004.
- [28] K. W. Kim, ed., "Resonator Size Effects on the FBAR Ladder Filter Performance," *IEEE Microw. Wirel. Compon. Lett.*, vol. 13, pp. 335-337, 2003.
- [29] J. D. Larson, P. D. Bradley, S. Wartenberg, ed., "Modified Butterworth-Van Dyke circuit for FBAR resonators and automated measurement system," Proc. IEEE Ultrasonics Symposium, vol. 1, pp. 863-868, Oct. 2000.
- [30] N. M. Nguyen, R. G. Meyer, "Start-up and Frequency Stability in High-Frequency Oscillators," *IEEE J. Solid State Circuits*, vol. 27, pp. 810-820, 1992.
- [31] B. Razavi, *Design of Analog CMOS Integrated Circuits*, U.S.: McGraw-Hill Companies, 2002.
- [32] T. H. Lee, *The Design of CMOS Radio-Frequency Integrated Circuits*, Cambridge, U.K.: Cambridge Univ. Press, 2004.
- [33] H. Bahadur, R. Parshad, "Modified Pierce oscillator circuit," Proceedings of the IEEE, 1978.
- [34] A. Kochhar, T. Matsumura, G. Zhang, ed., "Monolithic Fabrication of Film Bulk Acoustic Resonators above Integrated Circuit by Adhesive-Bonding-Based Film Transfer," IEEE IUS, 2012.
- [35] J. Y. Lee, S. H. Lee, H. Kim, ed., "A 23-GHz capacitive-degeneration LC VCO with a FOM of -199 dBc/Hz," *Microw. Opt. Techn. Lett.*, vol. 50, NO. 6, pp. 1688- 1690, June 2008.

- [36] S. Kim, H. Shin, "An E-TSPC Divide-by-2 circuit with forward body biasing in 0.25 μ m CMOS," *IEEE Microwave and Wireless Components Letters*, vol. 19, NO. 10, October 2009.
- [37] S. Rai, Y. Su, W. Pang, ed., "A digitally compensated 1.5 GHz CMOS/FBAR frequency reference," *IEEE Trans. Ultrason., Ferroelectr., Freq. Control*, vol. 57, no.3, pp. 552-561, 2010.
- [38] M. L. Johnston, I. Kymissis and K. L. Shepard, "FBAR-CMOS oscillator array for mass-sensing applications," *IEEE Sensor J.*, vol. 10, no.6, pp. 1042-1047, 2010.
- [39] J. Lin and Y. Kao, "Wireless temperature sensing using a passive RFID tag with film bulk acoustic resonator," *IEEE IUS*, pp. 2209-2212, Nov. 2008.
- [40] K. Kundert, "Predicting the Phase Noise and Jitter of PLL-Based Frequency Synthesizers," 2006.
- [41] John Rogers, Calvin Plett, Foster Dai, *Integrated Circuit Design for High-Speed Frequency Synthesis*, U.S.: Artech House Microwave Library, 2006.